

# THÈSE DE DOCTORAT

de l'Université de recherche Paris Sciences et Lettres  
PSL Research University

Préparée à l'École Nationale Supérieure de Chimie de Paris

Conception de contacts oxydes et de pérovskites à cations mixtes  
pour des cellules solaires hautement efficaces

Design of oxide contacts and mixed cation hybrid perovskites for  
highly efficient solar cells

Ecole doctorale n° ED 388

Ecole doctorale de Chimie Physique et de Chimie Analytique de Paris Centre

Spécialité Chimie Physique

## COMPOSITION DU JURY :

Présidente du jury  
Pr. Christel LABERTY-ROBERT  
Professeur Sorbonne Université,

Pr. Fabrice GOUBARD  
Professeur Université de Cergy-Pontoise,  
Rapporteur

Pr. Nicolas MERCIER  
Professeur Université d'Angers,  
Rapporteur

Dr. Samir FARHAT  
Maître de Conférences Université Paris 13,  
Examinateur

Dr. Thierry PAUपोर्टÉ  
Directeur de Recherche CNRS,  
Directeur de thèse

Soutenue par Pengjiu WANG  
le 25 Septembre 2018

Dirigée par Thierry PAUपोर्टÉ



# ACKNOWLEDGEMENTS

It would not have been possible to write this doctoral thesis without the help and support of the kind people around me. Though many individuals aided me, I would like to highlight and thank in particular the following people.

I would like to acknowledge the China Scholarship Council for financing supporting to me.

I would like to express my deepest appreciation to my thesis director, Dr. Thierry Pauport é I would like to thank him for his guidance and advice during these past three years of research, investigation and his help in writing publications. I am grateful for his patience and endless support while correcting my thesis manuscript.

I would like to thank Pr. Fabrice Goubard and Pr. Nicolas Mercier for accepting to be my reviewers, as well as Pr. Christel Labery-Robert and Pr. Samir Farhat for being my examiners.

I am deeply grateful to all my colleagues and friends for their help, their support, for all the great times we shared, and the many scientific discussions. I would like to thank in particular Post-doctor Zhipeng Shao, Shuping liu, Zhonghan Zhang, and Fan Sun, as well as Dr. Hengjun Chen, Zhengyu Yang, Tao Zhu, Maria Ulfa, Alexandra Szemjonov, Sana Koussi, and many others.

Lastly I would like to thank my family for all their love and encouragement. My parents, who raised me with love and always supported me. Besides, I want especially to thank my queen YanYAN, you are my Polaris, tell me where to go.

Thank all of you

## Résumé

Hormis l'énergie nucléaire et géothermique, le soleil est à l'origine de la quasi-totalité des sources d'énergie renouvelables et fossiles utilisées par l'humanité pour ses besoins alimentaires, domestiques et industriels. Cette énergie provient de la réaction de fusion des noyaux d'hydrogène en une réaction en chaîne continue produisant des noyaux d'hélium. Ceci entraîne une légère perte de masse qui se convertit en énergie - moitié sous forme de lumière, moitié sous forme de particules appelées neutrinos. Cette énergie inépuisable est la plus abondante et prometteuse pour la transition énergétique.

Le photovoltaïque (PV) (la conversion de l'énergie solaire en électricité) a connu des progrès continus depuis les années 50 avec le développement des cellules au silicium cristallin, des cellules en couches minces, et, plus récemment, des cellules solaires à colorant et organiques. La dernière famille de cellules solaires PV apparue est basée sur des composés semiconducteurs halogénés de structure pérovskite. Ces composés ont un caractère hybride organique-inorganique et ont pour formule générale  $ABX_3$ , X étant un halogénure et B l'ion plomb. Ce sont des semiconducteurs fortement absorbant dans le domaine du proche UV-visible. Ils possèdent une bande interdite de transition directe qui peut être modulée dans une large gamme en ajustant la composition de la pérovskite. Ces cellules utilisent aussi des contacts solides de part et d'autre de la pérovskite, un contact capte les trous photogénérés et un oxyde semiconducteur de type n (typiquement  $TiO_2$ ) capte les électrons. Le rendement de photoconversion des cellules solaires à pérovskites (PSC) a connu une augmentation hors-norme depuis leur apparition il y a quelques années, passant de 3,8% à 22,7%.

Dans cette thèse, nous nous sommes appliqués à optimiser la couche bloquante des trous (BL) de  $TiO_2$  et à développer des pérovskites à cations monovalents multiples (A dans  $ABX_3$ ) pour l'application. Nous avons finalement obtenu des PSC très stables, reproductibles et de très haut rendement de photoconversion.

Le Chapitre 1 est une revue bibliographique de différentes technologies de cellules solaires, des composants des cellules de type PSC ainsi que des principales

techniques de caractérisation des cellules photovoltaïques.

Dans le Chapitre 2, nous avons étudié les paramètres qui rendent les couches bloquantes de TiO<sub>2</sub> efficaces. Plusieurs BLs ont été préparés par la technique de pyrolyse-spray et par spin-coating. Nous avons trouvé que les premières étaient minces, très compactes et parfaitement couvrantes. Par spectroscopie Raman, nous avons montré qu'elles étaient constituées d'anatase pure et la voltamétrie cyclique a montré qu'elles étaient parfaitement bloquantes. Les couches préparés par spin-coating étaient poreuses, contenaient des craquelures et des trous et n'étaient pas complètement bloquantes. De plus elles étaient moins cristallisées que celles préparés par pyrolyse spray et contenaient de la phase rutile. Nous avons aussi utilisé la spectroscopie d'impédance pour étudier les différents phénomènes de transfert et d'accumulation de charges se déroulant dans le dispositif sous éclairage et comment ils sont influencés par la BL.

Dans le chapitre 3, nous avons étudié le phénomène de cristallisation spontanée de la pérovskite FAMA (FA<sub>0.87</sub>MA<sub>0.13</sub>Pb(I<sub>0.87</sub>Br<sub>0.17</sub>)<sub>3</sub> avec FA le cation formamidinium et MA le cation méthylammonium) par le contrôle de la concentration de supersaturation de la solution de précurseur. Nous avons développé deux types de dépôts de la pérovskite, le dépôt direct et la technique de dépôt à chaud (hot-casting). La technique de dépôt direct sans étape d'induction de la cristallisation par égouttement par un anti-solvant a permis d'obtenir une phase  $\alpha$  pure. Elle pourrait permettre l'obtention des films homogènes sur une large surface. La technique de hot-casting a permis d'obtenir des couches denses, formées de gros grains et de phase  $\alpha$  pure. Ces couches présentaient beaucoup moins de joints de grains ce qui devrait permettre de limiter fortement leur effet néfaste de recombinaison de charges. Cependant, ces couches présentaient des crêtes qui sont à l'origine de défauts et de propriétés photovoltaïques décevantes. Nous avons enfin étudié la préparation de la pérovskite FAMA par la technique d'égouttement (dripping) d'un antisolvant pour induire la cristallisation et finalement obtenir des dispositifs PV très performants et reproductibles. L'étude de 30 cellules a donné les paramètres PV moyens suivants :  $V_{oc} = 1104$  mV,  $J_{sc} = 23.16$  mA/cm<sup>2</sup>, et FF = 78%, soit un rendement de photoconversion

moyen (PCE) de 19.8%.

De plus, nous avons mené une étude détaillée de l'extraction de charge par les couches adjacentes en utilisant les techniques de mesure de déclin de photoluminescence (PL) (technique TCSPC) et de spectres de PL stationnaires. Nous avons montré que le temps de vie des porteurs de charges et donc le temps d'extraction dépend de la pérovskite et de la couche d'oxyde. La structure planaire TiO<sub>2</sub>-compact conduit à un transfert d'électrons peu rapide et est donc peu efficace. D'un autre côté, la structure TiO<sub>2</sub>-compact/mesoporeuse/PCBM est beaucoup plus efficace et permet de générer un photocourant beaucoup plus élevé. Il existe donc une marge d'amélioration pour les dispositifs du côté de cette couche qui collecte et transporte les électrons.

Dans le chapitre 4, nous avons étudié l'ajout de 5% de cation césium (Cs<sup>+</sup>) dans la structure pérovskite FAMA. Nous avons étudié les premières étapes de la nucléation et montré que l'ajout de Cs favorise la nucléation hétérogène. Ce changement de composition diminue l'énergie de cristallisation. La présence de Cs améliore la pureté de la pérovskite et favorise l'obtention de la phase  $\alpha$ . Nous avons montré que cette grande pureté améliore la stabilité de la pérovskite dans le temps et en température. Nous avons proposé un mécanisme différent de photoluminescence de la pérovskite en présence de Cs. De plus, nous avons aussi testé cette pérovskite à triple cation monovalent avec la couche d'extraction électronique TiO<sub>2</sub>-compact/mesoporeuse/PCBM. Avec cette configuration, les cellules ont atteint un  $J_{sc}$  très élevé de 24.61 mA/cm<sup>2</sup>

Finalement, nous avons obtenu des dispositifs de rendement très élevés, reproductible et stable avec la pérovskite Cs5FAMA. Pour les cellules record, nous avons mesuré:  $V_{oc} = 1104$  mV,  $J_{sc} = 24.19$  mA/cm<sup>2</sup>, et  $FF = 77.4\%$ , soit un PCE de 20.67 %. Le suivi sur 5 minutes de la puissance maximale délivrée a donné un rendement stable de 20.6%. Les paramètres photovoltaïques moyens mesurés pour 40 cellules étaient de  $V_{oc} = 1106$  mV,  $J_{sc} = 23.84$  mA/cm<sup>2</sup>,  $FF = 76\%$ , donnant un PCE de 20.2 %.

## **Abstract**

In sun, hydrogen and helium be lighted to generate atomic nuclei combine and release heavier energy by fusion reaction. Human beings never give up grabbing renewable energy from sun. Photovoltaic devices always deem the best candidate for a renewable energy.

Since the 50's, photovoltaics is a field in continuous development, from the earlier developed crystalline silicon to thin film solar cells, and then to the more recent dye-sensitized solar cells (DSSCs) and organic solar cells. Recently, a new family of very promising solar cells, derived from DSSCs, appeared based on new absorber materials, the hybrid perovskites (HPs). In perovskite solar cells (PSCs), organic and inorganic hybrid perovskites with a general formula  $ABX_3$  replaces the pigment in DSSCs, and exhibits an extremely high optical absorption coefficient and a tunable band gap via composition change. Meanwhile, to improve the device stability, traditional liquid electrolyte is replaced by a solid state hole transporting materials (HTM). Based on these advanced improvements, the power conversion efficiency (PCE) of PSC has rapid increased from 3.8% to certified 22.7% within a few years.

In this thesis, we have optimized the  $TiO_2$  hole blocking layer (BL) and we have investigated multiple monovalent cation (A in  $ABX_3$ ) perovskite compounds for PSC application. Finally we realized a series of stable, reproducible and highly efficient PSCs.

Chapter 1 is a bibliographic review of solar cells and PSC components as well as a description of the main techniques employed for the device characterizations. In the chapter 2, we have investigated the key parameters that render the  $TiO_2$  BL efficient in PSCs. Several BLs have been prepared using the aerosol spray pyrolysis and the spin-coating techniques. We found that the sprayed BLs present thin, highly compact, full-covering characters. They exhibited the pure anatase phase characters by Raman spectroscopy, and realized perfectly blocking effect via cyclic voltammetry. On the other hand, the spin-coated layers were porous, contained cracks and pinholes and were not fully blocking. They were less crystallized than the sprayed layers. Besides,

we developed the use of the impedance spectroscopy technique to investigate the various processes taking place in the cells under illumination and how they are influenced by the BL.

In the chapter 3, we have investigated the promotion of spontaneous crystallization and growth of FAMA ( $\text{FA}_{0.87}\text{MA}_{0.13}\text{Pb}(\text{I}_{0.87}\text{Br}_{0.17})_3$  with FA the formamidinium cation and MA the methylammonium one) perovskite by the control the supersaturation concentration of the precursor solution. We developed two kinds of perovskite deposited techniques, the simply direct film-forming and the hot-casting method. The direct film-forming without dripping process realized high purity perovskite  $\alpha$ -phase and could be used for deposition at the large scale. The hot-casting technology realized a dense, big-grain, and pure phase perovskite layer, in order to further decrease grain boundaries and eliminate its detrimental effect on the charge carriers recombinations. Due to the morphological ridge structures of the hot-casted perovskite, these layers did not demonstrate excellent photovoltaic properties. Then we adopted an anti-solvent dripping step to trigger crystallization and finally realized high efficiency and highly reproducible perovskite photovoltaic devices. The investigation of 30 FAMA photovoltaic devices exhibited the following average photovoltaic parameters;  $V_{oc} = 1104$  mV,  $J_{sc} = 23.16$  mA/cm<sup>2</sup>, and FF = 78%, from which it resulted an average power conversion efficiency (PCE) of 19.8%.

In addition, we have carried out a detailed investigation of the charge extraction for the various layers by time-resolved photoluminescence (TCSPC technique) and steady-state photoluminescence (PL) spectroscopy. We obtained reasonable conclusions about the effect of the perovskite composition on the charge carrier injection kinetics and separation. We explained that the planar structure of TiO<sub>2</sub>-compact ETL usually not attain excellent photovoltaic properties due to slow charges injection. We found that the TiO<sub>2</sub>-compact/mesoporous/PCBM ETL achieved much more efficient electron injection. Then we concluded that the finding of a new electron transport material that could improve electron injection could breakthrough a new solar cells record.

In the chapter 4, we have thoroughly investigated the effect of adding 5% of cesium

cation ( $\text{Cs}^+$ ) into the dual cation FAMA perovskite. Our analysis of the early stage nucleation kinetics before heating treatment has shown that the addition of Cs promotes the heterogeneous nucleation compared to FAMA. It indicated that the crystallization Gibbs free energy of the system was decreased. The XRD patterns comparison between Cs5FAMA and FAMA perovskite showed that the Cs cation introduction into the perovskite matrix reduces the possibility of phase segregation and promotes the purity of the photoactive black  $\alpha$ -phase. The higher phase purity further prevents perovskite phase decomposition under the high temperature operational conditions. It is a key element to make sure that solar cells can operate in a stable manner. Based on energy band theory, we propose a photoluminescence mechanism for Cs5FAMA and predict that Cs5FAMA belongs to direct semiconductors. In addition, we designed a new electron extraction layer of  $\text{TiO}_2$ -compact/mesoporous/PCBM, this configuration cells achieved a very high  $J_{sc}$  of  $24.61 \text{ mA/cm}^2$ .

Finally, we achieved high efficiency, reproducible, and stable devices with Cs5FAMA perovskite. These photovoltaic devices exhibited at best an open circuit voltage  $V_{oc} = 1104 \text{ mV}$ , a short circuit current  $J_{sc} = 24.19 \text{ mA/cm}^2$ , and a fill factor  $\text{FF} = 77.4\%$ , resulting in a PCE of  $20.67\%$ . The maximum power point tracking for 5 minutes of the cells produced a steady-state PCE of  $20.6\%$ . The average photovoltaic parameters were  $V_{oc} = 1106 \text{ mV}$ ,  $J_{sc} = 23.84 \text{ mA/cm}^2$ ,  $\text{FF} = 76\%$ , and PCE of  $20.2\%$  for 40 piece of independent devices.

# Contents

General introduction .....	1
Chapter 1 Context .....	3
1.1 Introduction.....	3
1.1.1 Solar energy .....	3
1.1.2 Standard solar spectral irradiance .....	4
1.2 Several kinds of photovoltaic solar cells .....	5
1.2.1 Silicon solar cells .....	6
1.2.2 Dye-sensitized solar cells.....	9
1.3 Perovskite solar cells.....	11
1.3.1 Developing of Perovskite solar cells.....	11
1.3.2 The perovskite component .....	13
1.3.3 Structure of perovskite solar cells.....	15
1.3.3.1 The electron transport layer .....	16
1.3.3.2 The perovskite layer.....	16
1.3.3.3 The hole transporting layer .....	18
1.3.3.4 The back contract electrode .....	20
1.4 Characterization and analysis of Perovskite solar cells .....	20
1.4.1 Solar cell's characterization .....	20
1.4.2 Materials characterization in PSC.....	22
References.....	23
Chapter 2. TiO <sub>2</sub> electron transport layer (ETL) Optimization and achievement of high efficiency MAPI perovskite solar cells by two-step deposition method. ....	32
2.1 Introduction.....	32
2.2 Experiments .....	33
2.3 Results and discussion .....	34
2.4 Conclusion .....	52
References.....	55
Chapter 3. Formamidinium and methylammonium dual organic cations hybrid	

perovskite solar cells.....	61
3.1 Introduction.....	61
3.2 Experiments .....	62
3.3 Results and discussion .....	66
3.3.1 Preparation of high purity FAMA perovskite by direct film-forming method.....	66
3.3.2 Big-sized grains of FAMA perovskite prepared by hot-casting method.....	72
3.3.3 High efficiency FAMA perovskite by anti-solution method.....	76
3.4 Conclusion .....	87
References.....	89
Chapter 4 Multiple cations lead trihalide perovskite for solar cells with higher stability, reproducibility and highest efficiency. ....	91
4.1 Introduction.....	91
4.2 Experiments .....	92
4.3 Results and discussion .....	94
4.3.1 The nucleation kinetics of perovskite .....	95
4.3.2 Nature of fluorescence mechanism in Cs5FAMA perovskite .....	96
4.3.3 Discussion on the phase changes in perovskite .....	99
4.3.4 Discussion on the perovskite thermo-stability.....	102
4.3.5 The charge carriers lifetimes.....	105
4.3.6 Design and discussion of the charge extraction layers .....	106
4.3.7 The properties of Cs5FAMA perovskite solar cells.....	110
4.4 Conclusion .....	118
References.....	120
General conclusion and perspectives .....	123
List of figures.....	126
List of tables.....	132
List of the abbreviations and symbols .....	133

## General introduction

The sun is a huge ball of very hot gas, mostly composed of hydrogen and helium, which supplies a huge, continuous, renewable and cheap energy to the earth. Human beings never give up grabbing renewable energy from sun. In photovoltaic devices, this energy can be converted into electricity that can be conveniently employed and stored.

Since the 50's, photovoltaics is a field in continuous development, from the first developed crystalline silicon to thin film solar cells, and then to the more recent dye-sensitized solar cells (DSSCs) and organic solar cells. Recently, a new family of very promising solar cells, derived from DSSCs, appeared based on new absorber materials, the hybrid (organic and inorganic) perovskites (HPs). In perovskite solar cells (PSCs), compounds with a general formula  $ABX_3$  replaces the pigment in DSSCs, and exhibits an extremely high optical absorption coefficient and a tunable bandgap via composition change. Meanwhile, to improve the device stability, traditional liquid electrolyte is replaced by a solid-state hole transporting material (HTM). Based on these advanced improvements, the power conversion efficiency (PCE) of PSCs has steadily and rapidly increased from 3.8% to certified 22.7% within a few years.

In this thesis, we have optimized the  $TiO_2$  hole blocking layer (BL) and we have investigated multiple monovalent cation (A in  $ABX_3$ ) perovskite compounds for PSC application. Finally we realized a series of stable, reproducible and highly efficient PSCs.

Chapter 1 is a bibliographic review of solar cells and PSC components, as well as a description of the main techniques employed for the device characterizations. In addition, we further introduce perovskite solar cells development and revolution in the past few years, including the progress achieved in the various functional layers, cells structure, and some other hot-point studies of PSCs.

In Chapter 2, we will develop our study on the key parameters that render the  $TiO_2$

blocking layer (BL) efficient in PSCs. Several BLs have been prepared using the aerosol spray pyrolysis and the spin-coating techniques. Besides, we develop the use of the impedance spectroscopy technique to investigate the various processes taking place in the cells under illumination and how they are influenced by the BL. The optimal  $\text{TiO}_2$  blocking layer was employed to get relatively high efficiency  $\text{CH}_3\text{NH}_3\text{PbI}_3$  photovoltaic devices.

In Chapter 3 we will develop two kinds of perovskite deposition techniques avoiding a dripping step: the simple direct film-forming and the hot-casting methods. The direct film-forming without dripping process could be used for deposition at the large scale. The hot-casting technology realized a dense, big-grain, and pure phase perovskite layer. In this Chapter 3 we investigate the promotion of spontaneous crystallization and growth of FAMA ( $\text{FA}_{0.83}\text{MA}_{0.17}\text{Pb}(\text{I}_{0.83}\text{Br}_{0.17})_3$  (with FA the formamidinium cation and MA the methylammonium one) perovskite by the control the supersaturation concentration of the precursor solution. In the last section, we will adopt an anti-solvent dripping step to trigger crystallization and finally realize high efficiency perovskite photovoltaic devices.

In Chapter 4, the effect of adding 5% of Cs cation into the dual cations FAMA perovskite will be studied. We will analyze the early period nucleation kinetic of these materials before heating treatment, and discuss mixed-phases (other non-photoactive phases) that affect both FAMA and Cs5FAMA perovskite solar cells. Undesired mixed-phases in the FAMA perovskite will be identified. We will study the photoluminescence mechanism in FAMA and Cs5FAMA and study the charge injection to the adjacent charge collecting layers. Based on these fundamental data, high efficiency, reproducible, and stable devices with Cs5FAMA perovskite will be prepared.

Finally, we will provide a general conclusion of this work and give some perspectives.

# Chapter 1 Context

## 1.1 Introduction

### 1.1.1 Solar energy

The sun is a huge ball of very hot gas, mostly composed of hydrogen and helium. The two light hydrogen nuclei combine to produce a fusion reaction which releases a helium nuclei and energy due to a slight mass loss.  $E = \Delta mc^2$  “A tiny loss of mass produces a huge liberation of energy” making our earth so wonderful and unbelievable. Without the sun, there would be no life on earth. We depend on the sun for obtaining energy all the time.

The traditional source of energy is coming from fossil fuels. At the same time, a mass combustion brings the terrible environmental damages, the particles matter (PM 2.5) increasing in air[1] and global warming caused by the continuous increasing of CO<sub>2</sub> in the atmosphere.[2] In addition the globe energy crisis problem is coming, lacking of fossil fuel will be more and more prominent as time goes on.[3]

Therefore, the sustainable and renewable energies such as wind, photovoltaics, hydropower and others will play an increasing role in the future. The report ‘Renewable Energy Capacity Statistics 2015’ released by the International Renewable Energy Agency, provides the most comprehensive, up-to-date information on renewable energy capacity around the world (see Figure 1.1).[4] It presents trends in the development of the renewable energy sector, noting that over 100 GW of new renewable power capacity has been added every year since 2011.

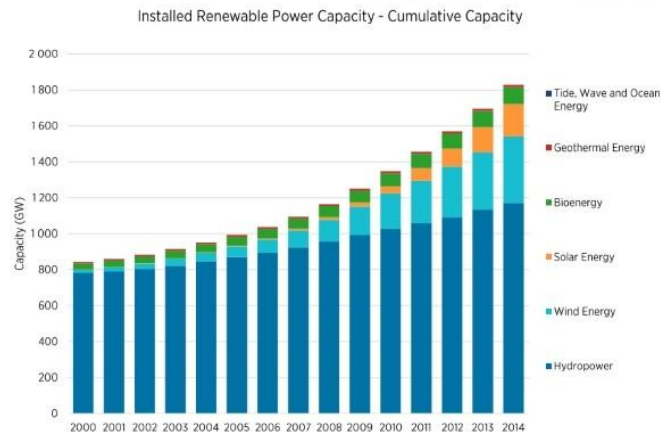


**Figure 1.1** Renewable power capacity and cumulative capacity, from the report Renewable Energy Capacity Statistics 2015 by International Renewable Energy Agency (IRENA).

### 1.1.2 Standard solar spectral irradiance

The actual solar spectrum received by a photovoltaic device will vary due to the weather, season, time of day and location. Therefore, the standard spectra are defined to allow the performance comparison of photovoltaic devices from different manufactures and research laboratories.

The spectra are standardized by the American Society of Testing and Materials Group (ASTMG). Figure 1.2 provides three main standardized spectra.[5] The standard spectrum for space applications is referred to as Air Mass zero (AM0), based on ASTM standard E 490. It has an integrated power of  $1366.1 \text{ W/m}^2$ . Due to the absorption and scattering when sunlight passes through the atmosphere, the solar spectral irradiance is decreased. Two standards are defined for terrestrial use, based on ASTM standard G173-03. The AM1.5 Global spectrum is designed for flat plate modules and has an integrated power of  $1000 \text{ W/m}^2$  ( $100 \text{ mW/cm}^2$ ). The AM1.5 Direct (circumsolar) spectrum is defined for solar concentrator work. It includes the direct beam from the sun plus the circumsolar component in a 2.5 degrees disk around the sun. The direct plus circumsolar spectrum has an integrated power density of  $900 \text{ W/m}^2$ .

Since perovskite photovoltaic devices aim at being used on earth and without concentration, the cells prepared during this thesis were measured under standard AM1.5 G solar illumination.

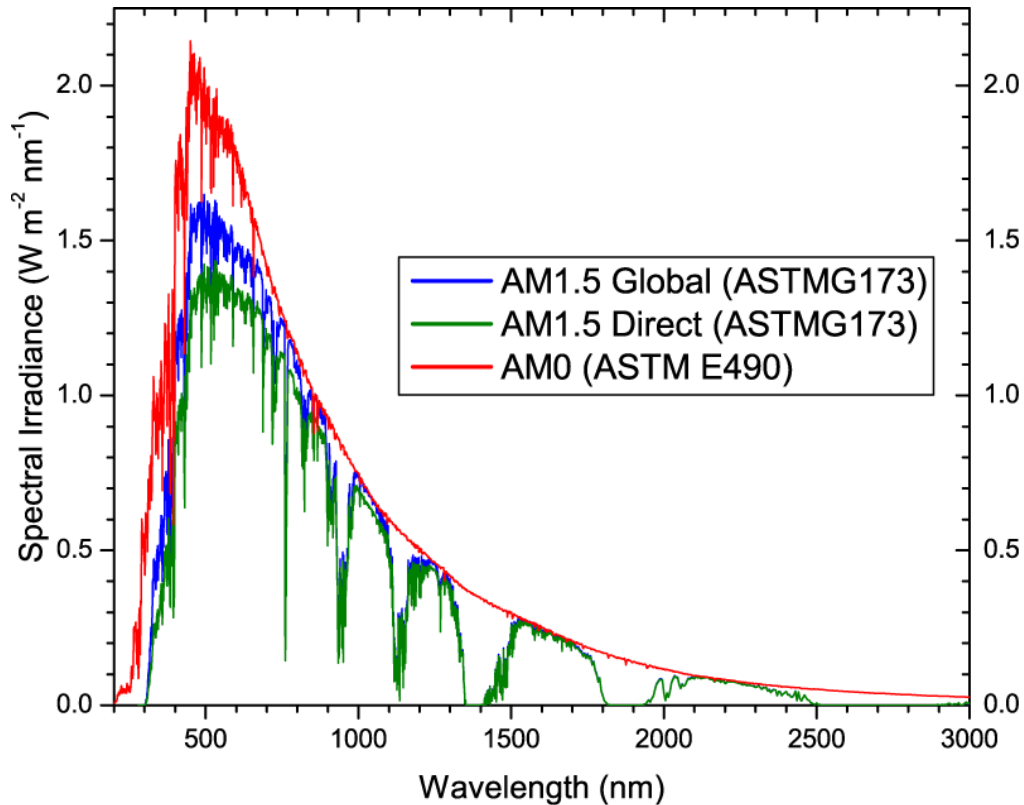


**Figure 1.2** Reference solar irradiation spectra according to the standards by the American Society of Testing and Materials.

## 1.2 Several kinds of photovoltaic solar cells

Photovoltaic solar cells are harvest sunlight devices which can absorb sunlight energy and convert it to electrical energy. Generally speaking, sunlight excites charge carriers or excitons in the corresponding absorber materials, the charge carriers are then separated to achieve the accumulation of electrons on one side and holes on the other side, then the charges are separated to produce a current.

Depending on the absorber materials, photovoltaic solar cells are divided into various technologies such as silicon solar cells [6, 7], dye-sensitized solar cells[8, 9], organic solar cells (such as polymer solar cells)[10, 11]. The perovskite solar cells, based on hybrid perovskite absorber materials, are newcomers and the most advanced

promising technology.[12] In the following, we will introduce several main families of photovoltaic devices.

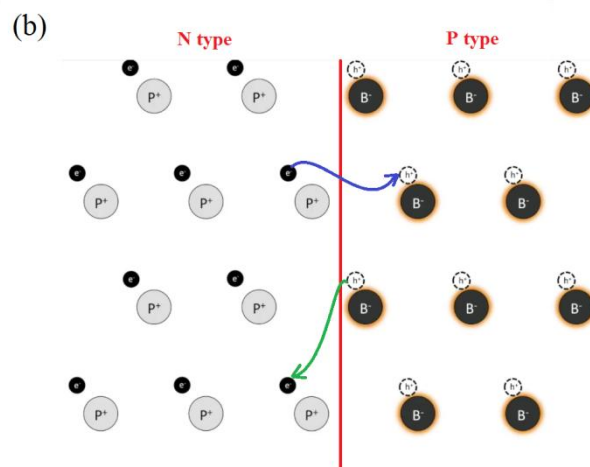
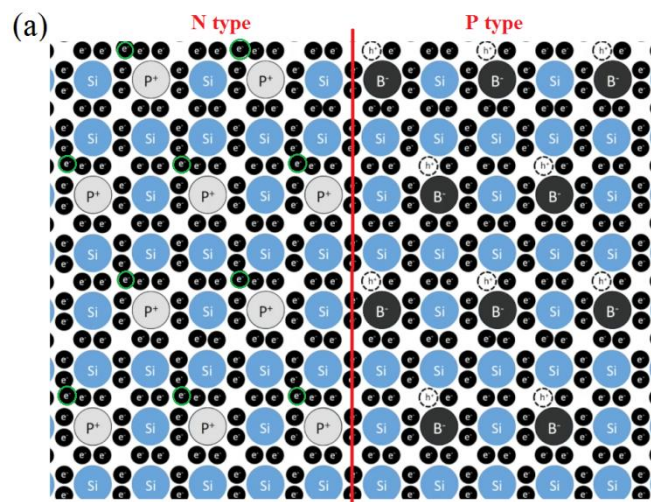
### **1.2.1 Silicon solar cells**

The first generation of photovoltaic solar cells is mainly based on crystalline silicon solar cells. It represents the main photovoltaic products on the commercial market at present (more than 90% of the market share).[13] However, the growth of crystalline silicon requires a high temperature melting which increases their fabrication cost and requires high energy consumption.[14] Therefore silicon solar cells have long period of cost recovery time. Fortunately, the silicon photovoltaic material is very stable and can be productive for several decades lasting periods.

Silicon solar cells are based on a p-n homojunction which produces a built-in electric field. It is noteworthy that the p-n homojunction is a characteristic for silicon solar cells, which is different to the dye-sensitizer solar and perovskite solar cells discussed in the following.

The understanding of the charge carrier separation and functioning mechanism is very necessary. The silicon absorber can be produced as two types of semiconductor materials, p-type and n-type, depending on doping. When the silicon lattices are doped by boron (or by another element of the group III column of the periodic table), this element traps the free electrons and release free holes leading to an excess of mobile holes. The semiconductor is then p-type doped. Similarly when silicon lattices are doped by phosphorus (or another element of the group V column), valence electrons have the tendency to be release and the concentration of mobile electrons increases, the semiconductor (SC) is n-type (see Figure 1.3a). All the excess charges are free to move around randomly. When two types semiconductors are contacted each other, a p-n junction is formed. Due to the opposite charges attract each other, excess electrons in the n-type will flow into the p-type to recombine with excess holes, resulting in the electron-hole neutralize and effectively vanish. Similarly, holes also can flow toward the n-type semiconductor (Figure 1.3b). Consequently, electrons and

holes randomly diffuse and neutralize continuously at the p-n junction. The total number of mobile charges decreases continuously near the p-n junction. It results in a strong built-in electric field (i.e. a space charge region (SCR) where the charges are exhausted) and the charges diffusion process will be stopped (Figure 1.3c). Under sunlight irradiation, electron of silicon is excited near the SCR, produces a hole and starts to move randomly (Figure 1.3d). Due to the presence a strong built electric field in the SCR, the electron will only randomly diffuse in the n-type zone while the hole will drift in the SCR (Figure 3e). Finally, the charge carriers separation is realized. In the closed circuit, the electrons will travel through the external wire and finally reach the p-type zone where they will combine with holes and finally generate a continuous current in the external circuit.



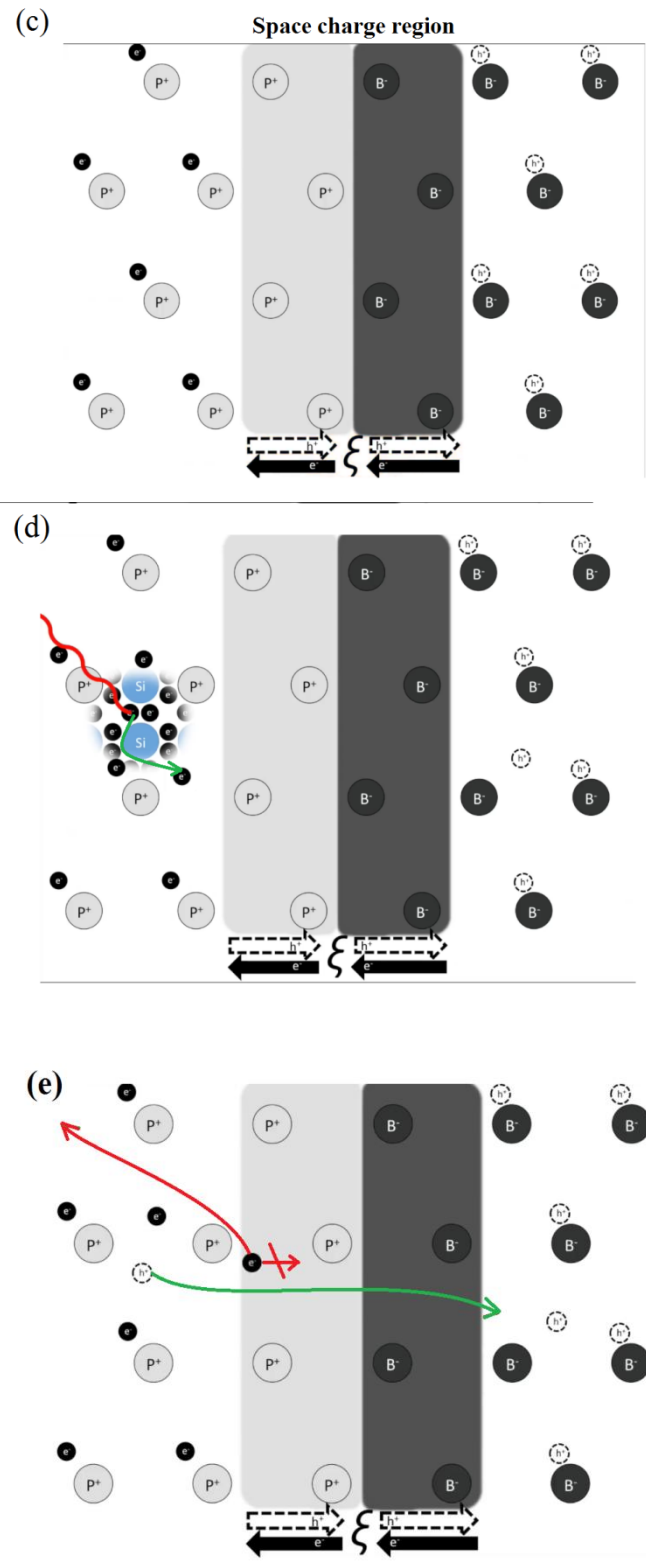


**Figure 1. 3** Silicon solar cells operating mechanism. (a) Silicon materials doping to form p-type and n-type semiconductor. (b) p-n junction formation. (c) Formation of the built-in electric field. (d) A pair of electron-hole formation after sunlight irradiation. (e) Realized charge carriers separation and current generation.

## 1.2.2 Dye-sensitized solar cells

Dye-sensitized solar cells (DSSCs) are photoelectrochemical cells that have gained a widespread attention because of low-cost production.[15] It is based on a junction formed between a photo-sensitized anode and an electrolyte forming a photoelectrochemical system. The first low cost, high-efficiency dye-sensitized solar cell was reported in 1991 by M. Grätzel's group.[16] At present, the highest efficiency lies around 13% (11.9% for a certified cell). It has been achieved by using a porphyrin-sensitizer and a liquid electrolyte.[17] Although the liquid electrolyte presents a serious challenge for making DSSCs useable for very long time without degradation, this technology presents a good performance/price ratio that could allow DSSCs to compete with crystalline silicon solar cells by grid parity.[18]

Generally speaking, a typical Dye-sensitized solar cell includes a titanium dioxide nanoparticles photo-anode sensitized to solar light by a dye, an opposite electrode and an electrolyte containing a redox couple system and additives.[19, 20] The specific DSSC photovoltaic device architecture is shown in Figure 1.4.[21]

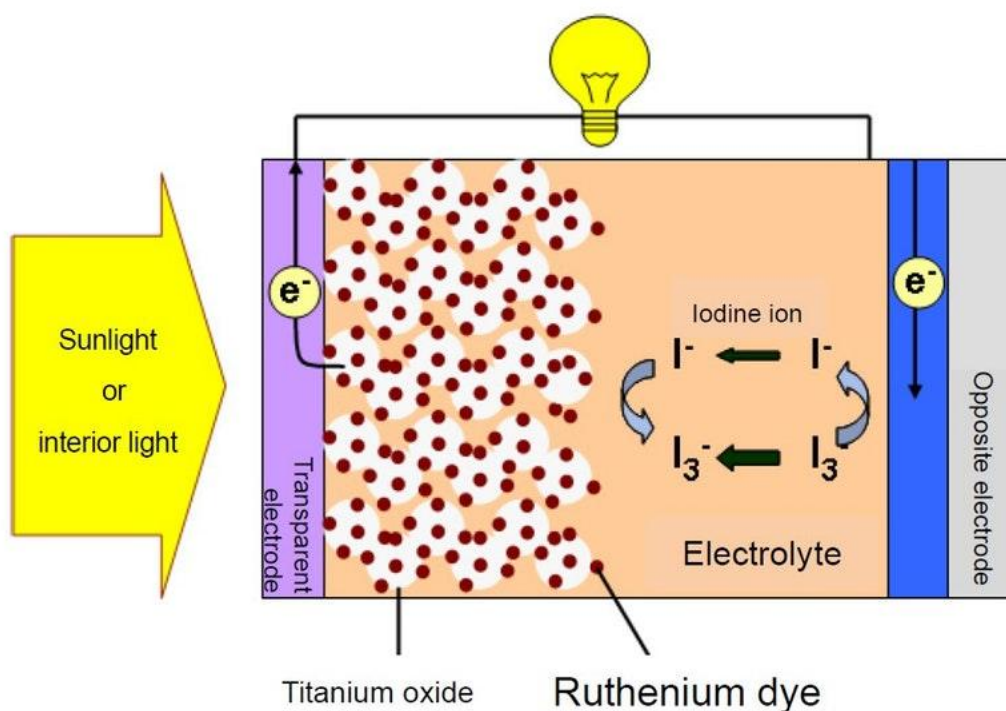
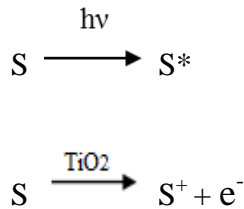


**Figure 1. 4** Device architecture of a typical liquid dye-sensitized solar cell.[21]

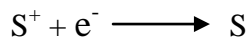
In here, with the help of Figure 1.5, we explain the DSSCs operation mechanism in detail. It will help following discussions on perovskite solar cells [22] because the first perovskite solar cells were derived from traditional DSSCs.

Charge carriers generation processes: At the beginning, the incident photons are absorbed by the dye-sensitizers anchored onto TiO<sub>2</sub> nanoparticle film. Generally, a Ru-complex photosensitizer (N719) is used as the dye. [23, 24] The photosensitizers are excited under sunlight, the electrons are excited from the ground state (S) to the excited state (S\*). At the same time, the electric charge is transferred to the TiO<sub>2</sub> wide bandgap oxide and it results in the oxidation of the photosensitizer (S<sup>+</sup>).

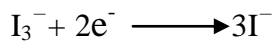


Electrons diffusion processes: The electrons, injected into the conduction band of TiO<sub>2</sub>, are transported by diffusion between the TiO<sub>2</sub> nanoparticles toward the transparent conducting oxide (TCO) front contact. Finally, the electrons reach the counter-electrode (CE) through the external circuit.

Electrolyte redox reaction: The oxidized photosensitizer (S<sup>+</sup>) accepts electron from the I<sup>-</sup> ion redox mediator leading to regeneration of the ground state (S), and two I<sup>-</sup> ions are oxidized to elementary iodine which reacts with I<sup>-</sup> to the oxidized state I<sub>3</sub><sup>-</sup>.



The oxidized redox mediator, I<sub>3</sub><sup>-</sup> diffuses toward the counter electrode and then it is reduced to I<sup>-</sup> ions.



It is noteworthy that just electrons are transported by diffusion mechanisms in dye-sensitized solar cell. The photogenerated electrons pass through the external circuit and flow into electrolyte where the redox reaction occurs.

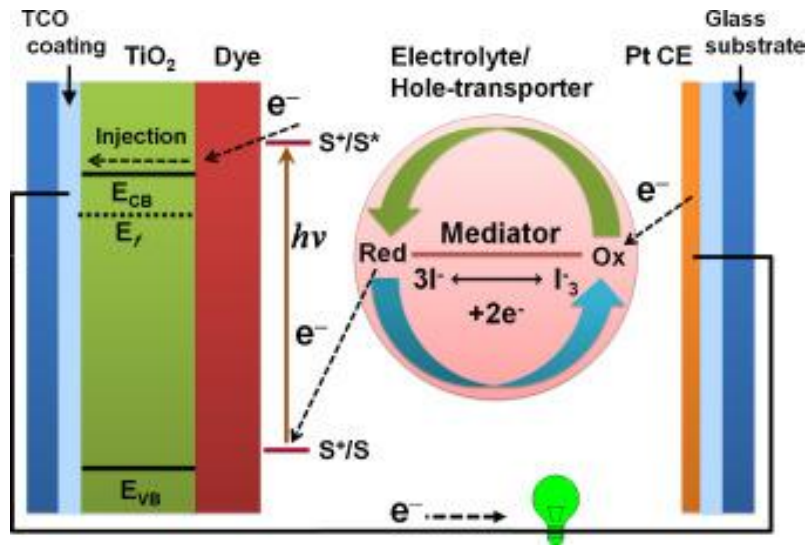


Figure 1. 5 Dye-sensitized solar cell device working mechanism.[22]

## 1.3 Perovskite solar cells

### 1.3.1 Developing of Perovskite solar cells

As discussed above, silicon solar cell has a p-n junction to form a built-in electric field. This electric potential field allows an effective separation of electrons and holes. In the DSSCs, a liquid electrolyte is used as a redox system. However, this electrolyte can be replaced by a solid hole transporting material (HTM), and covered a top metal counter electrode to constitute a solid-state dye-sensitized solar cells (ssDSSCs). In addition, the dye-sensitizer (such as the N719 dye and other pigments) can be replaced by a new inorganic and organic hybrid lead trihalide material (i.e. perovskite) to constitute a new family of solar cells. These photovoltaic devices are called perovskite solar cells (PSCs). Therefore the perovskite solar cells are derived from the DSSCs. However, further studies showed that the mesoporous  $\text{TiO}_2$  has to be quite thin (several hundred nm) and the perovskite layer had to be quite thick (several hundred nanometers) for getting record efficiencies. Moreover, earlier studies showed that the mesoporous  $\text{TiO}_2$  layer could be replaced by a mesoporous layer made of insulating  $\text{ZrO}_2$ . It has been also shown that planar architectures, without mesoporous  $\text{TiO}_2$  layer can work very effectively, just by using a compact thin  $\text{TiO}_2$  layer, or better, by using a compact  $\text{SnO}_2$  layer.

The perovskite solar cells have attracted a widespread attention in recently years. The power conversion efficiency of these devices has followed an unprecedented rapid rise from 3.8% to 22.7% within a few years. Figure 1.6 shows the evolution of the certified record for single junction perovskite solar cells which achieved a 22.7% efficiency in 2017. The rapid development of perovskite solar cells promote to form a independent solar cell branch—perovskite solar cell. The correlative mechanism, theory, and a series of new materials are developing, and the perovskite solar cell is the most cutting-edge research in photovoltaic field, which enforced power conversion efficiency (PCE) rapidly increasing just in the past several years (see Figure 1.7).

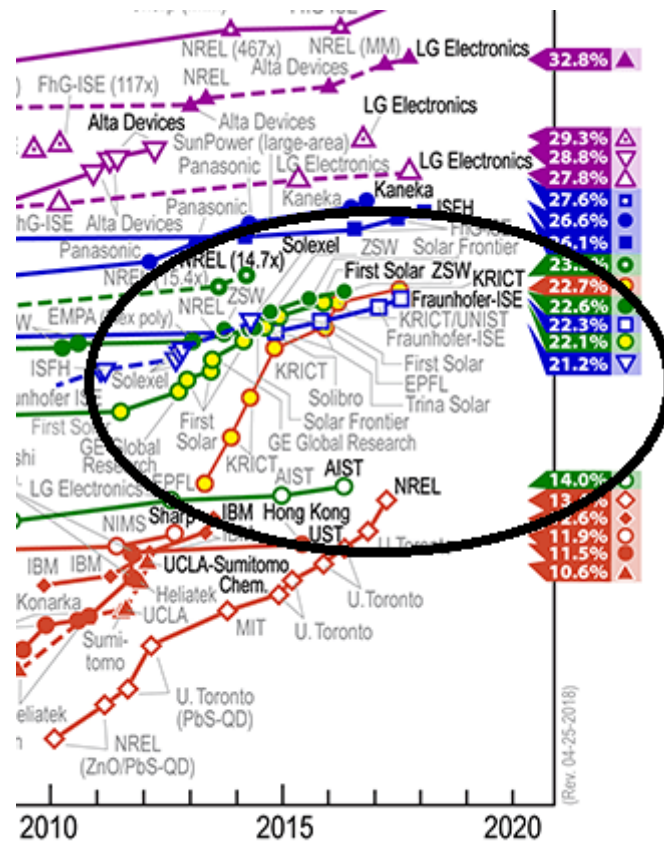


**Figure 1.6** Chart of perovskite solar cell efficiency records by the National Renewable Energy Laboratory (NREL).[25]

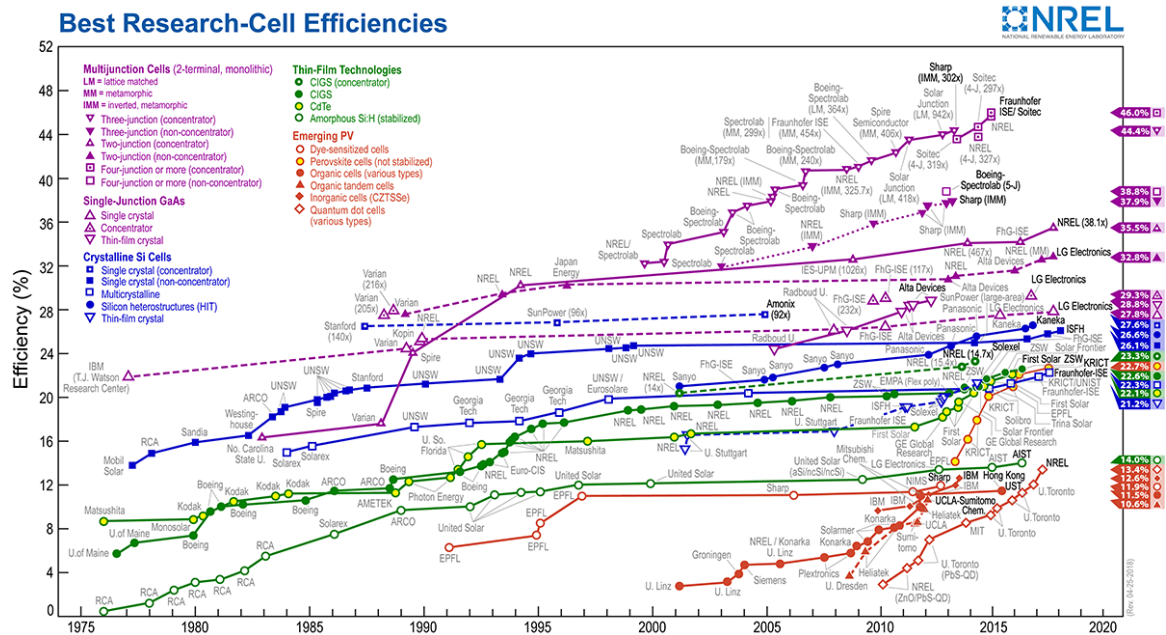


**Figure 1.7** Performance evolution chart of the best certified research cell efficiencies as published by NREL.[25]

### 1.3.2 The perovskite component

Historically, the term perovskite was used to describe the materials with the same type of crystal structure as calcium titanium oxide ( $\text{CaTiO}_3$ ), which was discovered in 1839 by the mineralogist Gustav Rose (named perovskite in honor of the Russian mineralogist Lev Alexe ÷vitch Perovski).[26] However, the discovery of organometal halide perovskite, mixing both organic and inorganic components by D. Weber is much more recent (1978).[27, 28] Their chemistry and descriptions have been then developed by several groups, in particular by D.B. Mitzi and co-workers.[29, 30] Depending on their structure, one can distinguish the 3D and 2D halide perovskite compounds. Most of them are direct bandgap semiconductors with a high light absorption coefficient.

The 3-dimensions organic-inorganic hybrid perovskite material has an  $\text{ABX}_3$  structure, where A is typically an organic cation (methylammonium,  $\text{MA}^+$ ; formamidinium,  $\text{FA}^+$ ) but can also be the cesium cation ( $\text{Cs}^+$ ). A is 12-fold cuboctahedral coordinated to X anions. B is a divalent metal cation B ( $\text{Pb}^{2+}$ ,  $\text{Sn}^{2+}$ ,  $\text{Ge}^{2+}$ ), and X is an anion ( $\text{Cl}^-$ ,  $\text{Br}^-$ ,  $\text{I}^-$ ).

The ideal cubic-symmetry perovskite structure has the B cation in 6 fold coordination, surrounded by the  $BX_6$  octahedron anions, and  $BX_6$  octahedron are corner-connected to form a three dimensional framework (see Figure 1.8). Due to the presence of a rather big space in the center of the cubic perovskite structure, small organic cations can fill the formed cage. The most miraculous is that, when the various A cations are adopted, it can distort the perovskite crystal structure and further induces many physical and chemistry properties. Especially, the electronic, magnetic, ferrimagnetism, and ferroelectric properties of the material [31] depend on the details of these distortions, which are important for the application of perovskite material.[32, 33]

In the photovoltaic field, organic-inorganic hybrid perovskite is easy to synthesize at low temperature by processes using solutions. Perovskite have strong panchromatic absorption of sunlight especially in the visible-light wavelength. In addition, perovskite are direct semiconductors with a tunable energy bandgap between 1.2 eV to 2.2 eV by adjusted chemical compositions engineering. Low exciton binding energy is approximate 10 meV and long charge carrier diffusion length is around 1  $\mu\text{m}$ , especially in single crystals, which is guaranteed that charge carries can be effective separated. And their charges mobilities are roughly  $10 \text{ cm}^2 \text{ v}^{-1} \text{ s}^{-1}$ . These unique photophysical and optoelectronic properties explain why perovskite solar cells achieved very high power conversion efficiency, low-costing and convenient fabrication.

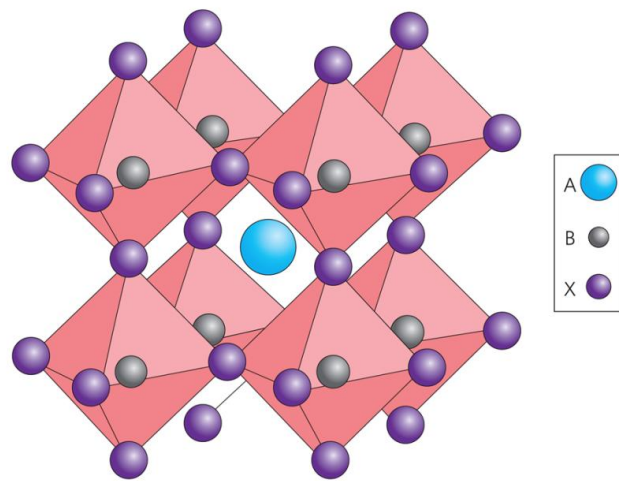


**Figure 1. 8** Ball and stick model of generic  $ABX_3$  perovskite structure.[34]

### 1.3.3 Structure of perovskite solar cells

If the initial structure of the PSC was based on DSSCs (using a liquid electrolyte and perovskite nanocrystals for sensitization), the major breakthroughs in the field were realized in 2012 when a solid HTM (typically Spiro-OMeTAD) was employed to replace the liquid electrolyte (in which the perovskite is dissolved, making the devices unstable) and with the use of rather thick perovskite layers of typically 400 nm thickness.[35] With the development of perovskite solar cells (PSCs), the device structure and configuration also presents a series of evolution and change. For example, the inverted structure PSCs [36, 37, 38], planar PSCs [39, 40], and mesoscopic PSCs [12, 41, 42] have been developed in parallel. In the inverted structure devices, the hole extracting layer is deposited on ITO substrate, the electron extraction layer is prepared on top of the perovskite layer and the back contact is deposited on this layer. It is completely the opposite to the ‘normal’ or standard PSCs structure. Very recently, an inverted structure device has been reported to achieve an efficiency above 20%.[43]

In here, we mainly introduce the ‘normal’ or standard perovskite solar cell structure. As shown in Figure 1.9, these PSCs consist in an electron transporting layer (including a compact hole blocking and a mesoporous layer), a perovskite layer, a hole transporting layer, and a metal back-contact electrode. The energy levels matching for the various functional layers will decide the device structure and the final efficiency.

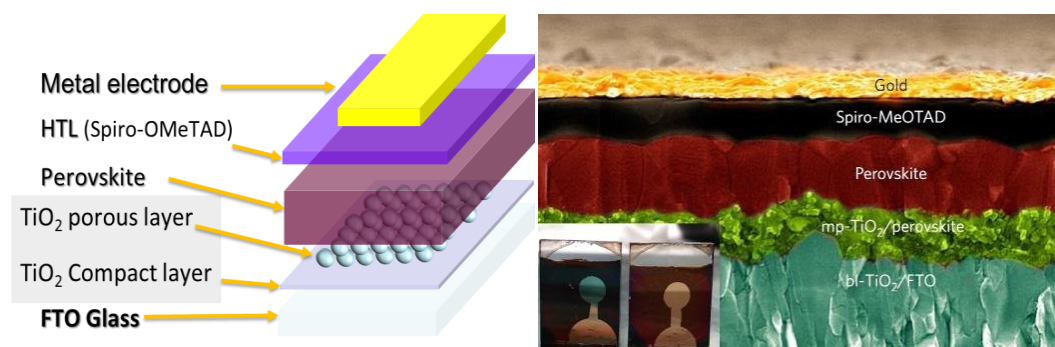


**Figure 1.9** Standard structure of perovskite solar cells and functional layer assemblies (the left schematic). Cross section SEM image of a standard perovskite solar cells (right image). The insets are pictures of FAMA and Cs5FAMA –based perovskite solar cells.

### **1.3.3.1 The electron transport layer**

In order to prevent charge carriers recombination on transparent conducting oxide (TCO), one must first avoid the direct contact between the F-doped tin oxide (FTO) and the perovskite. Therefore, a dense metal oxide hole blocking layer is deposited that must completely covers the FTO surface. In addition, through the energy levels matching between the compact metal oxide and the perovskite, promoted electrons must be rapidly injected into the metal oxide conduction band from perovskite. Generally speaking, the electron transporting layer (ETL) of high efficiency PSCs consists in a bilayer structure: a compact layer capped by a mesoporous layer (see Figure 1.9). In the chapter 3 and 4, we will show that, in the case of  $\text{TiO}_2$ , a double layer ETL can extract more efficiently the photogenerated electrons.

Several techniques have been developed to fabricate the metal oxide ETL. Aerosol spray pyrolysis and spin-coating are the most commonly techniques used.[35][44] The typical thickness of a blocking layer ranges between 20 and 100 nm, which can be controlled by the concentration of the precursor solution and the spin-coating time.[45] The mesoporous  $\text{TiO}_2$  layers are prepared from a nanoparticle solution at the accurate concentration, spin-coated on top of the hole blocking layer. In the Chapter 2, we will detail various techniques and precursor solutions for the preparation of the  $\text{TiO}_2$  hole blocking layer in PSCs and their effect on the cell performances and functioning.

### **1.3.3.2 The perovskite layer**

Absorber materials for the solar light harvesting must have a broad and strong absorbance over the visible to near infrared region of the solar spectrum. Shockley

Queisser efficiency limit theory gives maximum efficiency at the band gap of 1.34 eV.[46]

These bandgap values determine the strength of electrical field which is related to the open circuit voltage of the solar cell. When the bandgap value is too low, a wider solar spectrum will be covered and this absorber material will collect extra current by absorbing more photons. However, it also results in a smaller voltage. On the other hand, a larger bandgap value will generate a lower current (due to a narrower absorption wavelength range for light) and a higher voltage. In this case, to balancing these two effects, the optimal band gap for a single junction solar cell is between about 1.4-1.5 eV.[47]

The organic-inorganic hybrid perovskites have attracted a widespread attention, because their optical bandgap can be varied by changing the A cation, the metal cation and/or the halide anion.

The bandgap of traditional perovskites such as  $\text{CH}_3\text{NH}_3\text{PbI}_3$  and  $\text{CH}_3\text{NH}_3\text{PbI}_{3-x}\text{Cl}_x$  usually used in the literature, is 1.58 eV[47, 48] and 1.55 eV[49], respectively. Later, some research groups found that pure formamidinium (FAPbI<sub>3</sub>) perovskite also achieved 14.2% efficiency for a bandgap of 1.48 eV.[47] In addition, one cation that has recently attracted much attention in mixed cation perovskite is the inorganic cesium ( $\text{Cs}^+$ ) which ionic radius is 1.81 Å [50, 51]. It is considerably smaller than  $\text{MA}^+$  (2.70 Å) or  $\text{FA}^+$  (2.79 Å).[52] In the  $\text{FA}_{0.9}\text{Cs}_{0.1}\text{PbI}_3$  perovskite,  $\text{FA}^+$  is partially replaced by  $\text{Cs}^+$ , the device PCE was enhanced to 16.5%.[53] Michael Saliba et al. found that the completely inorganic of  $\text{CsPbI}_3$  perovskite can be crystallized at high temperature and with a bandgap at around 1.73 eV.[54] Finally the  $\alpha\text{-CsPbI}_3$  (PSCs) displayed an highly reproducible efficiency of 11.8%.[55]

Concerning the influence of the metal cation, taking the example of  $\text{AMI}_3$  (M=Sn, Pb), the band gap of  $\text{ASnI}_3$  (1.20 eV) is lower than that of  $\text{APbI}_3$  (1.58 eV).[56] Researchers have investigated the influence of the halide anion, the mixed-halide ( $\text{I}_{1-x}\text{Br}_x$ ) composition also adjusted perovskite bandgap value from 1.48 to 2.3 eV in  $\text{FAPb}(\text{I}_{1-x}\text{Br}_x)$ .[57]

Recently, the MA/FA mixtures demonstrates that a small amount of MA is already

sufficient to induce a preferable crystallization into the photoactive phase of FA perovskite resulting in a more thermally and structurally stable composition than the pure MA or FA compounds.[58, 59] This illustrates that MA can be thought as a “crystallizer” of the black phase FA perovskite.[50, 60, 61, 62] We found the MA/FA mixed perovskite is a research hot spot, because it presents excellent properties and PCE record.[54, 59, 60, 61]

Many deposition techniques of perovskite layers have been developed in the literature. The common film deposition methods are so called one-step precursor solution depositions [63] and the two-step sequential deposition method.[44] Besides, several groups have developed the vacuum-assisted method[64], the hot-casting method [37] and the anti-solvent methods [65, 66]. It is noteworthy that anti-solvent dripping treatment is successfully used to trigger perovskite crystallization. S. Paek et al. studied the effect of various anti-solvents on perovskite crystallization.[67] The dual-source vapor deposition method permits to prepare an extremely uniform perovskite layer. An efficiency of 15.4% was reported by Liu et al.[68] Y. Yang’s group reported a low-temperature vapor-assisted solution process to get perovskite film with full surface coverage, and finally achieved a PCE of 12.1%.[40] Michael Grätzel’s group adopted a vacuum flash-assisted solution process for the perovskite layer preparation and attained high certified PCE of 19.6%.[69]

### **1.3.3.3 The hole transporting layer**

The hole transporting layer (HTL) is another key components in perovskite solar cells. It is used to extract holes and inject holes into the back contact in PSCs. Various materials have been explored as HTM, ranging from low HOMO molecular[70], polymers[71, 72] and inorganic component such as CuI [73] or CuSCN[74]. In a typical perovskite solar cell, the most commonly used hole transporting material (HTM) is 2,2',7,7'-tetrakis-N,N-di(4-methoxyphenyl)amine-9,9'-spirobifluorene (noted Spiro-OMeTAD). The molecular structure of Spiro-OMeTAD is depicted in Figure 1.10. Spiro-OMeTAD is an amorphous organic p-type semiconductor with a

large bandgap (at about 3.0 eV). This compound has a hole mobility in the range of  $1 \times 10^{-5}$  to  $1 \times 10^{-4} \text{ cm}^2 \text{ V}^{-1} \text{ s}^{-1}$  as reported in the literature.[75, 76] The advantage of spiro-OMeTAD is its good ability to pore filling due to the high solubility in toluene and chlorobenzene organic solvents.

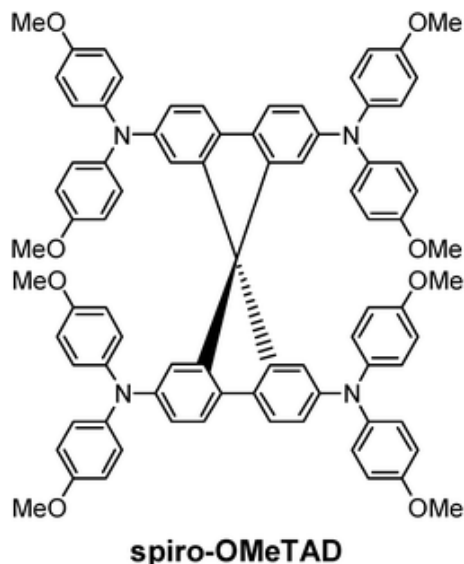


**Figure 1. 10** Molecular structure of 2,2',7,7'-tetrakis-N,N-di(4-methoxyphenyl)amine-9,9'-spirobifluorene (Spiro-MeOTAD), utilized as HTM in PSCs.

Pristine spiro-OMeTAD has high resistivity. Therefore, non-doped Spiro-OMeTAD HTM usually cannot achieve high efficiency. Generally speaking, several additives are added to Spiro-OMeTAD solution to improve its rapid holes transporting properties. The common additives are: 4-tert-butylpyridine (TBP), lithium bis(trifluoromethylsulfonyl)imide (LiTFSI) attributed, and tris(2-1H-pyrazol-1-yl)-4-tert-butylpyridine)-cobalt(III)-tris(bis-(trifluoromethylsulfonyl)imide) (a cobalt complex which directly oxidizes the Spiro-OMeTAD). However, these additives into HTM bring some problems to PSCs. Especially, the 4-tert-butylpyridine (TBP) and Li complex chemicals could react with the counter electrode.[77, 78] In addition, some researchers think that the Spiro-OMeTAD dopants can diffuse into the metal electrode causing irreversible degradation.[79, 80] Therefore, some researchers turn to studying new HTM materials. For example, Yi Hou et al. reported that using Ta-WO<sub>x</sub>/conjugated polymer PDCBT in the hole

extraction layer realizes high efficiency and stable working PSCs.[81] Besides, Neha Arora et al. reported that using configuration of CuSCN/graphene oxide HTL allows the achievement of high efficiency, around 20%, and that the PSCs retain > 95% of their initial efficiency after a 1000 hour of functioning.[82] It is observed that Spiro-OMeTAD maybe not the best candidate for HTM in PSCs.

### **1.3.3.4 The back contact electrode**

The back contact electrode of PSCs usually use silver or gold thin film formed by the thermal evaporation technique. Silver is more used than gold, due to a lower cost. However, the gold back electrode can supply a suitable work function, which promotes the achievement of a high voltage for photovoltaic devices. Compared to the expensive silver and gold contacts, the low-cost carbon materials have attracted some attention especially with the layer preparation by screen printable deposition techniques.[41] Moreover, the carbon layer can work as a water repellent layer to protect the cell from water, and improves the stability of PSCs devices.[83] [84]

## **1.4 Characterization and analysis of Perovskite solar cells**

### **1.4.1 Solar cell's characterization**

#### Current-Voltage (J-V curves) characteristics

The solar cells were measured under a one sun illumination provided by a solar simulator (Abet Technology Sun 2000) using a 150 W xenon light source. The light intensity was calibrated with a Si photodiode. Current-voltage characteristics of the cells were obtained by applying an external voltage bias while measuring the current response with a digital sourcemeter (Keithley 2410). The voltage scan rate was 25 mV s<sup>-1</sup> and no device preconditioning, such as light soaking or extended forward voltage biasing in the dark, was applied before starting the measurement. The cells were masked with metal mask (0.076 cm<sup>2</sup>) to fix the active area and reduce the influence of the scattered light. The metal mask was calibrated by using an optical microscope

which has permitted to precisely measure the mask active area at  $0.076 \text{ cm}^2$ . The incident light intensity was adjusted to  $1000 \text{ W/m}^2$  in accordance with standard AM 1.5G spectrum (see Figure 1.2) by using a calibrated silicon solar cell.

#### Stabilized power output and stability measurements

Steady-state power output and stability of solar cells were performed with a Princeton Applied Research (EGG 273A model) potentiostat under the same solar simulator with standard AM 1.5G illumination. The devices were masked ( $0.076 \text{ cm}^2$ ) under the normal ambient atmosphere. After the opening of the shutter of the solar simulator, the devices were measured with a maximum power point (MPP) tracking routine, under the monitored potentiostat. 30 tracking points were recorded in 60 s. For stabilized power output experiments, the measurement time was 60 s. For photovoltaic devices stability experiments, the measurement time was 300 s.

#### External quantum efficiency (EQE)

In order to determine the ratio of collected charge to the incident photons, the external quantum efficiency was introduced. The devices were measured with a QuantX-300 apparatus from Newport Corporation equipped with a monochromator and a 150 W xenon lamp. The light beam was chopped at 25 Hz and the wavelength measurement ranged from 300 nm to 900 nm.

#### Impedance spectroscopy

The impedance spectra were measured at room temperature, between 600 kHz and 30 mHz, using a PGSTAT 30 apparatus from Autolab. All the measured cells had the same contact geometries. The alternating current (AC) signal was 20 mV. All the impedance spectra were measured at room temperature, over a large potential range (typically from 0V to 1V), both in the dark and under a  $\sim 1$  sun light power provided by a halogen Schott lamp. These spectra were analyzed using the Z-view software from National Instrument.

## 1.4.2 Materials characterization in PSC

### X-ray power diffraction

The various pristine perovskite films were measured by an X'Pert Pro diffractometer (Malvern Pananalytical) equipped with ceramic copper anode tube ( $\text{CuK}_\alpha$ ,  $\lambda = 1.5406 \text{ \AA}$ ). Diffraction patterns were collected for 15 min. The measurements were performed in Bragg-Brentano geometry  $2\theta = 8^\circ$  to  $80^\circ$ .

### Field emission scanning electron microscope (FE-SEM)

Scanning electron microscopy (SEM) was performed on a high-resolution scanning electron microscope (ZEISS Merlin). Secondary electron images were acquired with an EDX detector. Reflecting back scattering electron images were obtained with RBSE detector by split screen technology.

### Steady-state photoluminescence spectrum measurements

Photoluminescence spectra were recorded by exciting the perovskite films deposited on various extraction layers at 460 nm with a standard 450-W Xenon CW lamp. The signal was obtained on a spectrofluorometer (Fluorolog FL1065, Horiba Jobin Yvon Technology) in the 620 nm to 850 nm range. The samples were mounted at  $60^\circ$  and the emission recorded at  $90^\circ$  from the incident beam path.

### Time-resolved photoluminescence decay spectrum measurements (with single-photon counting, TCSPC technique)

The PL decay experiments were performed under microscope observation (numerical aperture 0.7). The sample was excited by a 470 nm diode laser (Picoquant). The emission was filtered by a 488-nm longpass filter. The emission signal was analyzed by a PerkinElmer SPCM avalanche photodiode combined with a PicoHarp acquisition card (500 ps characteristic time of the total system response function) used with the laser in a pulsed mode at a 0.14  $\mu\text{W}$  excitation power (pulse duration 70 ps).

### Steady-state absorbance spectrum measurements (with time increasing absorbance dynamic spectrum)

The absorption spectra (specular component) of the various layers were measured by a Varian Cary 5000 UV-Vis-NIR spectrophotometer.

For the study of perovskite nucleation kinetics in Chapter 4, the mesoporous TiO<sub>2</sub> layer were deposited on FTO glasses and infiltrated with perovskite precursor solution by spin-coating. Immediately, the sample was mounted into a special sample holder, and then the anti-solvent was rapidly injected on perovskite precursor film. The film optical absorption was then monitored at 495 ~ 500 nm wavelengths, and absorbance points were recorded by every single 6 second.

### Optical microscopy

Electronic optical microscopy was employed to precisely measure the metal mask surface area to obtain the accurate illuminated solar cell area.

## **References**

1. Peters A, Dockery DW, Muller JE, Mittleman MA. Increased particulate air pollution and the triggering of myocardial infarction. *Circulation*. 2001;103:2810-5.
2. Shakun JD, Clark PU, He F, Marcott SA, Mix AC, Liu Z, Otto-Bliesner B, Schmittner A, Bard E. Global warming preceded by increasing carbon dioxide concentrations during the last deglaciation. *Nature*. **2012**;484:49.
3. Rubin ES, Chen C, Rao AB. Cost and performance of fossil fuel power plants with CO<sub>2</sub> capture and storage. *Energy policy*. 2007;35:4444-54.
4. IRENA RELEASES WORLD'S MOST COMPREHENSIVE RENEWABLE ENERGY CAPACITY FIGURES. Available from: <https://irenanewsroom.org/2015/06/14/irena-releases-worlds-most-comprehensive-renewable-energy-capacity-figures/>.
5. Standard Solar Spectra. Available from: <https://www.pveducation.org/pvcdrom/appendices/standard-solar-spectra>.

6. Wenham S, Green M. Silicon solar cells. *Progress in Photovoltaics: Research and Applications*. 1996;4:3-33.
7. Goetzberger A, Knobloch J, Voss B. Crystalline silicon solar cells. editorial John Wiley & Sons Ltd. 1998;1.
8. Grätzel M. Dye-sensitized solar cells. *Journal of Photochemistry and Photobiology C: Photochemistry Reviews*. 2003;4:145-53.
9. Hara K, Arakawa H. Dye-sensitized solar cells. *Handbook of photovoltaic science and engineering*. 2003:663-700.
10. Würhle D, Meissner D. Organic solar cells. *Advanced Materials*. 1991;3:129-38.
11. Günes S, Neugebauer H, Sariciftci NS. Conjugated polymer-based organic solar cells. *Chemical reviews*. 2007;107:1324-38.
12. Grätzel M. The light and shade of perovskite solar cells. *Nature materials*. 2014;13:838.
13. Green MA. Commercial progress and challenges for photovoltaics. *Nat Energy*. 2016;1:15015.
14. Tairov YM, Tsvetkov V. Investigation of growth processes of ingots of silicon carbide single crystals. *Journal of crystal growth*. 1978;43:209-12.
15. Green MA. Third generation photovoltaics: advanced solar energy conversion. *Physics Today*. 2004;57:71-2.
16. O'regan B, Grätzel M. A low-cost, high-efficiency solar cell based on dye-sensitized colloidal TiO<sub>2</sub> films. *Nature*. 1991;353:737.
17. Mathew S, Yella A, Gao P, Humphry-Baker R, Curchod BF, Ashari-Astani N, Tavernelli I, Rothlisberger U, Nazeeruddin MK, Grätzel M. Dye-sensitized solar cells with 13% efficiency achieved through the molecular engineering of porphyrin sensitizers. *Nature chemistry*. 2014;6:242.
18. Eshetu GG, Armand M, Ohno H, Scrosati B, Passerini S. Ionic liquids as tailored media for the synthesis and processing of energy conversion materials. *Energy & Environmental Science*. 2016;9:49-61.
19. Gong J, Liang J, Sumathy K. Review on dye-sensitized solar cells (DSSCs): fundamental concepts and novel materials. *Renewable and Sustainable Energy*

Reviews. 2012;16:5848-60.

20. Hamann TW. The end of iodide? Cobalt complex redox shuttles in DSSCs. Dalton Transactions. 2012;41:3111-5.

21. Tanaka exclusively supply ruthenium dye for dye-sensitized solar cell. Available from:

<https://www.printedelectronicsworld.com/articles/4062/tanaka-exclusively-supply-ruthenium-dye-for-dye-sensitized-solar-cells>.

22. Yun S, Freitas JN, Nogueira AF, Wang Y, Ahmad S, Wang Z-S. Dye-sensitized solar cells employing polymers. Progress in Polymer Science. 2016;59:1-40.

23. Wang Z-S, Kawauchi H, Kashima T, Arakawa H. Significant influence of TiO<sub>2</sub> photoelectrode morphology on the energy conversion efficiency of N719 dye-sensitized solar cell. Coordination chemistry reviews. 2004;248:1381-9.

24. Lee KE, Gomez MA, Elouatik S, Demopoulos GP. Further understanding of the adsorption mechanism of N719 sensitizer on anatase TiO<sub>2</sub> films for DSSC applications using vibrational spectroscopy and confocal Raman imaging. Langmuir. 2010;26:9575-83.

25. NREL chart (2018) <https://www.nrel.gov/pv/assets/images/efficiency-chart.png>.

26. Mitzi DB. Templating and structural engineering in organic-inorganic perovskites. Journal of the Chemical Society, Dalton Transactions. 2001:1-12.

27. der Verbindungen TIS. CH<sub>3</sub>NH<sub>3</sub>PbX<sub>3</sub>, ein Pb (II)-System mit kubischer Perowskitstruktur.

28. Weber D. CH<sub>3</sub>NH<sub>3</sub>SnBr<sub>x</sub>I<sub>3-x</sub> (x= 0-3), ein Sn (II)-System mit kubischer Perowskitstruktur/CH<sub>3</sub>NH<sub>3</sub>SnBr<sub>x</sub>I<sub>3-x</sub> (x= 0-3), a Sn (II)-system with cubic perovskite structure. Zeitschrift für Naturforschung B. 1978;33:862-5.

29. Mitzi D, Wang S, Feild C, Chess C, Guloy A. Conducting layered organic-inorganic halides containing <110>-oriented perovskite sheets. Science. 1995;267:1473-6.

30. Kagan C, Mitzi D, Dimitrakopoulos C. Organic-inorganic hybrid materials as semiconducting channels in thin-film field-effect transistors. Science. 1999;286:945-7.

31. Frost JM, Butler KT, Walsh A. Molecular ferroelectric contributions to anomalous hysteresis in hybrid perovskite solar cells. *Apl Materials*. 2014;2:081506.
32. Feng HL, Arai M, Matsushita Y, Tsujimoto Y, Guo Y, Sathish CI, Wang X, Yuan Y-H, Tanaka M, Yamaura K. High-temperature ferrimagnetism driven by lattice distortion in double perovskite  $\text{Ca}_2\text{FeOsO}_6$ . *Journal of the American Chemical Society*. 2014;136:3326-9.
33. Aso R, Kan D, Shimakawa Y, Kurata H. Atomic level observation of octahedral distortions at the perovskite oxide heterointerface. *Scientific reports*. 2013;3:2214.
34. Green MA, Ho-Baillie A, Snaith HJ. The emergence of perovskite solar cells. *Nature Photonics*. 2014;8:nphoton. 2014.134.
35. Kim H-S, Lee C-R, Im J-H, Lee K-B, Moehl T, Marchioro A, Moon S-J, Humphry-Baker R, Yum J-H, Moser JE. Lead iodide perovskite sensitized all-solid-state submicron thin film mesoscopic solar cell with efficiency exceeding 9%. *Scientific reports*. 2012;2:591.
36. He Z, Zhong C, Su S, Xu M, Wu H, Cao Y. Enhanced power-conversion efficiency in polymer solar cells using an inverted device structure. *Nature Photonics*. 2012;6:591.
37. Nie W, Tsai H, Asadpour R, Blancon J-C, Neukirch AJ, Gupta G, Crochet JJ, Chhowalla M, Tretiak S, Alam MA. High-efficiency solution-processed perovskite solar cells with millimeter-scale grains. *Science*. 2015;347:522-5.
38. Bai Y, Yu H, Zhu Z, Jiang K, Zhang T, Zhao N, Yang S, Yan H. High performance inverted structure perovskite solar cells based on a PCBM: polystyrene blend electron transport layer. *Journal of Materials Chemistry A*. 2015;3:9098-102.
39. Liu D, Kelly TL. Perovskite solar cells with a planar heterojunction structure prepared using room-temperature solution processing techniques. *Nature Photonics*. 2014;8:133.
40. Chen Q, Zhou H, Hong Z, Luo S, Duan H-S, Wang H-H, Liu Y, Li G, Yang Y. Planar heterojunction perovskite solar cells via vapor-assisted solution process. *Journal of the American Chemical Society*. 2013;136:622-5.
41. Mei A, Li X, Liu L, Ku Z, Liu T, Rong Y, Xu M, Hu M, Chen J, Yang Y. A

hole-conductor-free, fully printable mesoscopic perovskite solar cell with high stability. *Science*. 2014;345:295-8.

42. Park N-G. Organometal perovskite light absorbers toward a 20% efficiency low-cost solid-state mesoscopic solar cell. *The journal of physical chemistry letters*. 2013;4:2423-9.

43. Luo D, Yang W, Wang Z, Sadhanala A, Hu Q, Su R, Shivanna R, Trindade GF, Watts JF, Xu Z. Enhanced photovoltage for inverted planar heterojunction perovskite solar cells. *Science*. 2018;360:1442-6.

44. Burschka J, Pellet N, Moon S-J, Humphry-Baker R, Gao P, Nazeeruddin MK, Grätzel M. Sequential deposition as a route to high-performance perovskite-sensitized solar cells. *Nature*. 2013;499:316.

45. Wang P, Shao Z, Ulfa M, Pauporté T. Insights into the hole blocking layer effect on the perovskite solar cell performance and impedance response. *The Journal of Physical Chemistry C*. 2017;121:9131-41.

46. Shockley W, Queisser HJ. Detailed balance limit of efficiency of p-n junction solar cells. *Journal of Applied Physics*. 1961;32:510-9.

47. Eperon GE, Stranks SD, Menelaou C, Johnston MB, Herz LM, Snaith HJ. Formamidinium lead trihalide: a broadly tunable perovskite for efficient planar heterojunction solar cells. *Energy & Environmental Science*. 2014;7:982-8.

48. Etgar L, Gao P, Xue Z, Peng Q, Chandiran AK, Liu B, Nazeeruddin MK, Grätzel M. Mesoscopic CH<sub>3</sub>NH<sub>3</sub>PbI<sub>3</sub>/TiO<sub>2</sub> heterojunction solar cells. *Journal of the American Chemical Society*. 2012;134:17396-9.

49. Lee MM, Teuscher J, Miyasaka T, Murakami TN, Snaith HJ. Efficient hybrid solar cells based on meso-superstructured organometal halide perovskites. *Science*. 2012:1228604.

50. Yi C, Luo J, Meloni S, Boziki A, Ashari-Astani N, Grätzel C, Zakeeruddin SM, Rühlisberger U, Grätzel M. Entropic stabilization of mixed A-cation ABX<sub>3</sub> metal halide perovskites for high performance perovskite solar cells. *Energy & Environmental Science*. 2016;9:656-62.

51. Ponseca Jr CS, Savenije TJ, Abdellah M, Zheng K, Yartsev A, Pascher Tr,

Harlang T, Chabera P, Pullerits T, Stepanov A. Organometal halide perovskite solar cell materials rationalized: ultrafast charge generation, high and microsecond-long balanced mobilities, and slow recombination. *Journal of the American Chemical Society*. 2014;136:5189-92.

52. Amat A, Mosconi E, Ronca E, Quarti C, Umari P, Nazeeruddin MK, Grätzel M, De Angelis F. Cation-induced band-gap tuning in organohalide perovskites: interplay of spin-orbit coupling and octahedra tilting. *Nano letters*. 2014;14:3608-16.

53. Lee JW, Kim DH, Kim HS, Seo SW, Cho SM, Park NG. Formamidinium and cesium hybridization for photo-and moisture-stable perovskite solar cell. *Advanced Energy Materials*. 2015;5:1501310.

54. Saliba M, Matsui T, Domanski K, Seo J-Y, Ummadisingu A, Zakeeruddin SM, Correa-Baena J-P, Tress WR, Abate A, Hagfeldt A. Incorporation of rubidium cations into perovskite solar cells improves photovoltaic performance. *Science*. 2016;354:206-9.

55. Zhang T, Dar MI, Li G, Xu F, Guo N, Grätzel M, Zhao Y. Bication lead iodide 2D perovskite component to stabilize inorganic  $\alpha$ -CsPbI<sub>3</sub> perovskite phase for high-efficiency solar cells. *Science advances*. 2017;3:e1700841.

56. Stoumpos CC, Malliakas CD, Kanatzidis MG. Semiconducting tin and lead iodide perovskites with organic cations: phase transitions, high mobilities, and near-infrared photoluminescent properties. *Inorganic chemistry*. 2013;52:9019-38.

57. McMeekin DP, Sadoughi G, Rehman W, Eperon GE, Saliba M, Hörantner MT, Haghighirad A, Sakai N, Korte L, Rech B. A mixed-cation lead mixed-halide perovskite absorber for tandem solar cells. *Science*. 2016;351:151-5.

58. Bi D, Yi C, Luo J, Décoppet J-D, Zhang F, Zakeeruddin SM, Li X, Hagfeldt A, Grätzel M. Polymer-templated nucleation and crystal growth of perovskite films for solar cells with efficiency greater than 21%. *Nature Energy*. 2016;1:16142.

59. Bi D, Tress W, Dar MI, Gao P, Luo J, Renevier C, Schenk K, Abate A, Giordano F, Baena J-PC. Efficient luminescent solar cells based on tailored mixed-cation perovskites. *Science advances*. 2016;2:e1501170.

60. Saliba M, Matsui T, Seo J-Y, Domanski K, Correa-Baena J-P, Nazeeruddin MK,

Zakeeruddin SM, Tress W, Abate A, Hagfeldt A. Cesium-containing triple cation perovskite solar cells: improved stability, reproducibility and high efficiency. *Energy & Environmental Science*. 2016;9:1989-97.

61. Bu T, Liu X, Zhou Y, Yi J, Huang X, Luo L, Xiao J, Ku Z, Peng Y, Huang F. A novel quadruple-cation absorber for universal hysteresis elimination for high efficiency and stable perovskite solar cells. *Energy & Environmental Science*. 2017;10:2509-15.

62. Yi C, Li X, Luo J, Zakeeruddin SM, Grätzel M. Perovskite photovoltaics with outstanding performance produced by chemical conversion of bilayer mesostructured lead halide/TiO<sub>2</sub> films. *Advanced Materials*. 2016;28:2964-70.

63. Jeon NJ, Noh JH, Kim YC, Yang WS, Ryu S, Seok SI. Solvent engineering for high-performance inorganic-organic hybrid perovskite solar cells. *Nature materials*. 2014;13:897.

64. Xie FX, Zhang D, Su H, Ren X, Wong KS, Grätzel M, Choy WC. Vacuum-assisted thermal annealing of CH<sub>3</sub>NH<sub>3</sub>PbI<sub>3</sub> for highly stable and efficient perovskite solar cells. *ACS nano*. 2015;9:639-46.

65. Zheng X, Chen B, Wu C, Priya S. Room temperature fabrication of CH<sub>3</sub>NH<sub>3</sub>PbBr<sub>3</sub> by anti-solvent assisted crystallization approach for perovskite solar cells with fast response and small J-V hysteresis. *Nano Energy*. 2015;17:269-78.

66. Wang Y, Wu J, Zhang P, Liu D, Zhang T, Ji L, Gu X, Chen ZD, Li S. Stitching triple cation perovskite by a mixed anti-solvent process for high performance perovskite solar cells. *Nano Energy*. 2017;39:616-25.

67. Paek S, Schouwink P, Athanasopoulou EN, Cho K, Grancini G, Lee Y, Zhang Y, Stellacci F, Nazeeruddin MK, Gao P. From Nano-to Micrometer Scale: The Role of Antisolvent Treatment on High Performance Perovskite Solar Cells. *Chemistry of Materials*. 2017;29:3490-8.

68. Liu M, Johnston MB, Snaith HJ. Efficient planar heterojunction perovskite solar cells by vapour deposition. *Nature*. 2013;501:395.

69. Li X, Bi D, Yi C, Décoppet J-D, Luo J, Zakeeruddin SM, Hagfeldt A, Grätzel M. A vacuum flash-assisted solution process for high-efficiency large-area perovskite

solar cells. *Science*. 2016;aaf8060.

70. Edri E, Kirmayer S, Cahen D, Hodes G. High open-circuit voltage solar cells based on organic–inorganic lead bromide perovskite. *The journal of physical chemistry letters*. 2013;4:897-902.

71. Heo JH, Im SH, Noh JH, Mandal TN, Lim C-S, Chang JA, Lee YH, Kim H-j, Sarkar A, Nazeeruddin MK. Efficient inorganic–organic hybrid heterojunction solar cells containing perovskite compound and polymeric hole conductors. *Nature Photonics*. 2013;7:486.

72. Cai B, Xing Y, Yang Z, Zhang W-H, Qiu J. High performance hybrid solar cells sensitized by organolead halide perovskites. *Energy & Environmental Science*. 2013;6:1480-5.

73. Christians JA, Fung RC, Kamat PV. An inorganic hole conductor for organo-lead halide perovskite solar cells. Improved hole conductivity with copper iodide. *Journal of the American Chemical Society*. 2013;136:758-64.

74. Chavhan S, Miguel O, Grande H-J, Gonzalez-Pedro V, Sánchez RS, Barea EM, Mora-Seró I, Tena-Zaera R. Organo-metal halide perovskite-based solar cells with CuSCN as the inorganic hole selective contact. *Journal of Materials Chemistry A*. 2014;2:12754-60.

75. Leijtens T, Lim J, Teuscher J, Park T, Snaith HJ. Charge Density Dependent Mobility of Organic Hole-Transporters and Mesoporous TiO<sub>2</sub> Determined by Transient Mobility Spectroscopy: Implications to Dye-Sensitized and Organic Solar Cells. *Advanced Materials*. 2013;25:3227-33.

76. Snaith HJ, Grätzel M. Enhanced charge mobility in a molecular hole transporter via addition of redox inactive ionic dopant: Implication to dye-sensitized solar cells. *Applied physics letters*. 2006;89:262114.

77. Jennings JR, Wang Q. Influence of lithium ion concentration on electron injection, transport, and recombination in dye-sensitized solar cells. *The Journal of Physical Chemistry C*. 2009;114:1715-24.

78. Shi Y, Wang X, Zhang H, Li B, Lu H, Ma T, Hao C. Effects of 4-tert-butylpyridine on perovskite formation and performance of solution-processed

- perovskite solar cells. *Journal of Materials Chemistry A*. 2015;3:22191-8.
79. Domanski K, Correa-Baena J-P, Mine N, Nazeeruddin MK, Abate A, Saliba M, Tress W, Hagfeldt A, Grätzel M. Not all that glitters is gold: metal-migration-induced degradation in perovskite solar cells. *ACS nano*. 2016;10:6306-14.
80. Bush KA, Bailie CD, Chen Y, Bowring AR, Wang W, Ma W, Leijtens T, Moghadam F, McGehee MD. Thermal and environmental stability of semi-transparent perovskite solar cells for tandems enabled by a solution-processed nanoparticle buffer layer and sputtered ITO electrode. *Advanced Materials*. 2016;28:3937-43.
81. Hou Y, Du X, Scheiner S, McMeekin DP, Wang Z, Li N, Killian MS, Chen H, Richter M, Levchuk I. A generic interface to reduce the efficiency-stability-cost gap of perovskite solar cells. *Science*. 2017;358:1192-7.
82. Arora N, Dar MI, Hinderhofer A, Pellet N, Schreiber F, Zakeeruddin SM, Grätzel M. Perovskite solar cells with CuSCN hole extraction layers yield stabilized efficiencies greater than 20%. *Science*. 2017:eaam5655.
83. Zhou H, Chen Q, Li G, Luo S, Song T-b, Duan H-S, Hong Z, You J, Liu Y, Yang Y. Interface engineering of highly efficient perovskite solar cells. *Science*. 2014;345:542-6.
84. Xu X, Liu Z, Zuo Z, Zhang M, Zhao Z, Shen Y, Zhou H, Chen Q, Yang Y, Wang M. Hole selective NiO contact for efficient perovskite solar cells with carbon electrode. *Nano letters*. 2015;15:2402-8.

# **Chapter 2. TiO<sub>2</sub> electron transport layer (ETL) Optimization and achievement of high efficiency MAPI perovskite solar cells by two-step deposition method.**

## **2.1 Introduction**

Solar cells based on hybrid organic-inorganic perovskite absorbers have emerged as the most promising photovoltaic devices. They combine high power conversion efficiency, inexpensive starting materials and chemicals and rather simple fabrication procedures.[1-12] These devices have attracted a tremendous and continuously increasing attention from the scientific community and has become a viable competitor to conventional silicon photovoltaic devices. In perovskite solar cells (PSC), hybrid perovskite compounds, typically methylammonium lead iodide (CH<sub>3</sub>NH<sub>3</sub>PbI<sub>3</sub> or MAPbI<sub>3</sub>), which are direct bandgap semiconductors, are used as solar light absorbers to generate excitons.[1,2] The charge extraction and collection are obtained by contacting the perovskite layers with two adjacent phases with appropriate band structures and energy levels.[8-10] The electron transport material (ETM) extracts and transports the photogenerated electrons and blocks the hole transfer. On the other side, the hole transporting material (HTM) layer permits the separation and transport of photogenerated holes whereas the electron transfer is blocked. The characteristics of these adjacent layers are keys for an efficient functioning of the PSCs.

Highly efficient PSCs require the limitation of parasitic recombination reactions, especially at the perovskite/transparent conducting oxide (TCO) thin film interface. An indispensable part of PSC is the thin and compact layer deposited on TCO, simultaneously acting as electron extraction contact and hole blocking layer (BL).[8,14-21] Generally speaking, the BL must be thin, pinhole-free, crack-free, electrically conductive, transparent to the visible and near-infrared light and

conformal covering the TCO layer. The lack of pinholes and cracks in BL is critical to improve the hole blocking capability.  $\text{TiO}_2$  conducting oxide, as a wide bandgap n-type semiconductor, is the most common ETM used as hole BL in PSC due to low cost, high stability and appropriate band structure. Many techniques have been reported in the literature to prepare  $\text{TiO}_2$  BLs such as spray pyrolysis,[18] spin-coating,[14,15] magnetron sputtering,[18,19] atomic layer deposition (ALD),[20] electrochemical deposition [21] and so on. Although some group's PSCs already achieved relative high efficiency, the BL related problems still remain poorly understood. Therefore, we deeply investigated how various  $\text{TiO}_2$  blocking layers affect the performances and functioning of  $\text{MAPbI}_3$  perovskite solar cells. In this chapter, these BLs were prepared by spray pyrolysis and traditional spin-coating technology.

## 2.2 Experiments

The F-doped tin oxide coated glass (TEC7, Pilkington) was cut, and etched patterned using HCl 10% and Zn powder. They were then cleaned by using a concentrated  $2.5 \text{ mol.L}^{-1}$  NaOH solution, rinsed with water, clean with a detergent, rinsed with MilliQ water and dried with compressed air. The substrates were then annealed 30 min at  $500 \text{ }^\circ\text{C}$ .

Four different kinds of blocking layers were investigated. BL-S was prepared by an aerosol spray pyrolysis technology. A precursor solution was prepared by mixing 0.6 mL of titanium isopropoxide, 0.4 mL of acetyl acetone in 7 mL of isopropanol. The substrate was placed on a hotplate at  $455 \text{ }^\circ\text{C}$  for 20 min prior to start the spraying. And then the  $\text{TiO}_2$  deposited layer was annealed at  $455 \text{ }^\circ\text{C}$  for 20 min. Three different precursor solutions were investigated for the preparation of BLs by spin-coating. For BL-H, 0.8 mL of titanium isopropoxide (TTIP) was mixed to 50  $\mu\text{L}$  of HCl 37% in 4 mL of ethanol. For BL-A, 0.45 mL TTIP, 0.15 mL acetic acid in 6mL ethanol.[15] For BL-P, the solution was a mixture of 100  $\mu\text{L}$  titanium diisopropoxide-bis acetylacetonate (same precursor as for BL-S) and 70  $\mu\text{L}$  isopropanol. A 50  $\mu\text{L}$  of these

solutions was deposited on the substrate, spin-coated at 4000 rpm for 35 s and then placed on a hot-plate at 60 °C for 10 min. In all cases, the layers were finally annealed at 500 °C for 30 min. The mesoporous TiO<sub>2</sub> layer was prepared by diluting the NR30-D paste from Dyesol with ethanol (1:10 mass ratio). 50 µL of the solution was deposited on the blocking layer and spin-coated 20 s at 5000 rpm. The layer was then dried on a hotplate at 100 °C for 10 min and subsequently annealed at 500 °C for 30 min.

The CH<sub>3</sub>NH<sub>3</sub>PbI<sub>3</sub> (MAPI) layer was prepared using a 2-step technique. Firstly a 50 µL of a PbI<sub>2</sub> precursor solution consisting of acidified 1 mol.L<sup>-1</sup> PbI<sub>2</sub> in DMF was spin-coated at 4000 rpm for 30 s. Then, 100 µL of a methylammonium (MAI) solution containing 40 mg of MAI in 1 mL of 2-propanol was deposited on the PbI<sub>2</sub> layer, allowed to react for 20 s and spun at 4000 rpm for 30 s. The perovskite layer was annealed at 115 °C for 1h on a hotplate. The samples were then removed from the hotplate and left to cool down to room temperature during 10 min.

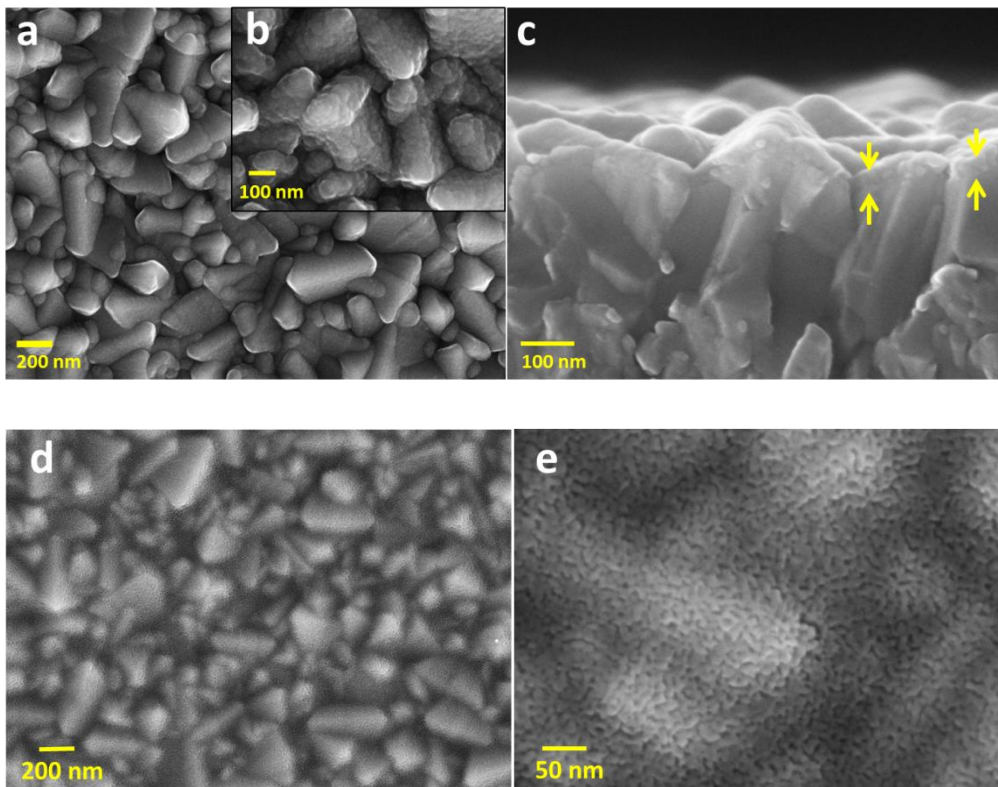
Spiro-OMeTAD was used as the HTM. A solution was prepared by dissolving 72 mg of Spiro-OMeTAD in 1 ml chlorobenzene. Then, 17.5 µl of bis(trifluoromethylsulfonyl)imide lithium salt solution (LiTFSI) solution (520 mg in 1 ml ACN), 28 µL of TBP (tert-butylpyridine) and 6 µL of tris(2-1H-pyrazol-1-yl)-4-tert-butylpyridine-cobalt(III)-tris(bis(trifluoromethylsulfonyl)imide) (300 mg in 1 ml ACN) were added to this solution. A 35 µL of the HTM solution was spin-coated at 4000 rpm for 20 s. Finally, the device was completed by thermally evaporating a 70-80 nm thick gold back contact on the Spiro-OMeTAD layer.

## 2.3 Results and discussion

The TiO<sub>2</sub> blocking layers (BLs) were prepared by two different technologies, spray pyrolysis and spin coating. Two different titanium precursors were employed for spin coating technology, titanium isopropoxide (TTIP) and titanium diisopropoxide-bis acetylacetonate. In here, the precursor solutions were acidified by acetic acid (BL-A)

and by hydrochloric acid (BL-H) using TTIP as titanium resource. Another, titanium diisopropoxide-bis acetylacetonate, was tested for spin-coating and named BL-P below. The blocking layer prepared by spray pyrolysis is named BL-S below.

Field emission scanning electron microscopy (FE-SEM) was employed to characterize the morphologies of optimized BLs. In Figure 2.1, the images of a-c show that BL-S was highly conformal and perfectly covered the FTO grains. Its thickness was measured between 30-35 nm (Figure 1c). No porosity was found and the obtained layer was highly compact. On the other hand, all the spin-coated BLs appeared as made of grains with a small size of about 10 nm (Figure 1d-k). Pinholes were present between the grains. The spin-coated layers were thicker than the sprayed one and had a tendency to smooth the surface. We also noted that the layers prepared with titanium isopropoxide were denser than those prepared with diisopropoxide-bis acetylacetonate precursor. The thicknesses of these layers were measured at 30-50 nm for BL-A, 70-80 nm for BL-H and 80-100 nm for BL-P, the FTO layer thickness was about 550-600 nm.



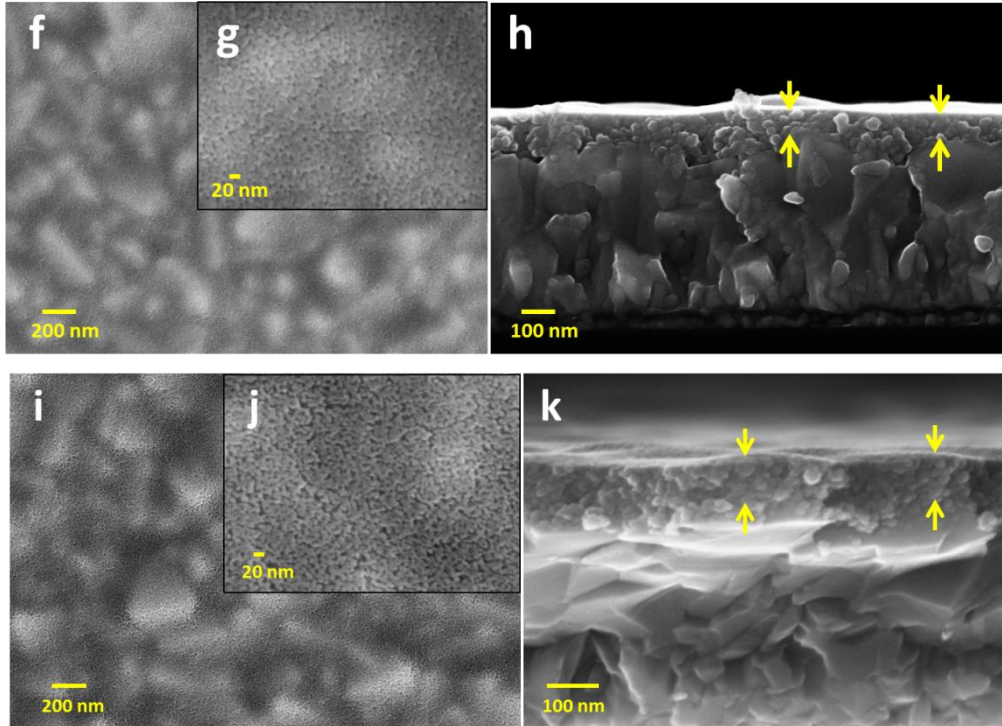


**Figure 2.1** Field emission scanning electron microscopy (SEM) views of blocking layers. (a-c) BL-S prepared by spray-pyrolysis technology; (d-k) prepared by spin coating. (d,e) BL-A; (f-h) BL-H and (i-k) BL-P.

The optical absorbance properties of the layers were measured using the FTO coated glass substrate as the baseline. In Figure 2.2, the curves are plotted as Tauc plots. Assuming that the layers are mainly made of  $\text{TiO}_2$  anatase phase which has an indirect bandgap, the optical bandgap are determined at 3.25 eV for the sprayed layer (BL-S). We found 3.30 eV for BL-A and 3.34 eV for BL-H and BL-P, respectively. These values are in agreement with the formation of a thin  $\text{TiO}_2$  layer of anatase.[25] However, the edge and linear section of the Tauc plots are reduced because the prepared layers are very thin. For accurately determine the crystal phase, Raman spectroscopy measurements were implemented.

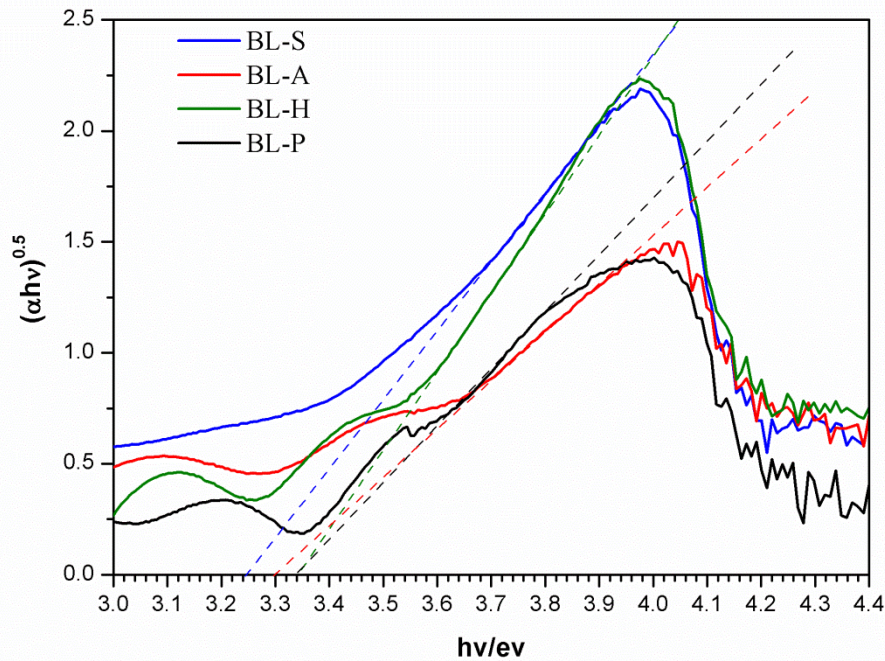


**Figure 2.2** Ultraviolet-Visible (UV-Vis) absorption spectra of various TiO<sub>2</sub> blocking layers, displayed as Tauc plots.

The Raman spectroscopy is sensitive to the TiO<sub>2</sub> crystallographic polymorphism. It is known that the electrical conductivity of TiO<sub>2</sub> rutile and brookite phase is less than that of the anatase one.[25] To reduce the series resistance, the formation of the TiO<sub>2</sub> anatase phase is then preferable in perovskite solar cells. Raman scattering was employed to determine the phase and qualitatively investigate the crystallinity of the BL. The Raman spectra of the BLs are shown in Figure 2.3. Anatase phase of TiO<sub>2</sub> has a tetragonal structure and belongs to the space group  $D_{4h}^{19}$  (I4/amd). The primitive unit cell contains two TiO<sub>2</sub> chemical units.[23] According to the factor group analysis, 15 optical modes have the irreducible representation and six modes are Raman active:  $A_{1g} + 2B_{1g} + 3E_g$ . [22] BL-S shows the best defined emission bands which are indexed to anatase at 144 cm<sup>-1</sup> (E<sub>g</sub>), 197 cm<sup>-1</sup> (E<sub>g</sub>), 399 cm<sup>-1</sup> (B<sub>1g</sub>), 513 cm<sup>-1</sup> (A<sub>1g</sub>, B<sub>1g</sub>) and 639 cm<sup>-1</sup> (E<sub>g</sub>). [27] These bands are also observed for the spin-coated layers but are less intense. The intensity order is BL-P, BL-H and BL-A. The emission intensity varies in

the inverse way compared to the layer thickness. Indeed, it increases with the longer range order, the crystallinity and density of the prepared compounds.

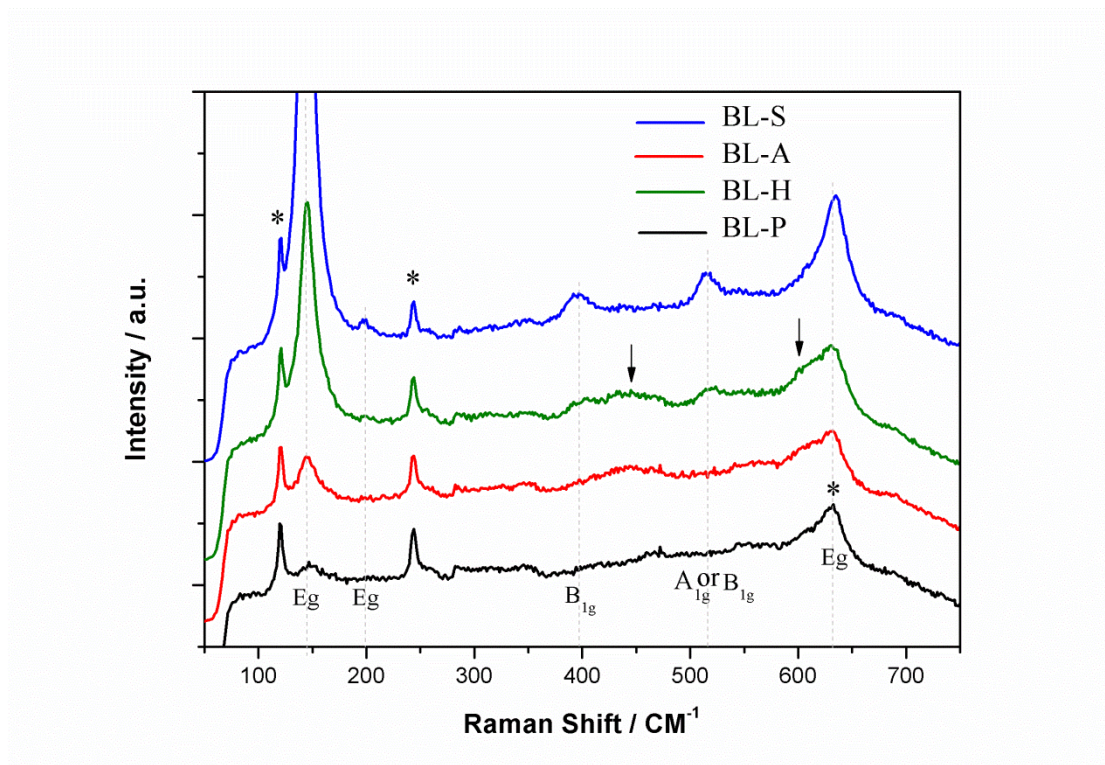


**Figure 2.3** Raman spectra of the various prepared TiO<sub>2</sub> blocking layers on FTO/Glass by the different precursor solution and deposited technologies.

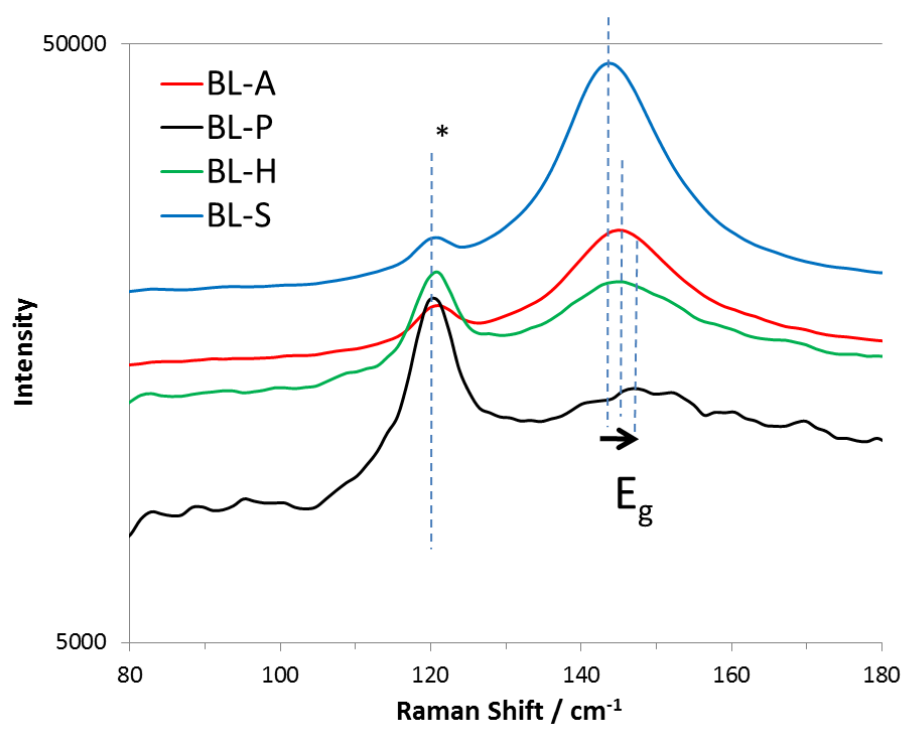


**Figure 2.4** Raman spectra zoom view at the first  $E_g$  mode for the various prepared  $TiO_2$  blocking layers.

Figure 2.4 is a zoom view of the lowest-frequency  $E_g$  Raman mode. This strongest Raman mode arises from the external vibration of the anatase structure. It exhibits a blue shift of the emission band from BL-S to BL-P which is due to phonon confinement and non-stoichiometry effects.[24] It confirms thus a crystallinity increasing as follows: BL-P<BL-H<BL-A<BL-S. A close inspection of Figure 2.3 shows a bump at about  $440\text{ cm}^{-1}$  and a shoulder at  $610\text{ cm}^{-1}$  (marked by arrows) for the layers prepared by spin coating. These peaks correspond to the  $E_g$  and  $A_{1g}$  modes of rutile phase. It indicates the presence of rutile phase in the spin-coated BLs. The Raman characterization shows that the sprayed BL is very well-crystallized and made of the pure anatase phase. A strong Raman emission is observed even if its thickness is the smallest at 30-35 nm. We also note that the indirect bandgap,  $E_g^i$  values determined above are larger for the less-crystallized materials. The reduced quality of the spin-coated films can be assigned to the crystallization process of  $TiO_2$ . These layers are prepared at low temperature, dried and subsequently crystallized at high temperature. It results in the formation of voids and pinholes (evident from SEM views, Figure 2.1), in a reduced crystal size and in the presence of rutile phase. On the other hand the sprayed layers are directly produced and crystallized at high temperature. They are better covering without pinholes and they have a better crystallinity.

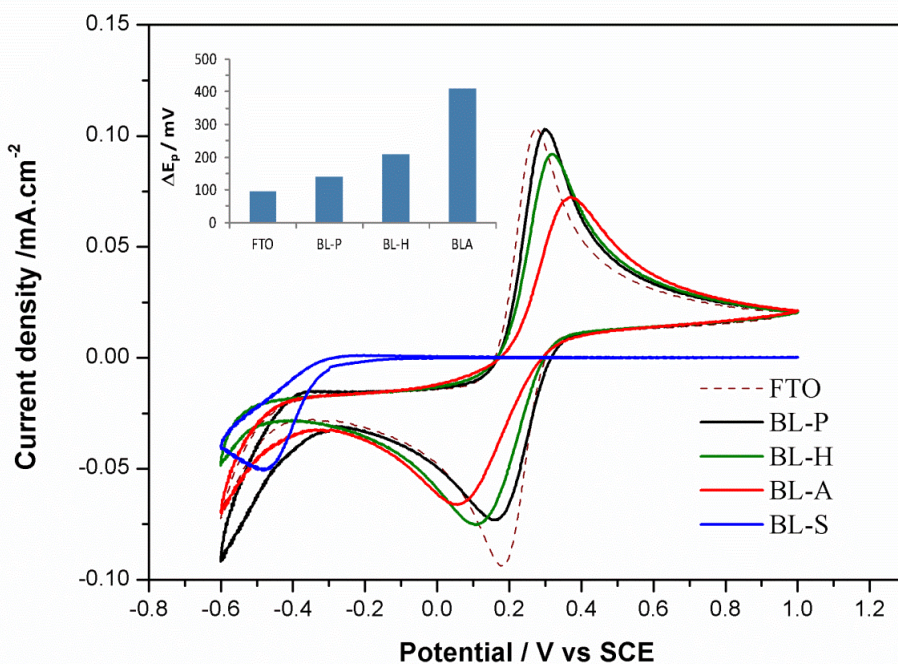


**Figure 2.5** Cyclic voltammograms of FTO electrode (dashed line) and BL electrodes (full lines) in an aqueous solution containing the  $\text{Fe}(\text{CN})_6^{3-/4-}$  redox system. Scan rate  $50 \text{ mV}\cdot\text{s}^{-1}$ . The inset is the  $\Delta E_p$  curve parameter for FTO and the spin-coated  $\text{TiO}_2$  layers.

The prepared BLs were probed using a liquid contact and the cyclic voltametry (CV) technique. We use  $\text{Fe}(\text{CN})_6^{3-/4-}$  as a model of reversible redox system.[21] A supporting electrolyte was employed to ensure a high conductivity of the solution. Kinetics of this redox reaction were measured on the various BLs and compared to bare FTO electrode. The voltammograms are presented in Figure 2.5. For FTO, two close anodic and cathodic peaks were observed. The sharp shape showed a Nernstian behavior. The anodic and cathodic peaks were separated by a potential difference,  $\Delta E_p$ , of 97 mV. A clear effect of the blocking  $\text{TiO}_2$  layer on the current density of the peaks and on  $\Delta E_p$  was observed in Figure 2.5. For the spin-coated layers, the shape varied from a reversible to a semi-reversible behavior.  $\Delta E_p$  increased with the order BL-P, BL-H and BL-A (Figure 2.5 inset). Another interesting parameter is the cathodic peak intensity ratio between the BL and the FTO curves, noted  $I_{p(\text{BL})}/I_{p(\text{FTO})}$  and represented

in Table 2.1. The inverse order was found.

**Table 2.1** Analysis of the CV curves redox peaks in figure 2.5.  $E_p$  is the potential difference between the anodic and cathodic peak maxima. Intensity ratio between the cathodic peak of FTO and of BLs.

	<b>FTO</b>	<b>BL-P</b>	<b>BL-H</b>	<b>BL-A</b>	<b>BL-S</b>
$\Delta E_p / \text{mV}$	97	139	208	411	$\infty$
$I_{p(\text{BL})}/I_{p(\text{FTO})}$	-	0.78	0.80	0.70	0

In Figure 2.5, we have also plotted the CV curve for the BL-S layer. In this case the redox reaction did not occur which indicates that the electrode was well-blocking.  $\Delta E_p$  is a straightforward signature of the blocking capability for spray layer (BL-S), it implied that the blocking capability of the BL is better. In the case of the spin-coating process, the layers present defects and pinholes which are filled by the electrolytic solution. They are somehow porous and the solution can reach the FTO substrate. The closer the CV curves to the FTO electrochemical response, the higher the porosity and the defect density in the layer. From this study we can predict that spray pyrolysis produces the best BL and that the BL-A spin-coated layers will be more efficient than the BL-H and the BL-P ones.

A mesoporous  $\text{TiO}_2$  layer was prepared by spin-coating on BLs and annealed before to be used as a substrate for the preparation MAPI perovskite by a two-step technique. SEM images of the mesoporous layer are shown in Figure 2.6. Its thickness was in the 100-125 nm range. The structure was very open and thin enough to give rise to an opto-electrical response mainly governed by the BL component. The morphology of the  $\text{PbI}_2$  layer prepared by spin coating is shown in Figure 2.7 a. The layer was made of merged grains and presented some voids. After reaction with the MAI, the morphology changed, showing some dissolution and re-crystallization phenomena of the layer which became perfectly covering and was made of large grains (Figure 2.7

b).

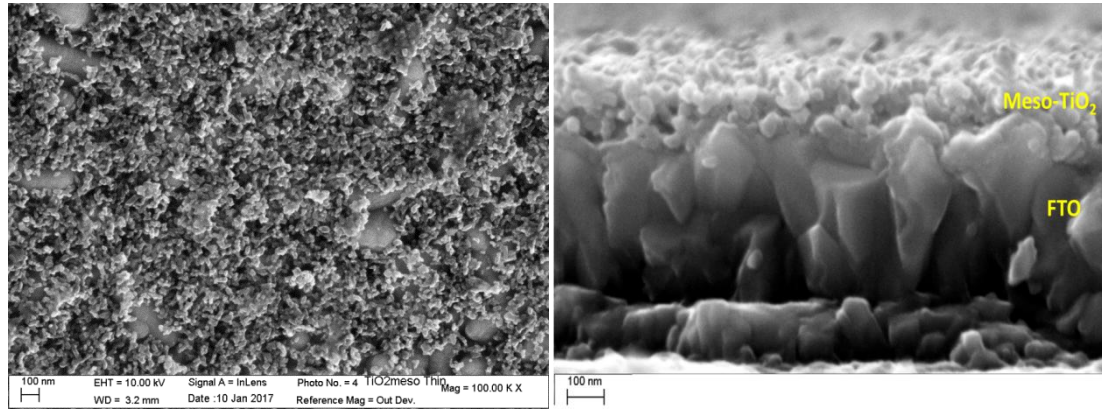


**Figure 2.6** SEM views of the mesoporous TiO<sub>2</sub> layer, deposited on the BL-S/FTO substrate. The left image is a top view, and the right image is a cross-sectional view.

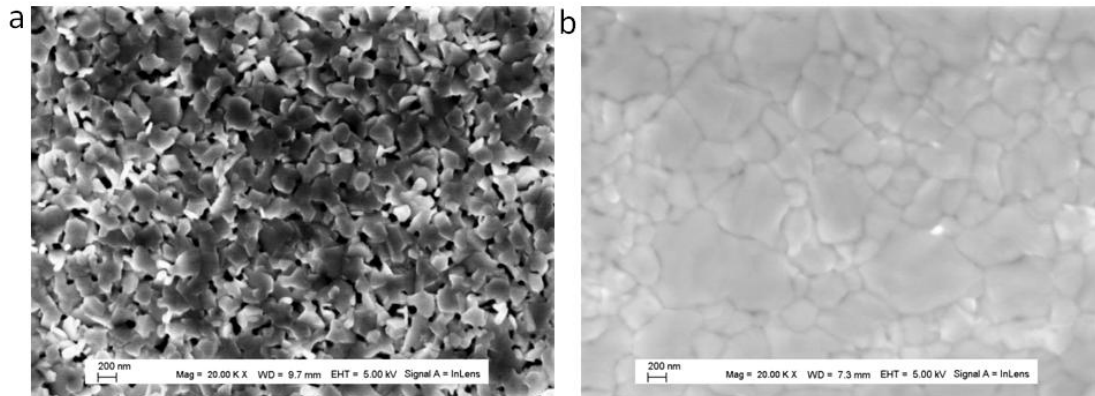


**Figure 2.7** Top view SEM images. (a) The initial deposited PbI<sub>2</sub> layer. (b) The same layer after its reaction with MAI and its transformation into MAPbI<sub>3</sub> layer.

XRD measurements were conducted to evaluate that the prepared compound was the intended perovskite material. A representative pattern is shown in Figure 2.8a. The diffraction peak positions are in agreement with the formation of tetragonal MAPbI<sub>3</sub>. The presence of unreacted hexagonal PbI<sub>2</sub> is also detected with the (001) and (002) PbI<sub>2</sub> phase diffraction peaks at 12.7° and 25.5°, respectively. The formation of MAPbI<sub>3</sub> was also confirmed by optical measurements shown in Figure 2.8b. Typical absorption curves are observed for both perovskite layers deposited on glass and on TiO<sub>2</sub> BL which exhibit an absorption edge measured at 780 nm in agreement with the literature data.[6] The photoluminescence emission of these layers are displayed in the

same figure. They are characterized by an unique emission peak centered at 770 nm.

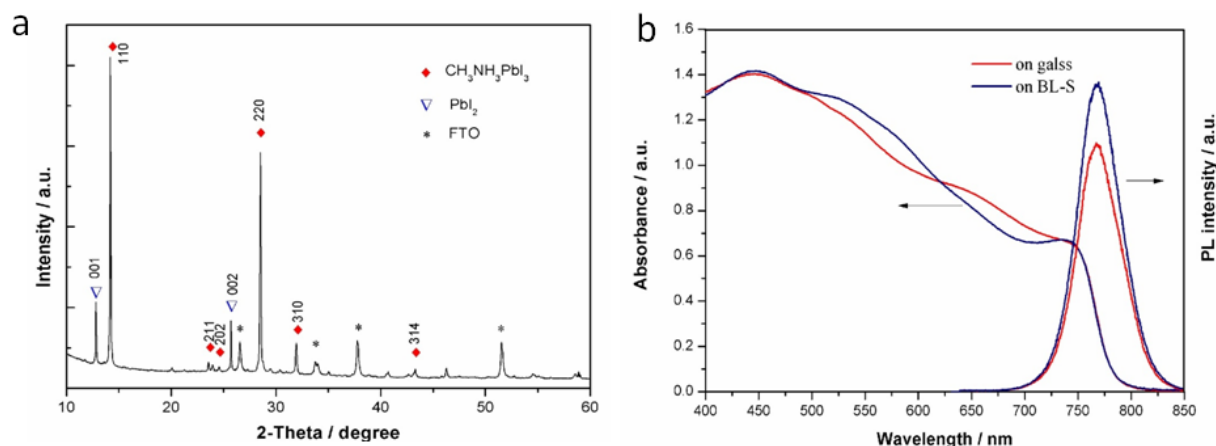


**Figure 2.8** (a) XRD pattern of two-step MAPbI<sub>3</sub> perovskite layer. (b) Absorbance and photoluminescence spectra of two-step MAPbI<sub>3</sub> on glass (red curves) and on BL-S (dark blue curves).

The PSCs were completed by depositing a spin-coated Spiro-OMeTAD layer as hole transporting layer (HTL) and by thermal evaporating a thin gold back contact. A strong effect of the BL deposition technology and precursor solution composition used for BL preparation was found on the *J-V* curves and PSCs performances. Figure 2.9 displays *J-V* curves for good cells measured in the reverse bias scan direction. Table 2.2 gathers the averaged and best device parameters for both the forward and reverse bias scanning directions. We can note that tests were also conducted using modified TiO<sub>2</sub> spraying conditions giving a BL with a thickness of 20-25 nm but they gave rise to lower performances. Optimized BL prepared by spray pyrolysis enabled an efficiency above 17%. Using the spin-coated BL gave rise to lower performances with worse characteristics for the  $V_{oc}$ ,  $J_{sc}$  and FF parameters. Increasing the thickness of BL reduces the FF notably because of the increase of the contact resistance. The average efficiency of the cells with spin-coated BL decreased in the following order: BL-A, BL-H, BL-P. The poor performance of the BL-P cells is assigned to their poor crystallinity, to their porosity and to the fact that this BL was the thickest of the investigated ones. This thickness was required to obtain working and stable cells.

However, it resulted in poorly efficient devices with a large hysteresis. These cells also delivered the lowest  $J_{sc}$ . It suggests a problem of charge injection from the perovskite. On the whole, we note that larger hysteresis is produced by using the spin-coated BLs compared to the sprayed one.

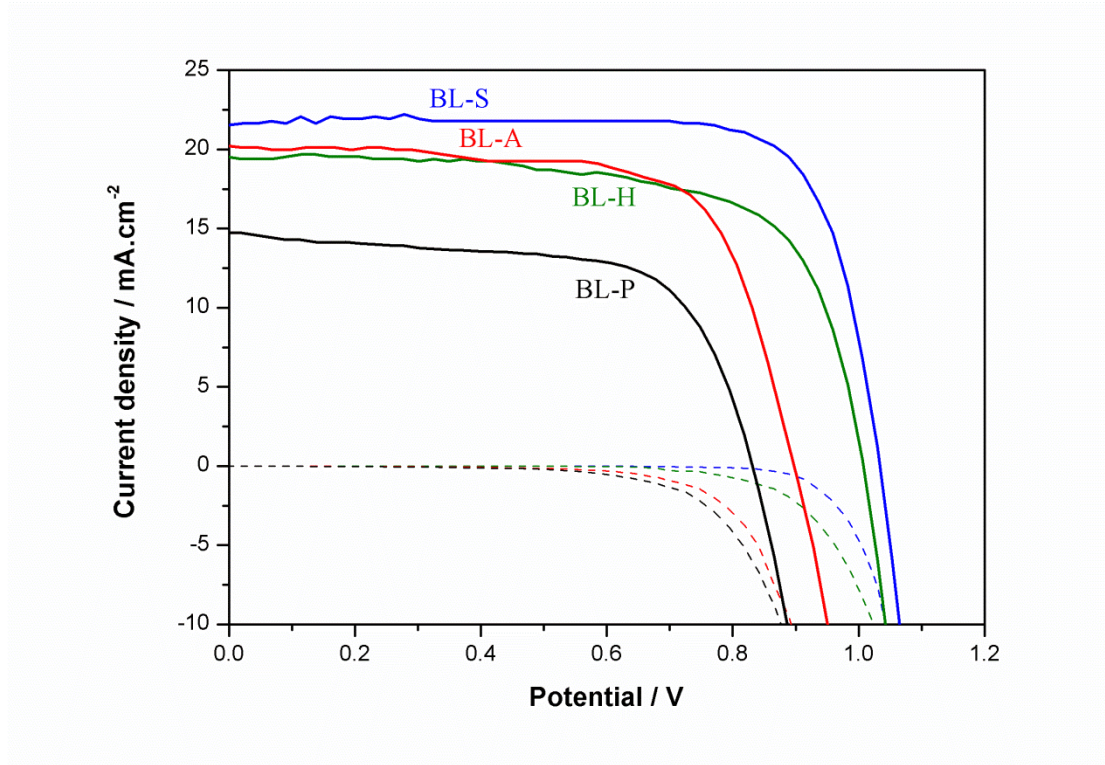


**Figure 2.9** Typical  $J$ - $V$  curves of  $\text{MAPbI}_3$  perovskite solar cells prepared on various BLs. The solid lines are the photocurrent measured under AM1.5 filtered one sun illumination; the dashed lines are the dark current.

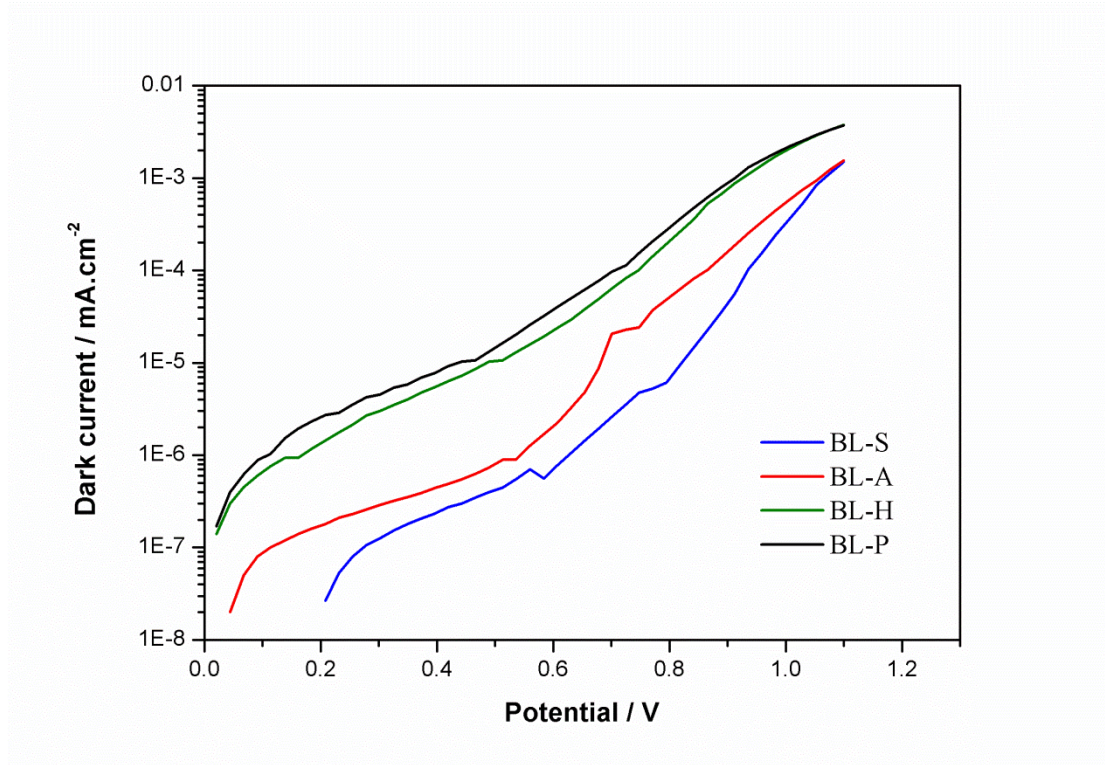
**Table 2.2** Photovoltaic parameters of *J-V* curves of two-step MAPbI<sub>3</sub> PSCs for various BL (AM1.5G filtered 100 mW.cm<sup>-2</sup> illumination).

Blocking layer	sample	Scan direction	V <sub>oc</sub> / V	J <sub>sc</sub> / mA.cm <sup>-2</sup>	FF / %	PCE / %
BL-S	Avg <sup>a</sup>	R <sup>c</sup>	1.006(±0.014)	21.54 (±0.33)	75.16 (±5.45)	16.03 (±0.97)
		F <sup>d</sup>	0.996(±0.022)	22.60 (±1.03)	60.54 (±3.51)	13.63 (±1.00)
	Best <sup>b</sup>	R	1.032	21.66	85.66	17.49
		F	1.021	22.91	61.85	14.47
BL-A	Avg	R	0.967(±0.023)	18.09(±1.26)	72.78 (±3.63)	12.91 (±0.32)
		F	0.877(±0.055)	18.95 (±0.80)	48.45 (±6.67)	8.17 (±1.71)
	Best	R	1.006	19.47	68.09	13.34
		F	0.939	19.30	52.61	9.54
BL-H	Avg	R	0.923 (±0.028)	19.04 (±2.43)	66.54 (±5.93)	11.67 (±1.37)
		F	0.806 (±0.040)	19.02 (±2.00)	43.15 (±8.87)	6.73 (±1.90)
	Best	R	0.967	20.37	66.61	13.12
		F	0.837	20.16	47.98	8.10
BL-P	Avg	R	0.861 (±0.036)	14.17(±0.99)	65.21 (±5.29)	7.92 (±0.21)
		F	0.793 (±0.089)	13.91 (±1.02)	37.78 (±8.62)	4.34 (±1.27)
	Best	R	0.895	12.78	70.43	8.06
		F	0.915	12.44	42.61	4.85

<sup>a</sup>Averaged value. <sup>b</sup> Maximum PCE cell parameters. <sup>c</sup> Reverse scan direction. <sup>d</sup> Forward scan direction.

The BL has a great influence on the V<sub>oc</sub> parameter. The sprayed layer enables the best cell V<sub>oc</sub>. This parameter decreased as follows: BL-S>BL-A>BL-H>BL-P. This is in

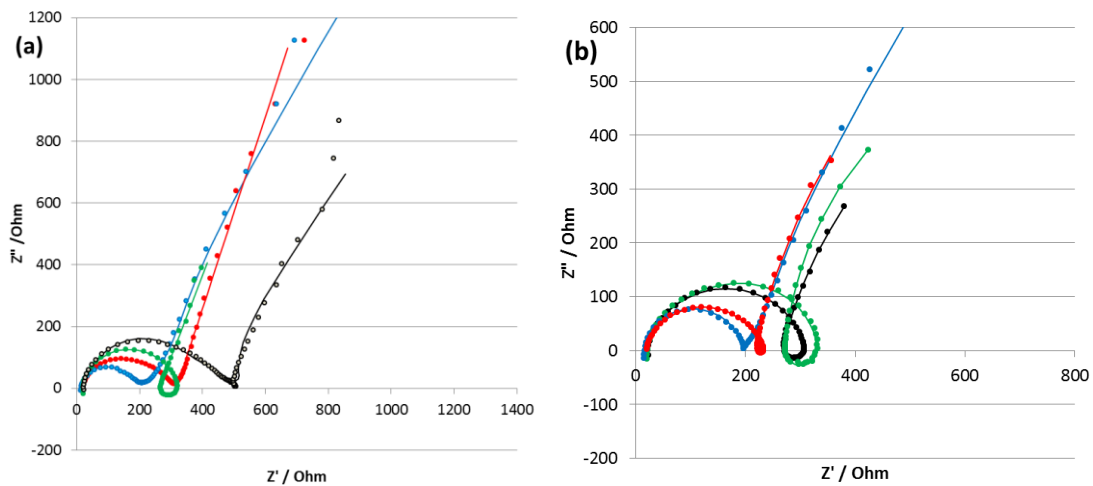
agreement with the cell dark current curves reported in Figure 2.10 . The dark current can vary by up to one and a half orders of magnitude due to the blocking layer characteristics. As expected the lowest dark current is found for the sprayed  $\text{TiO}_2$  that we have observed to be dense and to conformally well-cover the FTO substrate.



**Figure 2.10** Dark current of two-step  $\text{MAPbI}_3$  perovskite solar cells prepared on various BLs. The dark current is plotted in a logarithmic scale.

To gain a deeper insight into the effect of the blocking layers in the cell functioning, we have investigated the solar cell electrical response to a small alternating current (AC) perturbation applied to the devices polarized at various potentials. Impedance spectroscopy has proved to be a useful tool to investigate different solar cells, especially dye-sensitized solar cells [26,28-31] and emerges as a powerful technique for the investigation of PSCs.[8,9,32-45] By this technique the phenomena of charges (ions and electrons/holes) transfer and accumulation can be thoroughly investigated. The cells have been analyzed under light illumination and over a wide frequency range. Figure 2.11 shows Nyquist plots (imaginary versus real part of the impedance) recorded at various applied potentials. In Figure 2.11(a) and 2.11(b) are displayed the

impedance spectra of PSCs on various BLs at short circuit (0.0V) (Figure 2.11a) potential and at 0.6V applied potential (Figure 2.11b): Blue impedance spectrum is BL-S; Red, BL-A; Green, BL-H and Black, BL-P; respectively. For all of them a minimum of three distinct impedance features were found. All the recorded spectra exhibited an arc of circle at low frequencies (LF) and at high frequencies (HF). The behavior of impedance was more complex in the intermediate frequency (IF) range (typically between 1Hz and 2000 Hz). For the BL-H and BL-P cells an inductive loop was observed at IF for all the investigated applied potentials. For the BL-A cells, this feature appeared above 0.4V. For the best cells, with a BL prepared by spray pyrolysis (BL-S), this feature appeared clearly over a narrow applied voltage range, between 0.5-0.7V and it was reduced in amplitude. Figure 2.11(c) is a zoom view of the loop for the BL-S cell polarized at 0.6V. We have also observed an effect of the applied potential on the loop amplitude. Figure 2.11(d) illustrates that the amplitude of the inductive loop increased with the applied voltage, reaching a maximum at 0.6-0.7 V before to decrease.



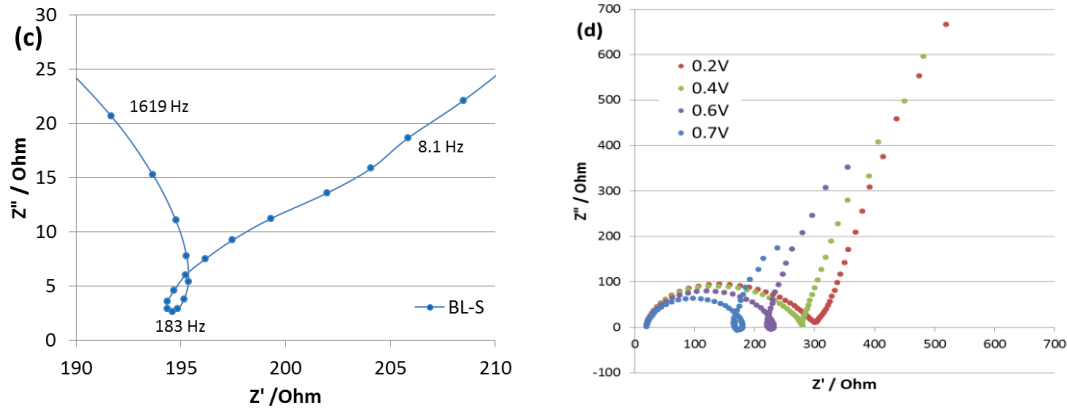


**Figure 2.11** Perovskite solar cells impedance spectra in a Nyquist plot. (a) Spectra at short circuit (0.0V) for various BLs. (b) The same with an applied voltage of 0.6V. (c) Zoom for BL-S at 0.6 V. The dots are the experimental points and full lines are the fits. Blue curve, BL-S; Red, BL-A; Green, BL-H; and Black, BL-P. (d) Effect of applied potential on the impedance response of the BL-A cell.

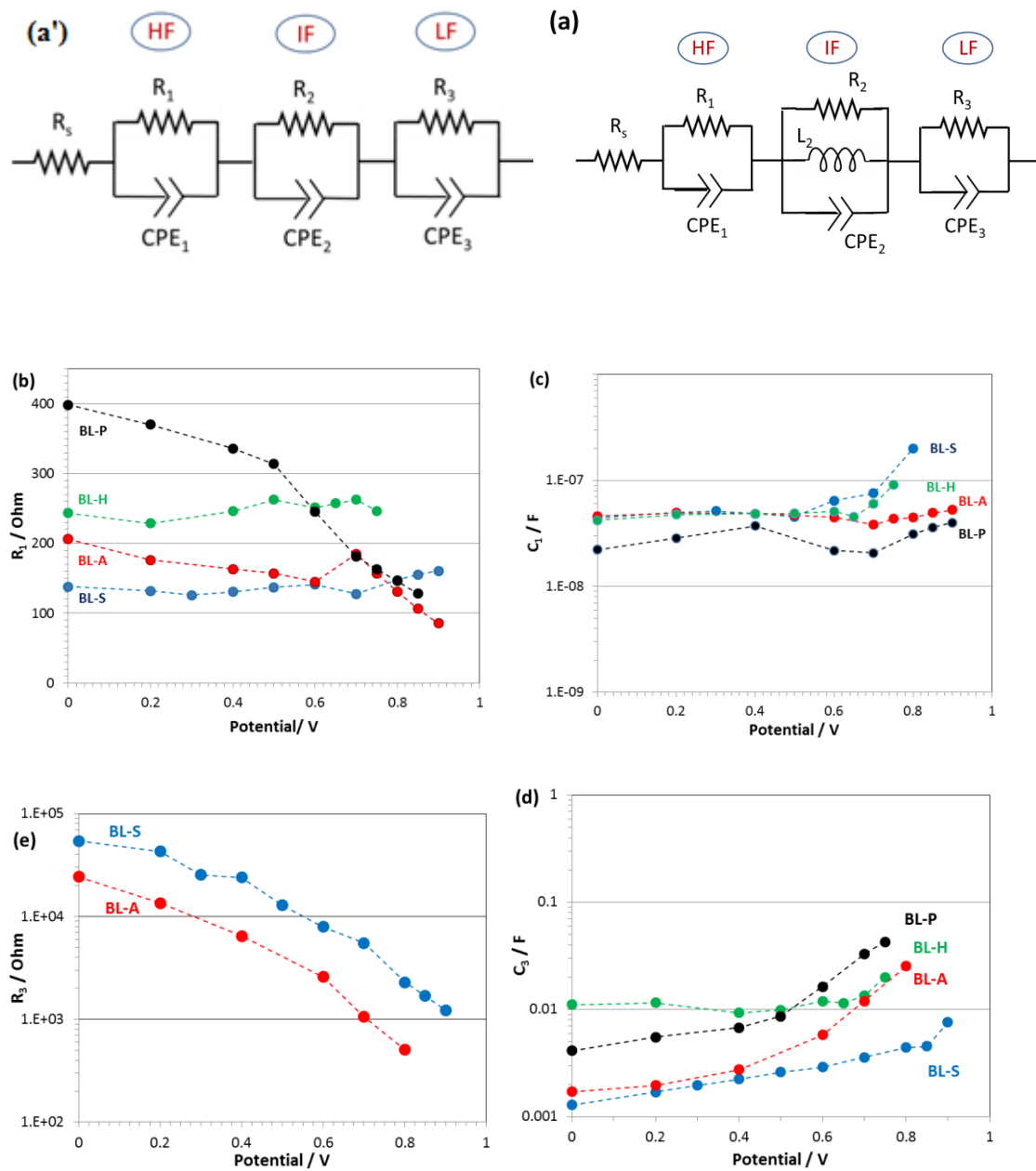
The low and high frequency components of the spectra could be fitted by a resistance a parallel with a capacitance (R//C) circuit. More precisely, because the arc of circles were not a semi-circles and that some dispersion occurred, they were modelled by a R//CPE circuit.  $Z_{CPE}$  is a constant phase element which complex impedance varies like  $Z_{CPE} = \frac{1}{T(i\omega)^p}$  where  $\omega$  is the angular frequency related to the frequency as  $f = \frac{\omega}{2\pi}$ ,  $i$  is the square root of -1 and  $p$  is a number lower than 1. The capacitances were extracted from the  $Z_{CPE}$  parameters using the general approach described by Brug et al.[46] The intermediate region showed various shapes at low applied potential. The loop found for BL-H and BL-P has been modelled using an inductor element in parallel with a resistor and a CPE. A similar modeling has been employed for BL-A above 0.2V and for BL-S above 0.5 V. The other spectra, for which the loop was not found, were fitted with the simplified circuit shown in Figure 2.12 (a'). Quantitative analysis of the electrical response has been achieved using the equivalent electrical circuit (EEC) proposed in the Figure 2.12(a). All the spectra could be correctly fitted with this EEC.

The next step was to study the effect of the BL on the various elements of the EEC and to determine which of them are impacted by this cell component. At short circuit, the size of the arc of circle at high frequency defines a resistance that more or less increases with the BL layer thickness. Using the EEC model, the high frequency resistance, named  $R_1$ , was determined and is presented in Figure 2.12(b) as a function of the applied potential. In the case of BL-S, this resistance is low and more or less constant with the applied potential. Higher values are found with the spin-coated BLs and between 0 and 0.6V, it reflects the thickness and crystallinity of the BLs. This high frequency resistance has been described to scale with the thickness of the perovskite layer above 500  $\mu\text{m}$ . [34] However, in the present case the contribution of the bulk perovskite resistance is very low and  $R_1$  reflects mainly the selective contact resistance. It varies with the transport resistance in the ETL, it reflects then not only its thickness but also its crystallinity and phase composition since it is known that the resistivity of rutile, present in the spin-coated layers, is higher than the anatase one.

The high frequency capacitance is named  $C_1$ . According to the literature data, this capacitance can be assigned to the bulk perovskite layer. [38-40] This is in agreement with the same order of magnitude found for the investigated cells in Figure 2.12(c).  $C_1$  does not vary clearly with the BL layer chemical nature and thickness. The high frequency capacitance has been described as insensitive to light and reflects the dielectric relaxation of the hybrid perovskite. It is due to diverse phenomena involving dipolar mechanisms such as  $\text{CH}_3\text{NH}_3^+$  or  $[\text{PbI}_6]$  octahedra reorientation and cooperative off-centering. [38] In the literature, the dielectric constant of MAPI has been reported with values ranging between 22 and 37. [34,39,40]

The LF relaxation is characterized by a capacitance named  $C_3$ . The low frequency capacitive behavior of PSCs has been described as highly dependent on the illumination. [41] In the dark, the low frequency capacitance is due to electrode polarization taking place due to ion migration to the electrode contacts and charge compensation at the selective contact electrodes giving rise to a double layer component at each contact. Under illumination  $C_3$  becomes very high and has been qualified as a giant capacitance. [43-45] This is caused by the ionic and electronic

charge accumulation at the perovskite/contact layers interfaces. In our case  $C_3$  could be correctly determined for the BL-S cells in which the influence of the IF contribution on the impedance response was low. On the other hand, for BL-H and BL-P, for which IF and LF responses intertwine, the full determination of  $C_3$  could not be done satisfactorily.  $C_3$  for BL-S is constant. Similar  $C_3$  were found for BL-A below 0.5V for which this parameter is not influenced by the IF contribution. Higher  $C_3$  are found for BL-H and BL-P due to the IF contribution overlap and possible higher roughness of the ETL/perovskite interface.



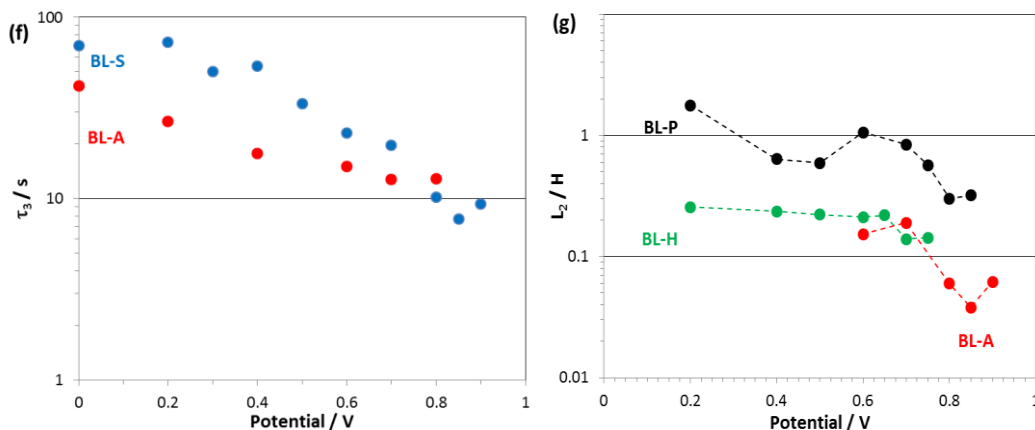


**Figure 2.12** Simplified (a') and general (a) equivalent electrical circuit used to fit the impedance spectra (HF, high frequency; IF, intermediate frequency; and LF, low frequency). Fitting results of the electrical parameters plotted as the function of the applied potential: (b)  $R_1$ , (c)  $C_1$ , (d)  $C_3$ , (e)  $R_3$ , (f)  $\tau_3$  and (g)  $L_2$ .

$R_3$  is the resistance of the low frequency relaxation. This component could be accurately determined for BL-S and BL-A in Figure 2.12(e). The values were higher by a factor 3 in the case of BL-S. The low frequency resistance is assigned to the charge recombination. MAPbI<sub>3</sub> is an ionic conductor and perturbation of the voltage induces the movement of ions and corresponding changes in the potential distribution across the layer and at the interfaces. These changes affect the recombination rate. Higher values for BL-S show lower recombination and are in agreement with the higher  $V_{oc}$  of these cells (see Table 2.2). The  $R_3$  decrease with the applied voltage shows that the recombination is strongly enhanced by the applied voltage. Figure 2.12 (f) shows the relaxation time  $\tau_3=R_3C_3$ . This time constant is low, in the tens of second range and shows the occurrence of a slow process. This is in agreement with the low diffusion coefficient of the ionic species (the most likely candidate being iodide vacancies) in the hybrid perovskite.

The complex behavior in the IF range involves a capacitive, a resistive and an inductive contributions. The loop behavior is much more pronounced in the case of the spin coated layers, especially for those with the worse efficiency, BL-H and BL-P.

In our study, this inductive behavior is the signature of the poorly working cells. The loop could be related to the porosity and the low crystallinity of the spin-coated layers. In these layers, additional electronic surface states would be present.  $C_2$  and  $L_2$  have been determined for the spin coated BL cells. Figure 2.12 (g) shows that the cells with BLs prepared from titanium isopropoxide exhibit similar  $L_2$  behavior and are different to that prepared with diisopropoxide-bis acetylacetonate. The latter yields to lower  $C_2$  in Figure 2.13, but to higher  $L_2$  values. The inductive phenomenon at IF is a singular behavior for a solar cell. It could be linked to the ionic conductivity of the perovskite.[47,48] In Table 2.2, it has been observed that fill factor (FF) parameters of cells decreased as follows: BL-S>BL-A>BL-H>BL-P.  $R_1$  and  $R_2$  contribute to the total series resistance. We have observed that these electrical components vary in the order BL-S<BL-A<BL-H<BL-P (Figure 2.12) and explain the observed behavior for the FF parameter. The BL thickness and resistivity thus significantly affect the FF of the photovoltaic devices.

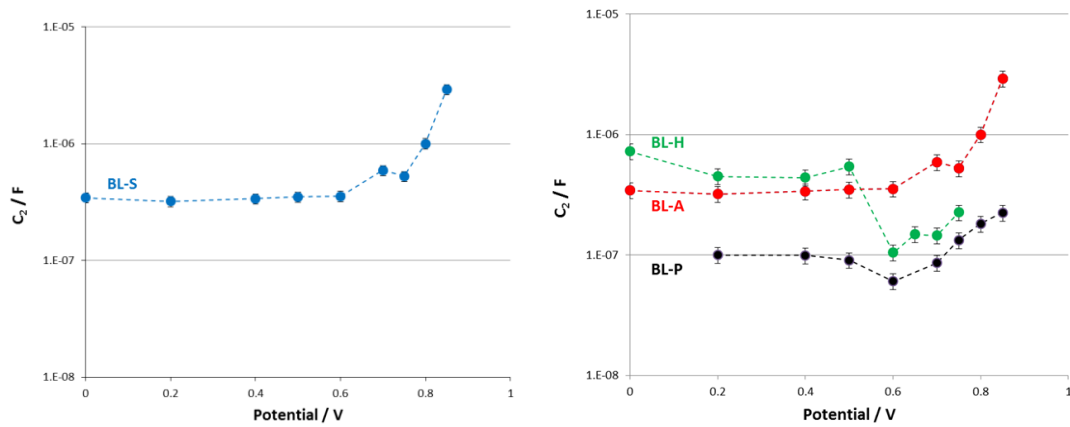


**Figure 2.13** Variation of the  $C_2$  parameter with the applied potential.

## 2.4 Conclusion

We have investigated the key parameters that render  $TiO_2$  blocking layer efficient in perovskite solar cells. Several BLs have been prepared using the aerosol spray pyrolysis and the spin-coating techniques. For the latter, several solution compositions have been investigated. It resulted in the formation of BLs with various properties.

SEM imaging of BLs showed that the spin-coated ones were porous. We have shown that Raman spectroscopy is a reliable and accurate technique which provides essential information on the crystal phase and crystallinity of the prepared layers. Cyclic voltammetry gave fast and reliable information on the blocking ability of the layers used in PSC. Overall, we found that the sprayed BLs were thin, highly compact, covering and conformal. No cracks and pinholes were found due to the precursor degradation and condensation occurring directly at high temperature. They were made of the pure anatase phase and were perfectly blocking. On the other hand the spin-coated layers were porous, contained cracks and pinholes and were not fully blocking. They were less crystallized than the sprayed layers and their crystallinity and blocking capabilities were shown to decrease with the order: BL-A, BL-H and BL-P. Moreover, trace of the rutile phase (less conducting than the anatase one) was also detected for the spin-coated layers. In good agreement with these observations, the best cell efficiencies were achieved using the BL-S.

We developed the use of the impedance spectroscopy technique to investigate the various processes taking place in the cells under illumination and how they are influenced by the BL. The impedance spectra revealed complex electrical phenomena which were characterized by different characteristic times. A general equivalent circuit has been proposed to fit the spectra. In the intermediate frequency range, an inductor was introduced to fit a loop. We have found that the inductive loop, if observable for all the cells, was more pronounced and found over a larger potential range in the case of the most badly working devices. Much information could be extracted from the impedance study. The BL has a strong influence on the high frequency resistance. It varies with the transport resistance of the contact and it reflects the crystallinity, the phase composition and the thickness of the BLs. The high frequency capacitance reflects the dielectric relaxation of the perovskite layer. The low frequency capacitance was extracted for the best working cells and was assigned to the ionic and electronic charge accumulation at the interfaces. The low frequency resistance is related to the recombination rate in the cells and was much higher for the the BL-S cells giving rise to higher cell performances. The low frequency relaxation

time is high, in the tens of seconds range, and can be related to slow relaxation processes occurring in the cells such as the movement of ionic species.

Our study has clearly shown the strong influence of the BL on the cell functioning, performances and impedance response. BLs produced directly at high temperature such as the BL-S ones have much better properties that render them more efficient for the electron transport and hole blocking and they produced high efficiency perovskite solar cells. This optimized BL will be implemented in Chapter 3 and Chapter 4 for the development of highly efficient PSCs using mixed cation hybrid perovskite.

## References

- [1] Kim, H.S.; Lee, C.R.; Im J.H.; Lee, K.H.; Moehl, T.; Marchioro, A.; Moon, S.J.; Humphry-Baker, R.; Yum, J.H.; Moser, J.E. et al., M. Lead iodide perovskite sensitized all-solid-state submicron thin film mesoscopic solar cell with efficiency exceeding 9%. *Sci. Rep.* **2012**, *2*, 591.
- [2] Lee, M.M.; Teuscher, J.; Miyasaka, T.; Murakami, T.N.; Snaith, H.J. Efficient hybrid solar cells based on meso-superstructured organo-metal halide perovskite. *Science* **2012**, *338*, 643-647.
- [3] Liu, M.; Johnston, M.B.; Snaith, H.J. Efficient Planar Heterojunction Perovskite Solar Cells by Vapour Deposition. *Nature* **2013**, *501*, 395-398.
- [4] Burschka, J.; Pellet, N.; Moon, S.J.; Humphry-Baker, R.; Gao, P., Nazeeruddin, M.K.; Grätzel, M. Sequential Deposition as a Route to High-Performance Perovskite-Sensitized Solar Cells. *Nature* **2013**, *499*, 316-319.
- [5] Jeon, N.J.; Noh, J.H.; Kim, Y.C.; Yang, W.S.; Ryu, S.; Seok, S.I. Solvent Engineering for High-Performance Inorganic-Organic Hybrid Perovskite Solar Cells. *Nature Mater.* **2014**, *13*, 897-903.
- [6] Zhang, J.; P. Barboux, P.; T. Pauporté T. Electrochemical Design of Nanostructured ZnO Charge Carrier Layers for Efficient Solid-State Perovskite-Sensitized Solar Cells. *Adv. Energy Mater.* **2014**, *4*, 1400932.
- [7] Nie, W.Y.; Tsai, H.H.; Asadpour, R.; Blancon, J.C.; Neukirch, A.J.; Gupta, G.; Crochet, J.J.; Chhowalla, M.; Tretiak, S.; Alam, M.A.; High-efficiency solution-processed perovskite solar cells with millimeter-scale grains. *Science*, **2015**, *347*, 522-525.
- [8] Zhang, J.; Juárez-Pérez, E. J. ; Mora-Seró I. ; Viana, B.; Pauporté T. Fast and Low Temperature Growth of Electron Transport Layers for Efficient Perovskite Solar Cells. *J. Mater. Chem. A.*, **2015**, *3* 4909–4915.
- [9] Zhang, J.; Pauporté T. Effect of Oxide Contact Layer on the Preparation and Properties of CH<sub>3</sub>NH<sub>3</sub>PbI<sub>3</sub> for Perovskite Solar Cell Application. *J. Phys. Chem. C*,

**2015**, *119*, 14919–14928.

[10] Zhang J.; Th. Pauport é T. One-Dimensional Free-Standing TiO<sub>2</sub> Nanotube Arrays Designed for Perovskite Solar Cells Application. *ChemPhysChem*, **2015**, *16*, 2836 – 2841.

[11] Saliba, M.; Matsui, T.; Seo, J.Y.; Domanski, K.; Correa-Baena, J.P.; Nazeeruddin, M.K.; Zakeeruddin, S.M.; Tress, W.; Abate, A.; Hagfeldt, A. Cesium-containing triple cation perovskite solar cells: improved stability, reproducibility and high efficiency. *Energy Env. Sci.* **2016**, *9*, 1989-1997.

[12] You, J.B.; Meng, L.; Song, T.B.; Guo, T.F.; Yang, Y.; Chang, W.H.; Hong, Z.R.; Chen, H.J. Zhou, H.P.; Chen, Q. Improved air stability of perovskite solar cells via solution-processed metal oxide transport layers, *Nat. Nanotechnol.* 2016, *11*, 75

[13] [http://www.nrel.gov/pv/assets/images/efficiency\\_chart.jpg](http://www.nrel.gov/pv/assets/images/efficiency_chart.jpg)

[14] Vivo, P.; Ojanper, A.; Smatt J.H.; Sanden S.; Hashmi, S.G.; Kaunisto K.; Ihalainen, P.; Masood M.T.; Osterbacka R.; Lund, P.; Lemmetyinen, H. Influence of TiO<sub>2</sub> compact layer precursor on the performance of perovskite solar cells. *Org. Electron.* **2017**, *41*, 287-293.

[15] Liu, F.; Dong, Q.; Wong, M.K.; Djurišić, A.B.; Ng, A.; Ren, Z.; Shen, Q.; Surya, C.; Chan, W.K.; Wang, J.; Ng, A.M.C.; Liao, C.; Li, Shih, Wei, C.; Su H.; Dai J. Is excess PbI<sub>2</sub> beneficial for perovskite solar cell Performance? *Adv. Energy Mater.* **2016**, *6*, 1502206

[16] Yates H.M.; Afzaal, M.; Walter, A.; John L.; Hodgkinson, J.L.; Moon, S.J.; Sacchetto, D.; Brauninger, M.; Niesen, B.; Nicolay, S.; McCarthy, M.; Pemble, M.E.; Povey I.M.; Ballif C. Progression towards high efficiency perovskite solar cells via optimisation of the front electrode and blocking layer. *J. Mater. Chem. C* **2016**, *4*, 11269—11277.

[17] Zhang, C.; Luo, Y.; Chen, X.; Ou-Yang, W.; Chen, Y.; Sun, Z.; Huang, S. Influence of different TiO<sub>2</sub> blocking films on the photovoltaic performance of perovskite solar cells, *Appl. Surf. Sci.* **2016**, *388*, 82–88.

[18] Zhang, S.; Lei, L.; Yang, S.; Li, X.; Liu, Y.; Gao, Q.; Gao, X.; Cao, Q.; Yu, Y.

Influence of TiO<sub>2</sub> blocking layer morphology on planar heterojunction perovskite solar cells . *Chem. Lett.* **2016**, *45*, 592-594.

[19] Gao, Q.; Yang, S.W.; Lei, L.; Zhang, S.D.; Cao, Q.P.; Xie, J.J.; Li, J.Q.; Liu, Y.; An Effective TiO<sub>2</sub> Blocking Layer for Perovskite Solar Cells with Enhanced Performance, *Chem. Lett.* **2015**, *44*, 624-626.

[20] A.K. Chadiran, A. Yella, M.T. Mayer, P. Gao, M.K. Nazeeruddin, M. Grätzel, Sub-nanometer conformal TiO<sub>2</sub> blocking layer for high efficiency solid-state perovskite absorber solar cells. *Adv. Mater.* **2014**, *26*, 4309-4312.

[21] T.-S. Su, T.S.; T.-Y. Hsieh, T.Y.; C.-Y. Hong, C.Y.; T.-C. Wei, T.C. Electrodeposited ultrathin TiO<sub>2</sub> blocking layers for efficient perovskite solar cells. *Sci. Rep.*, **2015**, *5*, 16098.

[22] Ohsaka, T.; Izumi, F; Fujiki, Y. Raman spectrum of anatase TiO<sub>2</sub>. *J. Raman Spec.* **1978**, *7*, 321-324.

[23] Balachandran, U.; Erer N.G. Raman-spectra of titanium dioxide. *J. Solid State Chem.* **1982**, *42*, 276-282.

[24] Zhang, W.F.; He, Y.L.; Zhang, M.S.; Yin, Z.; Chen, Q. Raman scattering study on anatase TiO<sub>2</sub> nanocrystals. *J. Phys. D: Appl. Phys.* **2000**, *33*, 912-916.

[25] Magne, C.; Dufour, F.; Labat, F.; Lancel, G.; Durupthy, O.; Cassaignon, S.; Pauport é T. Effects of TiO<sub>2</sub> nanoparticle polymorphism on dye-sensitized solar cell photovoltaic Properties. *J. Photochem. Photobiol. A*, **2012**, *232*, 22-31.

[26] Fabregat-Santiago, F.; Garcia-Belmonte, G.; Mora-Sero, I.; Bisquert, J., Characterization of nanostructured hybrid and organic solar cells by impedance spectroscopy. *Phys. Chem. Chem. Phys.* **2011**, *13*, 9083-9118.

[27] Guerin, V. M.; Rathousky, J.; Pauporte, T. Electrochemical design of ZnO hierarchical structures for dye-sensitized solar cells. *Sol. Energy Mater. Sol. Cells* **2012**, *102*, 8-14.

[28] Magne, C. ; Moehl, T. ; Urien, M. ; Grätzel, M. ; Pauport é T. Effects of ZnO Film Growth Route and Nanostructure on Electron Transport and Recombination in Dye-Sensitized Solar Cells. *J. Mater. Chem. A* **2013**, *1*, 2079 - 2088.

[29] Fabregat-Santiago, F.; Bisquert, J.; Palomares, E.; Otero, L.; Kuang, D.B.;

- Zakeeruddin, S.M.; Gratzel, M. Correlation between photovoltaic performance and impedance spectroscopy of dye-sensitized solar cells based on ionic liquids. *J. Phys. Chem. C* **2007**, *111*, 6550-6560.
- [30] Kusumawati, Y.; Hosni, M.; Martoprawiro, M.A.; Cassaignon, S.; Pauport é T. Charge Transport and Recombination in TiO<sub>2</sub> Brookite Photoelectrode. *J. Phys. Chem. C* **2014**, *11*, 23459-23467.
- [31] Hosni, M.; Kusumawati, Y.; Farhat, S.; Jouini, N.; Ivansyah, A.L.; Martoprawiro, M.A.; Pauport é T. Ruthenium Polypyridyl TG6 Dye for the Sensitization of Nanoparticle and Nanocrystallite Spherical Aggregate Photoelectrodes. *ACS Applied Mater. Interfaces*, **2015**, *7*, 1568–1577.
- [32] Pascoe A.R.; Duffy, N.W.; Scully, A.D.; Huang, F.; Cheng, Y.B. Insights into Planar CH<sub>3</sub>NH<sub>3</sub>PbI<sub>3</sub> Perovskite Solar Cells Using Impedance Spectroscopy. *J. Phys. Chem. C* **2015**, *119*, 4444–4453
- [33] Juarez-Perez, E.J.; Wußler, M.; Fabregat-Santiago, F.; Lakus-Wollny, K.; Mankel, E.; Mayer, T.; Jaegermann, W.; Mora-Sero, I. Role of the Selective Contacts in the Performance of Lead Halide Perovskite Solar Cells. *J. Phys. Chem. Lett.* **2014**, *5*, 680–685.
- [34] Guerrero, A.; Garcia-Belmonte, G.; Mora-Sero, I.; Bisquert, J.; Kang, Y.S.; Jacobsson, T.J.; Correa-Baena, J.P.; Hagfeldt, A. Properties of Contact and Bulk Impedances in Hybrid Lead Halide Perovskite Solar Cells Including Inductive Loop Elements. *J. Phys. Chem. C* **2016**, *120*, 8023–8032.
- [35] Juarez-Perez, E.J.; Sanchez, R.S.; Badia, L.; Garcia-Belmonte, G.; Kang, Y.S.; Mora-Sero, I.; Bisquert, J. Photoinduced Giant Dielectric Constant in Lead Halide Perovskite Solar Cells. *J. Phys. Chem. Lett.* **2014**, *5*, 2390–2394.
- [36] Dualeh, A.; Moehl, T.; T éreault, N.; Teuscher, J.; Gao, P.; Nazeeruddin, M.K.; Gr äzel, M. Impedance Spectroscopic Analysis of Lead Iodide Perovskite-Sensitized Solid-State Solar Cells. *Sci. Rep.* **2014**, *8*, 362–373.
- [37] Gonzalez-Pedro, V.; Emilio J. Juarez-Perez, E.J.; Waode-Sukmawati Arsyad, W.S.; Eva M. Barea, E.M.; Francisco Fabregat-Santiago, F.; Ivan Mora-Sero, I.; Juan Bisquert, J. General Working Principles of CH<sub>3</sub>NH<sub>3</sub>PbX<sub>3</sub> Perovskite Solar Cells.

*Nano Lett.* **2014**, *14*, 888–893.

[38] Almora, O.; Zarazua, I.; Mas-Marza, E.; Mora-Sero, I.; Bisquert, J.; Garcia-Belmonte, G. Capacitive dark currents, hysteresis, and electrode polarization in lead halide perovskite solar cells. *J. Phys. Chem. Lett.* **2015**, *6*, 1645–1652.

[39] Guerrero, A.; Juarez-Perez, E. J.; Bisquert, J.; Mora-Sero, I.; Garcia-Belmonte, G. Electrical field profile and doping in planar lead halide perovskite solar cells. *Appl. Phys. Lett.* **2014**, *105*, 133902.

[40] Almora, O.; Guerrero, A.; Garcia-Belmonte, G. Ionic charging by local imbalance at interfaces in hybrid lead halide perovskites. *Appl. Phys. Lett.* **2016**, *108*, 043903.

[41] Kim, H.-S.; Mora-Sero, I.; Gonzalez-Pedro, V.; Fabregat-Santiago, F.; Juarez-Perez, E. J.; Park, N.-G.; Bisquert, J. Mechanism of carrier accumulation in perovskite thin-absorber solar cells. *Nat. Commun.* **2013**, *4*, 2242.

[42] Zarazua, I.; Han, G.F.; Boix, P.P.; Mhaisalkar, S.; Fabregat-Santiago, F.; Mora-Sero, I.; Bisquert, J.; Garcia-Belmonte, G. Surface Recombination and Collection Efficiency in Perovskite Solar Cells from Impedance Analysis. *J. Phys. Chem. Lett.*, **2016**, *7*, 5105-5113.

[35] Juarez-Perez, E. J.; Sanchez, R.S.; Badia, L.; Garcia-Belmonte, G.; Kang, Y. S.; Mora-Sero, I.; Bisquert, J. Photoinduced giant dielectric constant in lead halide perovskite solar cells. *J. Phys. Chem. Lett.* **2014**, *5*, 2390–2394.

[43] Yang, T.-Y.; Gregori, G.; Pellet, N.; Grätzel, M.; Maier, J. The significance of ion conduction in a hybrid organic-inorganic lead iodide- based perovskite photosensitizer. *Angew. Chem., Int. Ed.* **2015**, *54*, 7905–7910.

[44] Kim, H.-S.; Jang, I.-H.; Ahn, N.; Choi, M.; Guerrero, A.; Bisquert, J.; Park, N.-G. Control of I-V Hysteresis in CH<sub>3</sub>NH<sub>3</sub>PbI<sub>3</sub> Perovskite Solar Cell. *J. Phys. Chem. Lett.* **2015**, *6*, 4633–4639.

[45] Li, L.; Wang, F.; Wu, X.; Yu, H.; Zhou, S.; Zhao, N. Carrier- Activated Polarization in Organometal Halide Perovskites. *J. Phys. Chem. C* **2016**, *120*, 2536–2541.

[46] Brug, G.J.; Van Der Eeden, A.L.G.; Sluyters-Rehbach, M.; Sluyters, J.H. The

analysis of electrode impedance complicated by the presence of a constant phase element. *J. Electroanal. Chem.* **1984**, *176*, 275-295.

[47] Zhuang, Q.; Xu, J.; Fan, X.; Wei, G.; Dong, Q.; Jiang, Y.; Huang, L.; Sun, S. LiCoO<sub>2</sub> electrode/electrolyte interface of Li-ion batteries investigated by electrochemical impedance spectroscopy. *Sci. China, Ser. B: Chem.* **2007**, *50*, 776–783.

[48] Radvanyi, E.; Van Havenbergh, K.; Porcher, W.; Jouanneau, S.; Bridel, J.-S.; Put, S.; Franger, S. Study and modeling of the Solid Electrolyte Interphase behavior on nano-silicon anodes by Electrochemical Impedance Spectroscopy. *Electrochim. Acta* **2014**, *137*, 751– 757.

# Chapter 3. Formamidinium and methylammonium dual organic cations hybrid perovskite solar cells

## 3.1 Introduction

Perovskite solar cells prepared by laboratory-scale spin-coating methods have made tremendous progresses in the past few years in terms of efficiency and stability.[1, 2, 3, 4, 5] Such rapid progresses are mainly due to major advances made in the control of perovskite film deposition and crystallization.[6, 7, 8] However, devices made via large scale methods are still lagging behind state-of-the-art spin-coated devices because of the complicated nature of perovskite crystallization from a precursor state.[3, 9]

We know that the thermodynamics phase transition theory that  $\Delta G_c = RT \ln(C_0/C)$ , with R the constant of perfect gases and T the temperature.  $C_0$  is the solution concentration at saturation. For the spontaneous prompting of the phase transition (PT), the crystallization Gibbs energy must be negative, (i.e.  $\Delta G_c < 0$ ). It will be the case when  $C > C_0$ , here C is the supersaturation concentration of precursor solution. So the supersaturation concentration of precursor solution (C) is the main driving force for the phase transition. For example, the vacuumed-assisted crystallization process (upon which solvent rapidly volatilizes to increase C), and the anti-solvent dripping process achieved condensed perovskite thin film. Generally, the precursors are dissolved in dimethyl formamide (DMF) which is a viscous, low boiling point solvent. Because anti-solvent, such as chlorobenzene, is miscible with DMF with a decreased azeotropic point, it promotes the quick solvent evaporation and simultaneously un-dissolves perovskite seeds. The rapid increase of the perovskite precursors concentration (C) enforce the phase transition. Besides, the supersaturation vapor pressure (P) is another force for PT. The crystallization Gibbs energy is new written:  $\Delta G_c = RT \ln(P_0/P)$ , here  $P_0$  is the pressure of phase equilibrium, The crystallization requires  $P > P_0$ . Techniques such as vapor deposition,

vapor-assisted methods improve the crystalline quality of the perovskite layer and realize the stability of grains in either single crystal optoelectronic devices or solar cells absorber layers.

In Chapter 3, we develop various techniques to get large grain well-crystallized, pure phase FAMA perovskite. We will first describe a simple direct perovskite film-forming method which does not employ a dripping step by an anti-solvent. On the other hand, although tremendous efforts have been devoted to high efficiency perovskite solar cells (PSCs) on the small active areas, one of the main problems is that the anti-solvent dripping technology very easily leads to inhomogeneous perovskite layer in the center of substrate. Therefore, the technology suffers from low reproducibility on lab-to-lab and person-to-person.

In addition, many research groups have proposed the synthesis of big-sized perovskite grains, in order to reduce the interface between grains for further decreasing charge carrier recombination at the perovskite grains boundary. Therefore, we also developed a hot-casting technique to form layer made of 1-2 micrometer big-size perovskite grains.

At the end of the chapter, we will show that, developing a deposition method with anti-solvent dripping, we could finally realize highly efficient and reproducible perovskite photovoltaic devices.

## **3.2 Experiments**

In this chapter, we develop three kinds of technologies to deposit dual formamidinium/methylammonium organic cation (FAMA) perovskite layers. The various deposition methods and compositions of perovskite precursor solution realized specific advantages for perovskite layers. For example, the direct film-forming technology without anti-solvent dripping, is advantageous to realize large areas and homogenous perovskite layer. The hot-casting technology is advantageous to attain big-size perovskite grains and dramatically reduce the recombinations at the grain boundaries. Finally, via anti-solvent dripping method, we

achieved high efficiency and stability power conversion outputting on the small active areas.

We now detail the fabrication procedures of the solar cells for the various FAMA preparation protocols.

### **Substrates cleaning**

The F-doped tin oxide coated glass (TEC7, Pilkington) was cut, and etched patterned using HCl 10% and Zn powder. It was then cleaned for 20 min in a concentrated 2.5 mol.L<sup>-1</sup> NaOH ethanolic solution, rinsed with water, cleaned with a detergent, rinsed with MilliQ water and dried with compressed air. The substrates were then annealed 30 min at 500 °C on a hotplate.

### **Compact and mesoporous TiO<sub>2</sub> layers preparations**

A 20–30 nm dense compact layer of TiO<sub>2</sub> was deposited on FTO substrate by spraying pyrolysis technology at 455 °C, which precursor solution was prepared by mixing 600 µL titanium isopropoxide and 400 µL acetyl acetone (fuel of reaction, also named combustion synthesis method) in 6 mL isopropoxide solvent. The substrate was placed on a hotplate at 455 °C for 20 min prior to start spraying. The deposited layer was then annealed at 455 °C for 40 min before to be let to cool down. Then a 150–200 nm thick mesoporous TiO<sub>2</sub> layer was deposited by spin-coating on the sprayed TiO<sub>2</sub> blocking layer. 40 µL of a solution of 30 nm TiO<sub>2</sub> particle paste (Dyesol 30 NR-D paste diluted by ethanol with a 1:8 mass ratio) was deposited on the substrate and spin-coated for 20s at 4000 rpm with an initial ramp of 2000 rpm/s. The mesoporous layer was dried at 100 °C on a hot-plate and immediately sintered at 500 °C for 30 min on a covered the hotplate under dry air flux.

For experiments using only the TiO<sub>2</sub>-compact layer to investigate its impact on electron extraction, we will note in the following that the TiO<sub>2</sub> electron transport layer is without TiO<sub>2</sub>-mesoporous layer.

### **TiO<sub>2</sub>/PCBM electron transporting layer**

For studying PCBM (a fullerene derivative, [6,6]-phenyl-C61-butyric acid methyl ester) to investigate the electron injection enhancement, a 15 mmol PCBM dissolved in acetonitrile (ACN) solution was prepared. 50 µL of this PCBM solution was

deposited on the FTO/TiO<sub>2</sub>-compact/TiO<sub>2</sub>-mesoporous substrate and spin-coated at 4000 rpm for 20 s (the acceleration was 2000 rpm/s). After that, these PCBM coated substrates were placed on a hot-plate at 100 °C for 10 min, and cooled down before to proceed to the perovskite deposition.

## **Perovskite layers preparation**

### **1. Direct perovskite film-forming method (the simplest perovskite film-forming technique).**

The dual formamidinium (FA) and methylammonium (MA) organic cations are set at the following formula FA<sub>0.83</sub>MA<sub>0.17</sub>Pb(I<sub>0.83</sub>Br<sub>0.17</sub>)<sub>3</sub>. The perovskite precursor solution contained FAI, MAI, and HBr acid. The latter, being added as Lewis acid, usually can reduce the chemical reaction enthalpy to promote reaction rate. In here, we prepared a high concentration of precursor solution, mixing 1.1M PbI<sub>2</sub>, 1M FAI, 0.22 M MAI, and 0.51M HBr in dimethyl formamide (DMF). On the other hand, we also prepared a precursor solution with low concentration by mixing 1M PbI<sub>2</sub>, 0.83M FAI, 0.17 M MAI, and 0.51M HBr in DMF. 45 µL of the precursor solution was deposited on the TiO<sub>2</sub> mesoporous substrate, and then spun it at 1000 rpm for 20s (acceleration speed was 500 rpm/s) and 6000 rpm for 30s (acceleration speed was 3000 rpm/s). No anti-solvent dripping process was employed in this case. The coating perovskite layer was then annealed at 100 °C for 40 min.

For exploring optimized annealing time experiments, we tried to anneal under the various heating times for 5s, 10 min, 20 min, 30 min, 40 min, and 1 hour.

### **2. Hot-casting method for growth big-sized perovskite grains**

The precursor solution was composed of 1M FAI, 0.2M MABr, 1.1M PbI<sub>2</sub> and 0.22M PbBr<sub>2</sub> dissolved in dimethyl formamide (DMF) solvent. We adopted hot-casting technology to prepare layers made of big-sized perovskite grains. The detailed process is the following: preheated hot-plate at 150 °C for half an hour or more, and the prepared FAMA precursor solution was heated at 70 °C and stirred on another hot-plate for a half hour. After that, the preheated TiO<sub>2</sub> substrates was placed on the head of the spin-coater and 45µL of the prepared FAMA precursor solution was deposited on the substrate. The spinning was run at 6000 rpm for 30s (acceleration

speed was 3000 rpm/s). After the deposition of the perovskite layer, the sample was immediately placed on the hot-plate and heated at 150 °C for 20 min.

### **3. General anti-solvent dripping method for perovskite layer preparation**

The dual organic cations FAMA perovskite compounds was set the following formula:  $\text{FA}_{0.83}\text{MA}_{0.17}\text{Pb}(\text{I}_{0.83}\text{Br}_{0.17})_3$ . The precursor solution was composed of 1M FAI, 0.2M MABr, 1.1M  $\text{PbI}_2$  and 0.22M  $\text{PbBr}_2$  in anhydrous dimethyl formamide (DMF) and dimethylsulfoxide (DMSO) solvent mixture in a 4:1 volume ratio. 45  $\mu\text{L}$  of the perovskite precursor solution was deposited on the FTO/ $\text{TiO}_2$ -compact/ $\text{TiO}_2$ -mesoporous substrate and spin-coated at 1000 rpm for 10 s (500 rpm/s acceleration speed) for the first stage of program; and 6000 rpm for 30 s (3000 rpm/s acceleration speed) for the second stage of the program. During the second stage after 10s, 100  $\mu\text{L}$  of Chlorobenzene (CB) was dripped on the substrate. After the perovskite deposition, the perovskite layer was annealed at 100 °C for 1 hour.

#### **Hole transporting layers**

After the perovskite layer annealing, the substrates were cooled down for a few minutes. In here, Spiro-OMeTAD was used as the hole transporting material (HTM) layer. Spiro-OMeTAD precursor solution was doped with bis(trifluoromethylsulfonyl)-imide lithium salt solution (Li-TFSI, Sigma Aldrich), tris(2-(1H-pyrazol-1-yl)-4-tert-butylpyridine)-cobalt(III)-tris(bis-(trifluoromethylsulfonyl)imide) (FK209, Dyesol), and 4-tert-Butylpyridine (tBP, Sigma Aldrich). The molar ratio of additives for spiro-OMeTAD was: 0.5, 0.03, and 3.3 for Li-TFSI, cobalt complex FK209 and tBP, respectively. The solution was prepared by dissolving 0.1 g of Spiro-OMeTAD in 1.279 mL chlorobenzene. Then, 23  $\mu\text{L}$  of Li-TFSI solution (196 mg in 379  $\mu\text{L}$  ACN), 39  $\mu\text{L}$  of TBP and 18 $\mu\text{L}$  of Co-TFSI (99 mg in 263  $\mu\text{L}$  ACN) were added to this solution. 35  $\mu\text{L}$  of the Spiro-OMeTAD solution was spin-coated at 4000 rpm for 20 s.

#### **Back contact electrode**

Finally, the device was completed by thermally evaporating a 70–80 nm thick gold back electrode on the Spiro-OMeTAD layer.

### **3.3 Results and discussion**

In here, we will discuss about the effects of the various perovskite deposition technologies on the perovskite crystallinity, phase purity, morphology, and stability.

#### **3.3.1 Preparation of high purity FAMA perovskite by direct film-forming method**

Although tremendous progresses using laboratory-scale anti-solvent methods have been made during the last few years, this method is only suitable for fabricating small active area perovskite solar cells (PSCs). Spin-coating technology is a limit for industrial large area production and anti-solvent dripping is very difficult to control reproducibly lab-to-lab and person-to-person. Therefore, we have studied a simple direct film-forming technology which could be applied to commercial production machines, such as: roll-to-roll, or ink-jet printer.

Therefore, we developed a new strategy for the direct forming of perovskite layers without anti-solvent dripping, which even demonstrated more purity phase than traditional method. Figure 3.1 compares the XRD patterns of direct film-forming and traditional anti-solvent dripping technology. It is found that phase segregation occurs (mixed-phases) in the traditional one. In addition to the FAMA ones, diffraction peaks are also indexed to the yellow  $\delta$ -phase at  $11.58^\circ$  and to the  $\text{PbI}_2$  phase at  $12.7^\circ$  in the (anti-solvent) FAMA perovskite XRD pattern. On the other hand, in our direct film-forming case, the XRD patterns only exhibit the high purity photoactive black  $\alpha$ -phase notably at around  $14.3^\circ$ . Besides, we found that a slight excess of FAI precursor solution of FAMA perovskite gives rise to a better phase crystallinity, to a highly preferred (110) orientation. It also exhibits extremely sharp and narrow perovskite diffraction peaks. In addition, the most interesting is that without heating treatment, a self-maturation process occurred (when the deposited perovskite layers were placed in the dry air atmosphere for a half hour) which gave rise to a crystallized perovskite. It indicates that this technology promotes the spontaneous phase transition

even without heating treatment which might be due to a reduction of the Gibbs free energy of the whole crystallization reaction. We also note in Figure 3.1 that the annealing treatment of the sample results in XRD patterns with extremely intense and narrow diffraction peaks compared to the no heated ones. It implies that the heating treatment makes perovskite further grow up and promote its high crystallinity.

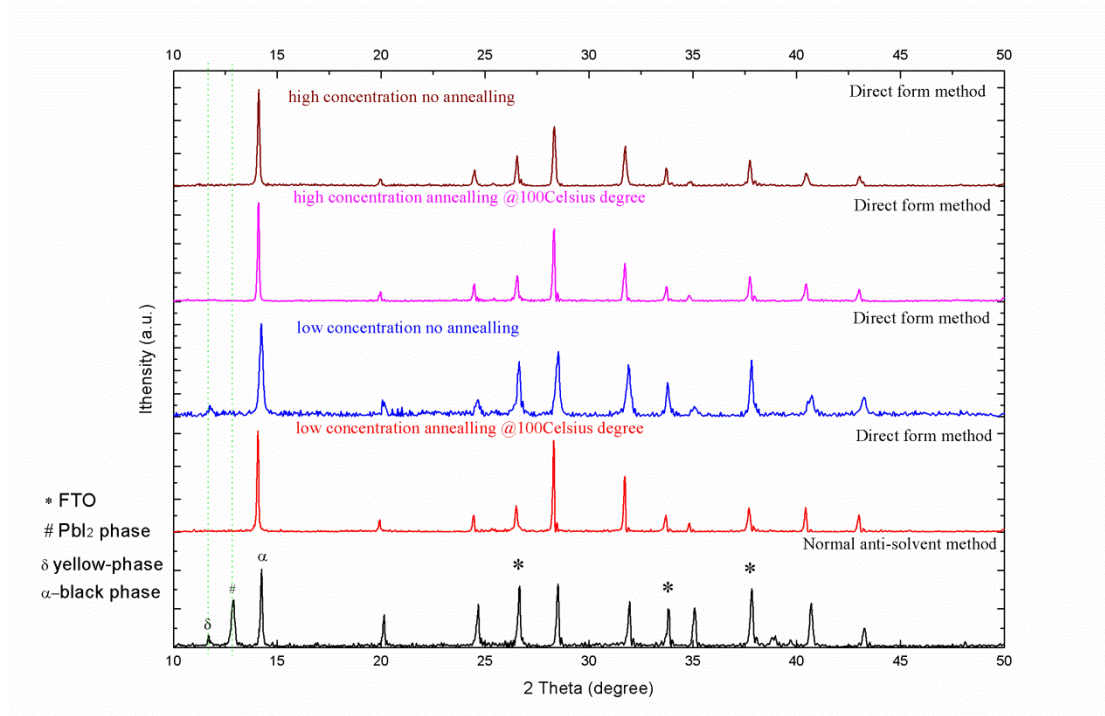


**Figure 3.1** X-ray diffraction (XRD) patterns of FAMA perovskite layer prepared by simple direct film-forming method (the first four patterns) and anti-solvent method (the bottom pattern). Effect of low and high precursor solution concentration and annealing for FAMA prepared by direct film-forming method. The symbol \* is F-doped tin dioxide, # is un-reacted  $\text{PbI}_2$  phase,  $\delta$  is non-photoactive yellow phase and  $\alpha$  is phase photoactive black phase.

In addition, we have studied in detail the effect of annealing time on the phase transition of the FAMA perovskite. In the Figure 3.2, The XRD patterns of the layers for various heating treatment of times are exhibited. Especially, for the extremely short annealing time of 5s, we found both the  $\text{PbI}_2$  phase and the perovskite  $\alpha$ -phase in the XRD pattern. However, after just an annealing time of 10min, the XRD pattern displayed almost complete transition to the perovskite  $\alpha$ -phase. It indicates that  $\text{PbI}_2$

phase gradually transfers to perovskite  $\alpha$ -phase during an extended heating treatment. Besides, the best phase purity was achieved for 40 min. After 1h, the  $\text{PbI}_2$  phase at  $12.7^\circ$  appeared meaning that the perovskite  $\alpha$ -phase started to decompose.

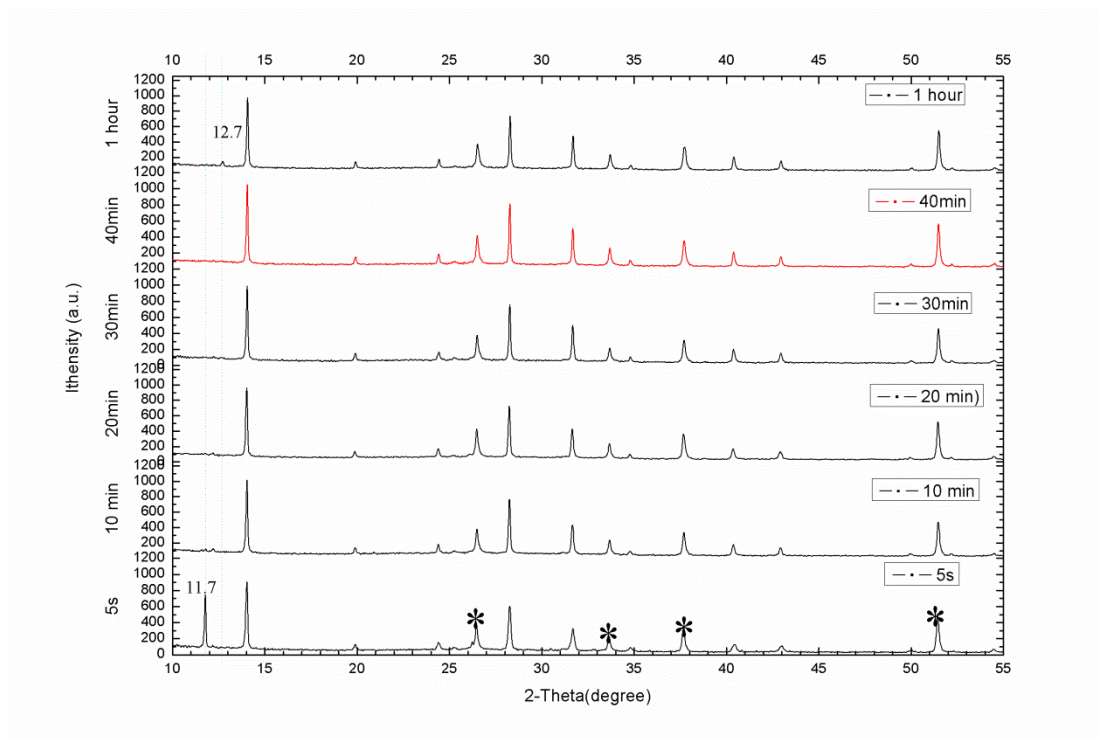


**Figure 3.2** XRD patterns of FAMA perovskite layer by direct film-forming method, under the different annealing times, 5second, 10 min, 20 min, 30 min, 40 min and 1 hour, respectively.

According to the UV-vis absorption spectrum (Figure 3.3), after coating the perovskite layer by the directly film-forming method, both high and low concentration of perovskite precursor solutions demonstrated a strong absorption. However, the inset of Figure 3.3 shows that the two films had a different optical band edge: the high concentration one was at 1.606 eV, while the low concentration one was at 1.55 eV. It indicates that the perovskite precursor composition has a strong effect on the material band-gap.

The absorbance of the layer was followed as a function of the annealing time for the low concentration precursor solution. Figure 3.4 indicates that with a prolonged heating treatment time, the absorbance of the layers increases. It is in good agreement with the results of top view perovskite SEM images detailed below (Figure 3.5).

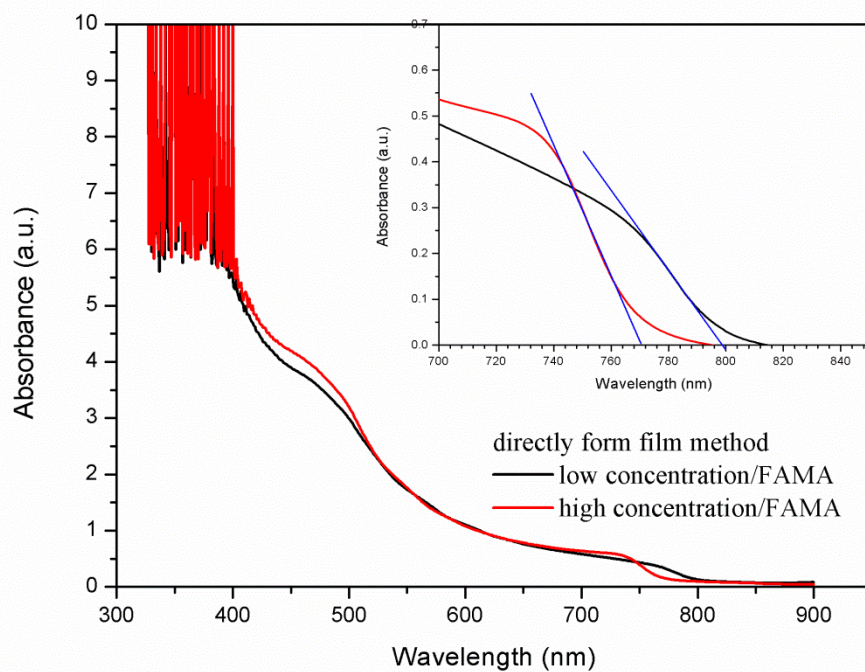


**Figure 3.3** Ultraviolet-visible (UV-vis) absorption spectrum of FAMA perovskite layer by direct film-forming method prepared from the high and low concentrations of precursor solution. The inset is a zoom of the bandgap edge.

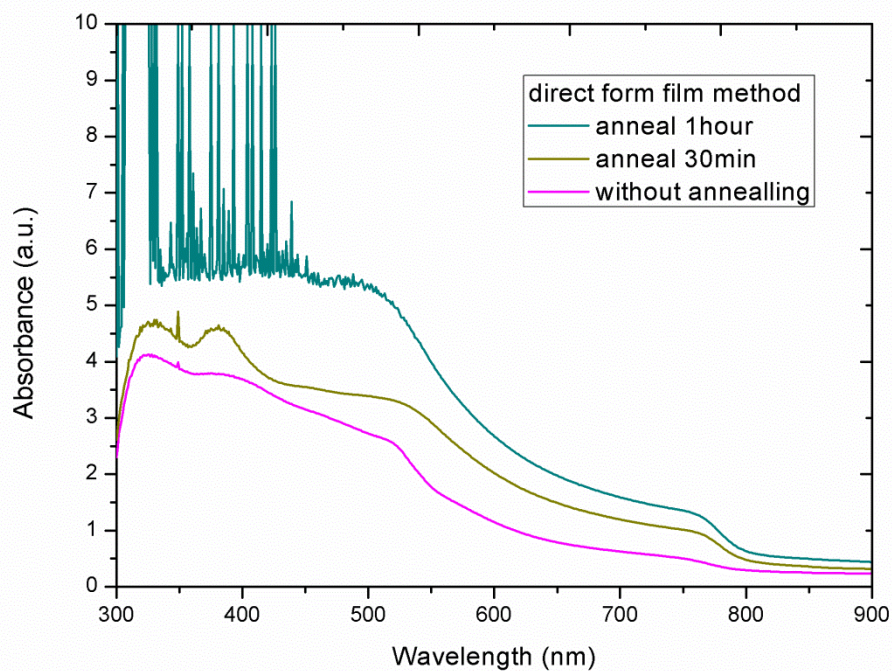


**Figure 3.4** UV-vis absorption spectra of FAMA perovskite layers without annealing

and for annealing times of 30 min and 1h.

In figure 3.5, shows the effect of precursor solution concentration and annealing on the layer morphology and size of perovskite grains. Although our XRD study has shown that, without annealing, a good crystallinity and purity  $\alpha$ -phase of perovskite was get, the grains were not fully covering the substrate as shown in Figure 3.5(a) and (c). After the heating treatment, the perovskite grains were further grown up and mature and the coverage was promoted (see Figure 3.5 (b) and (c)). Moreover, the SEM images show that the higher concentration gives rise to a better crystallization. Unfortunately, it still exists some pinholes near the boundary of grains in the perovskite layer. Until now, we do not know what causes this reaction. Generally speaking, these pinholes are detrimental for the solar cells. Actually, it results in short circuit in the cell caused by the direct contact between Spiro-OMeTAD and TiO<sub>2</sub> electron transporting layer. This increases the dark parasitic current, recombination and decreases the  $J_{sc}$  and  $V_{oc}$  of the cells.

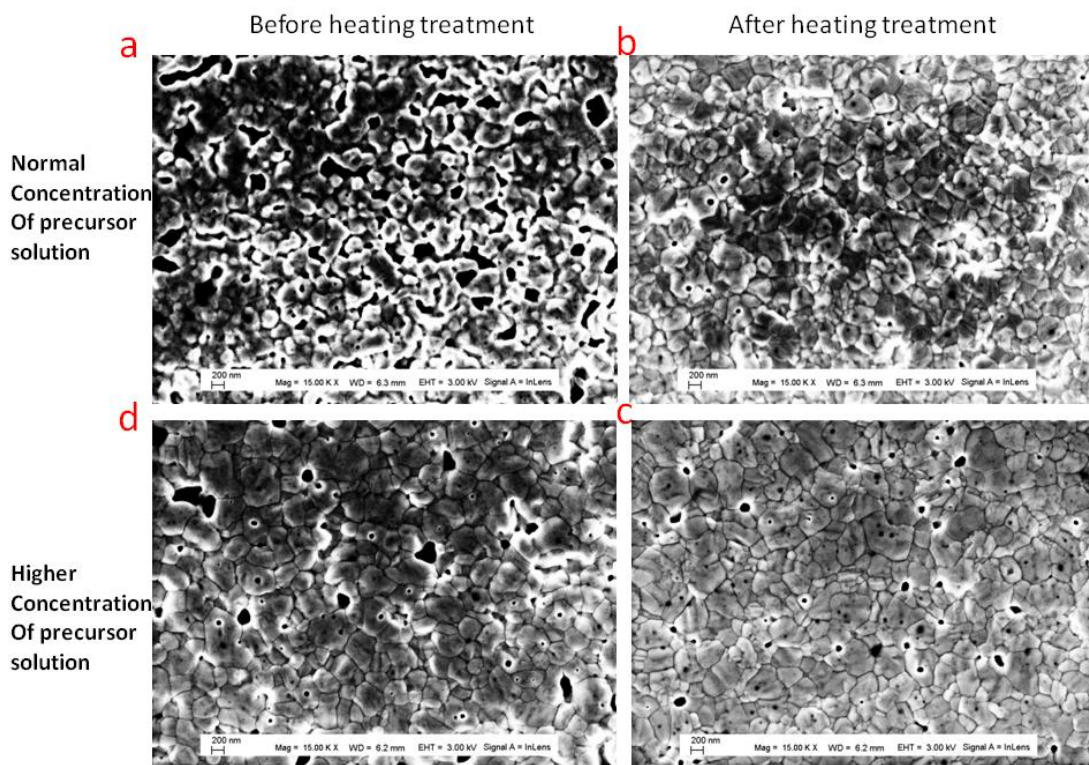


**Figure 3.5** Top views of scanning electron microscopy (SEM) images of perovskite films prepared from low concentration (a,b) and high concentration (c,d) precursor solutions. The layers before heating treatment are in the left and those after heating treatment in the right. The scale bar is 200 nm.

The direct film-forming technology realizes high purity  $\alpha$ -phase and scalable big-areas deposited perovskite layers. However, the pinholes and voids on the perovskite layer bring a deleterious impact on the solar cell performances. Figure 3.6 and Table 3.1, provide typical PSCs photovoltaic metrics of cells prepared via the directly film-forming method. They displays a  $V_{oc} = 920$  mV, a  $J_{sc} = 14.7$  mA/cm<sup>2</sup>, and a fill factor of 62.95%, resulting in a PCE of 8.54%. These pinholes and voids not only reduce the open circuit voltage but also reduce markedly the short circuit current because of the increased dark current and charge recombination near these defects.

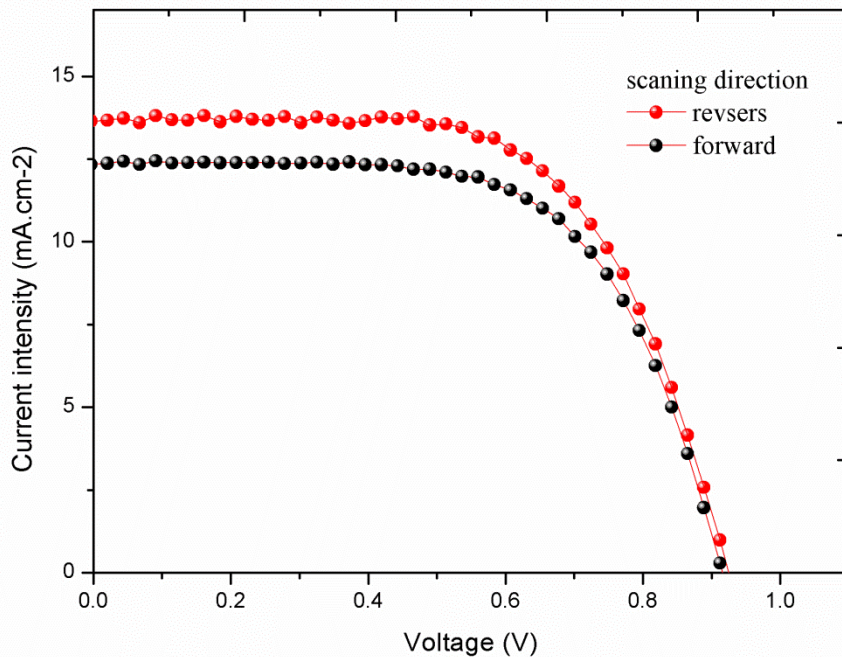


**Figure 3.6** Current density / voltage ( $J$ - $V$ ) curves of the FAMA perovskite solar cell prepared by the direct film-forming method. (Solar cell No.39 in Table 3.1)

**Table 3.1** *J-V* curve parameters for the forward and backward potential scans of FAMA perovskite solar cells prepared by the direct film-forming technology. Under AM1.5G 100 mW.cm<sup>-2</sup> illumination. The potential scan rate was 25mV/s.

Sample number	Scanning direction	V <sub>oc</sub> (V)	J <sub>sc</sub> (mA/cm <sup>2</sup> )	Fill factor (%)	PCE (%)
No.39	Reverse	0.92	14.7	62.95	8.54
	Forward	0.89	13.95	50.21	6.25
No.36	Reverse	0.94	14.29	62.89	8.51
	Forward	0.92	13.98	47.46	6.11
No.38	Reverse	0.96	13.71	62.17	8.20
	Forward	0.92	13.88	46.77	6.00

### 3.3.2 Big-sized grains of FAMA perovskite prepared by hot-casting method

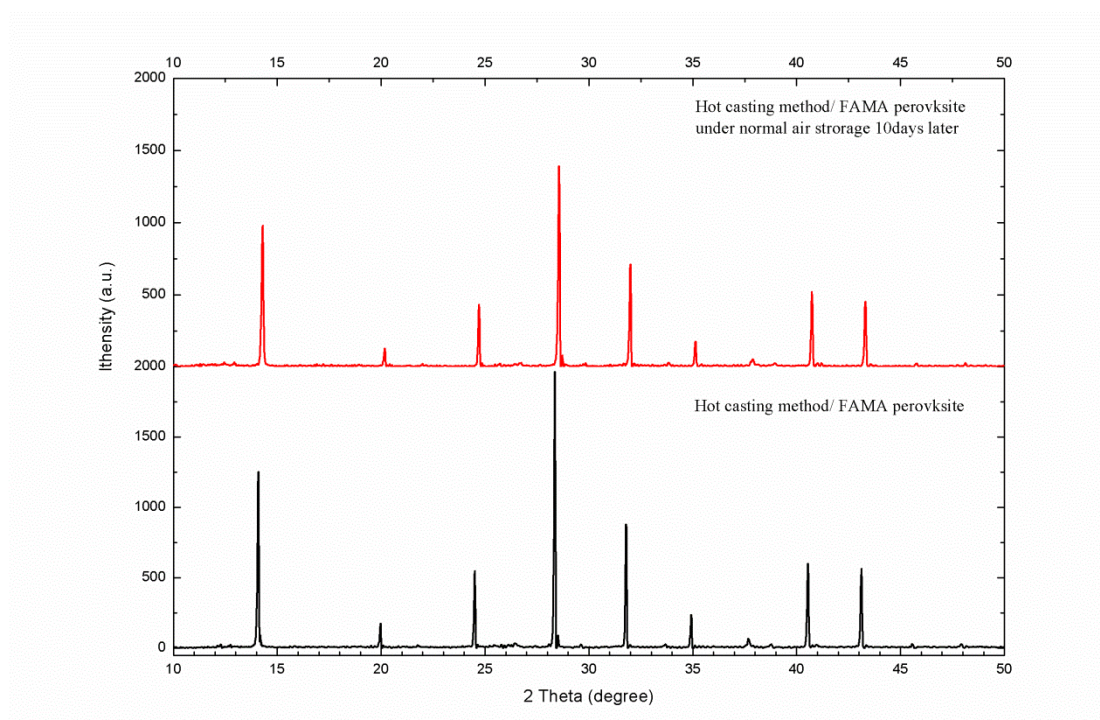
Some research groups have developed the synthesis of big-size perovskite grains to reduce the interface between the perovskite grains and then to decrease charge carrier recombination at the grains boundaries. In here, we have developed the hot-casting technology and could get perovskite grains with size as high as 1-2 micrometers.

Figure 3.7 shows the XRD patterns of FAMA perovskite layers prepared via hot-casting technology. The XRD patterns demonstrated pure photoactive perovskite  $\alpha$ -phase without other unexpected phase. It is interesting that the preferred orientations of lattice planes were changed. In here, the (110) lattice plane intensity is lower than the (220) plane one. It is unlike the layers deposited by the traditional deposition method and indicates that the crystal growth preferably occurs along the (220) lattice plane forming which is a delicate changing.

Moreover, we have followed the aging of these layers. We found that they can better endure the effect of ambient air and moisture (as we know, CH<sub>3</sub>NH<sub>3</sub>PbI<sub>3</sub> perovskite is seriously degraded by moisture), which demonstrates the higher stability of

perovskites prepared by hot-casting technology. Figure 3.7 shows the XRD pattern of a hot-casted layer after storage under ambient conditions, without any protecting treatment such as a coating protecting layer, or encapsulation. We stored these perovskite layers in a plastic box under the normal air atmosphere for 10 days (the relative moisture was above 40%). No  $\text{PbI}_2$  phase, yellow  $\delta$ -phase and other phases due to decomposition appeared after the storage.

In addition, compared to the other two kinds of perovskite deposition technologies, we found that the hot-casting method demonstrated a strongly full spectrum absorption and sharp optical band edge (Figure 3.8). It is assigned to the big-sized perovskite grains and to a thicker perovskite layer. We can note that the layer absorbance was almost increased 3 times compared to the anti-solvent method. Generally speaking, the sharp band edge absorption is a very good property for the material photoluminescence since the excitation light will be effectively excited by the above band-gap energy in this case.



**Figure 3.7** X-ray diffraction (XRD) patterns of fresh and 10-days aged FAMA perovskite layers prepared by host-casting method.

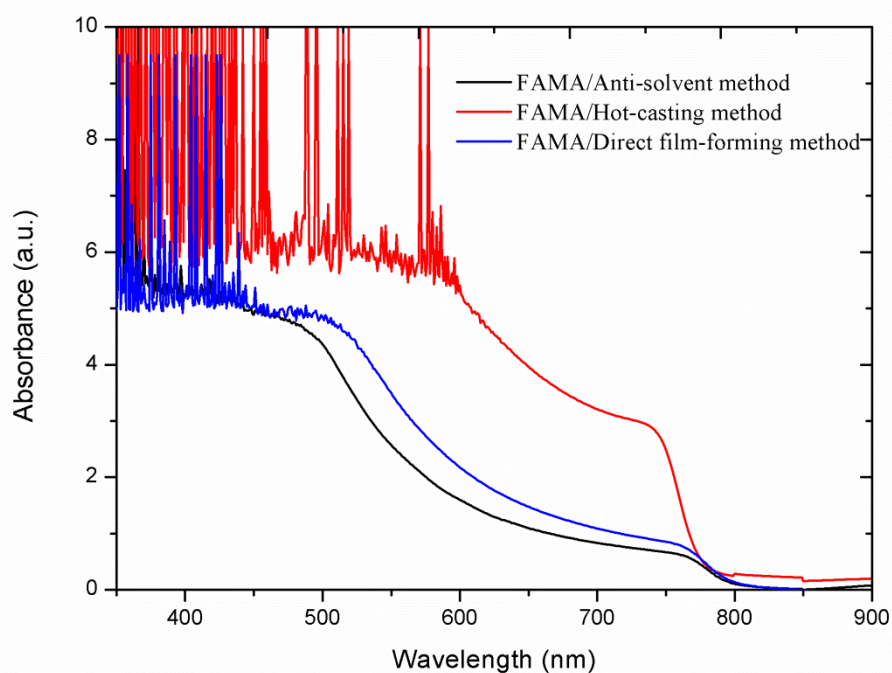


**Figure 3.8** Ultraviolet-visible (UV-vis) absorption spectra of FAMA perovskite layers prepared by different deposition techniques (anti-solvent dripping method, host-casting, and direct film-forming technique).

The morphology of layers prepared by hot-casting was imaged by SEM and is shown in Figure 3.9. We clearly observe that the layer consisted in 1-2 micrometers big grains which were surrounded by smaller perovskite grains. On the other hand, the grain size was only 200 nm in average for the other deposition techniques. The layer was fully covering the substrate and no pinholes and/or voids were present. This varying size effect is very interesting, and it results from the crystal growth mechanism. As described in the experimental part, in the hot-casting technology, when perovskite precursor solution is dripped on the preheated substrates, the solvent rapidly volatilizes and the supersaturation concentration of the precursor solution increases immediately. Therefore, perovskite crystalline seeds are easily formed and simultaneously the crystal seeds further grow up to form big-sized grains. After that, some small grains grow in-between these grains and fill the voids. In other words, the big-size grains grow first compared to the small ones.

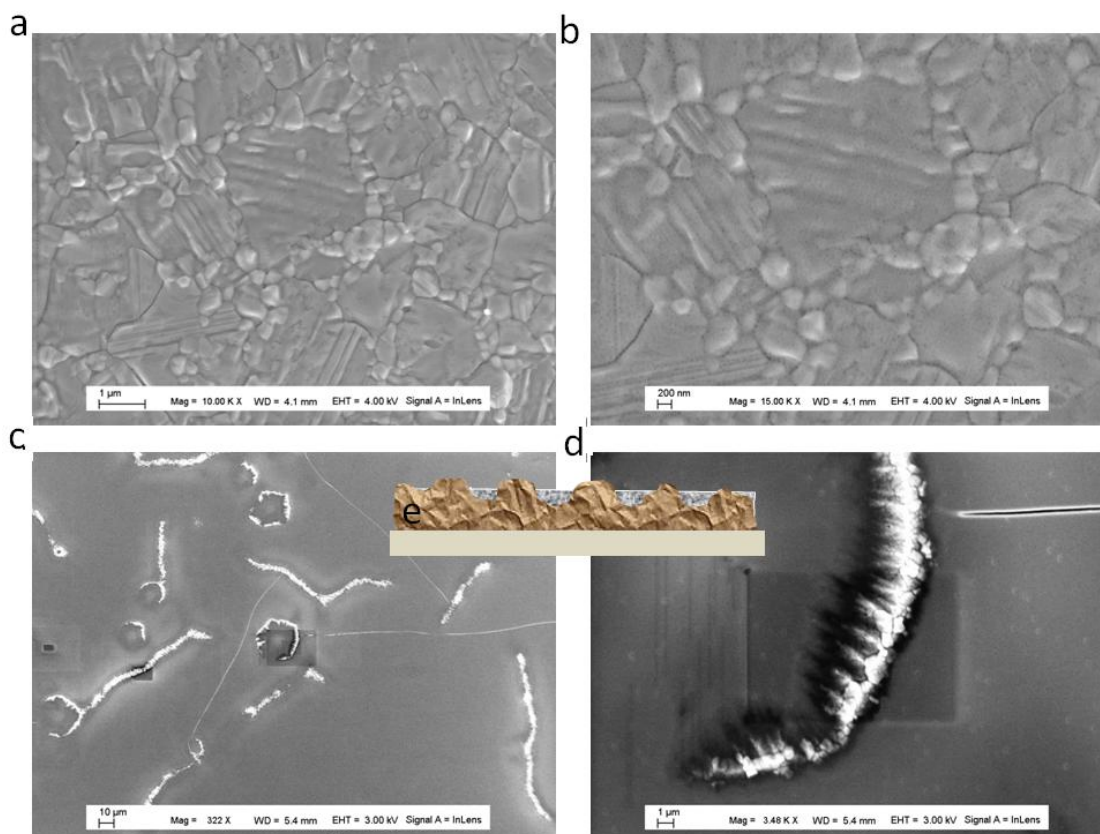


**Figure 3.9** SEM top views of hot-casted FAMA layers on mesoporous  $\text{TiO}_2$  underlayer. (a) and (b) show big-sized FAMA perovskite grains under different magnifications. (c) and (d) are SEM views of Spiro-OMeTAD (hole transporting material) deposited on top of the FAMA perovskite layer prepared by hot-casting. (e) Cross-sectional scheme of the Spiro-OMeTAD (in grey) deposited on the perovskite (in brown).

However, according to the low magnification SEM of Figure 3.10, we discovered that some places show ridge structures on the perovskite layer (these are brighter lines in figure 3.10 (a)). It may be caused by the rapid growing of the perovskite layer which induces volumetric changes. Just like mountain forming in geography, the adjacent earth plates move to together to produce highland and even mountain topography. In Figure 3.10 (b), we could clearly see the rise up of perovskite topography. At higher zoom up amplification in figure (c) and (d), the morphology is shown to be homogeneous, even at the ridge structures. No pinholes or voids were present.

Unfortunately, after the deposition of the Spiro-OMeTAD, the HTM could not fully

cover the perovskite layer as shown in Figure 3.9 (d) and (c). The schematic diagram Figure 3.9 (e) demonstrates some raised perovskite topographies are not covered by HTM from cross section, and makes top of perovskite grains exposed outside of Spiro-OMeTAD layer. Therefore, short circuit occurred in the photovoltaic devices and no photovoltaic performances could be measured.

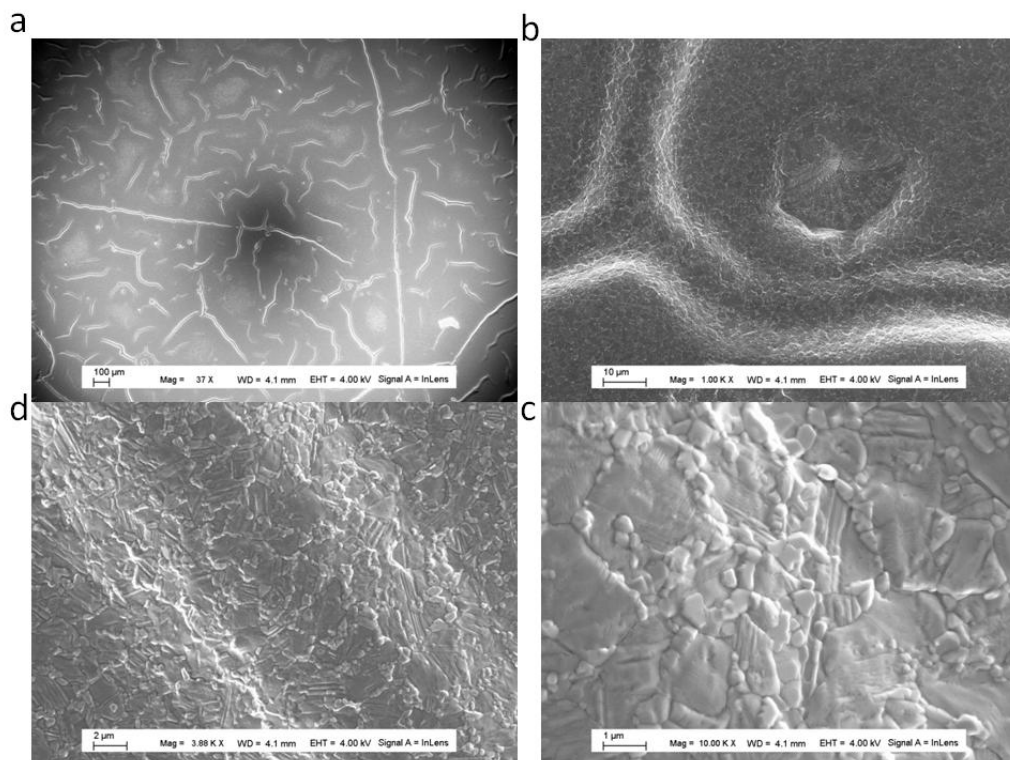


**Figure 3.10** SEM images focusing on ridge structures of perovskite (brighter lines) at various magnifications.

### 3.3.3 High efficiency FAMA perovskite by anti-solution method.

Above, we have realized the big-area FAMA perovskite deposition without artificial dripping procedure and achieved dense big-sized FAMA perovskite layers via a hot-casting method. However, we encountered morphology problems such as pinholes, voids and the ridge topography in the perovskite layer which seriously negatively affected the performances of the photovoltaic devices. Therefore, we adopted a traditional anti-solvent dripping technology to improve the coverage and the

homogeneity of the perovskite layers.

As shown above, in Figure 3.1 (bottom XRD pattern), the XRD pattern of the prepared perovskite layer includes the yellow perovskite  $\beta$ -phase at  $11.58^\circ$ , the  $\text{PbI}_2$  phase at  $12.7^\circ$ , and the black perovskite  $\alpha$ -phase at  $14.3^\circ$ . However, fortunately, the black  $\alpha$ -phase was the dominant one. The SEM top views of the layers in Figure 3.11(a), (b), (c) and (d), shows some bright small grains which grow up along the perovskite grain boundaries. These bright small grains were found on the SEM images for various amplifications. A first hypothesis was that these bright grains are also perovskite grains like the bottom perovskite layer, their brightness in SEM images being due to the sloping section of grains that gathers a lot of secondary electrons (because of different grains orientation, such as sloping section and flat topography).

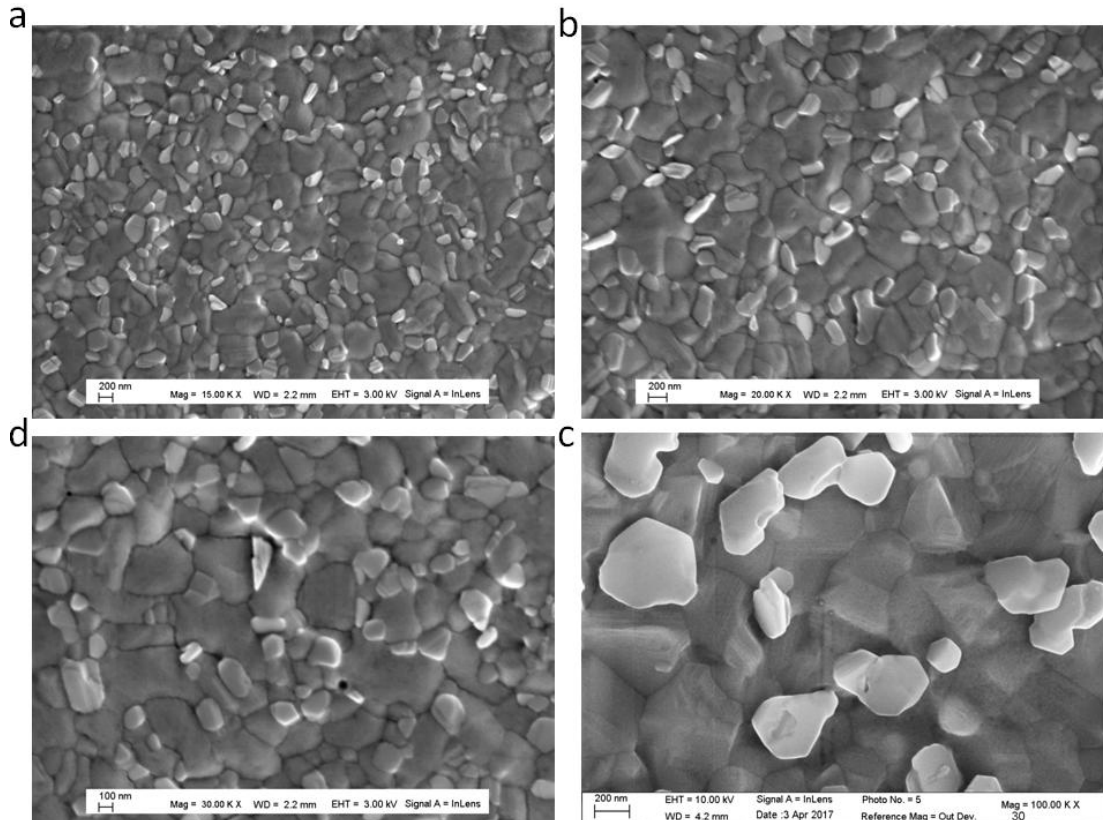


**Figure 3.11** SEM top views at various magnifications of the FAMA perovskite layer prepared via the general anti-solvent dripping method.

Many scholars found phase separation and impurity phase in FAMA perovskite. We first adopted the reflected backscattered-electron (RBSE) detection mode to identify that bright grains are  $\text{PbI}_2$  phase in the same image by split screen technology (Figure 3.12). The RBSD mode is used to detect contrast between areas with different chemical compositions. Actually, in RBSE the heavy elements appear brighter than the light ones. In our case, FAMA perovskite consisted in  $\text{Pb}^{2+}$ ,  $\Gamma$ ,  $\text{Br}^-$  and organic groups. In here, the most heavy element is Pb. In the Figure 3.12, the RBSD signal image shows the some bright grains compared to the grey perovskite grains. It indicates that these bright grains are heavy element (Pb) rich. Therefore, we assign these bright grains to  $\text{PbI}_2$ . However, the SE2 (secondary electrons) signal image just displays the same contrast, so the SE2 signal image generally describes perovskite morphology picture. Besides, it is noteworthy that we deliberately chose a sample zone with pinhole defects in the perovskite layer to label the reference position more easily.

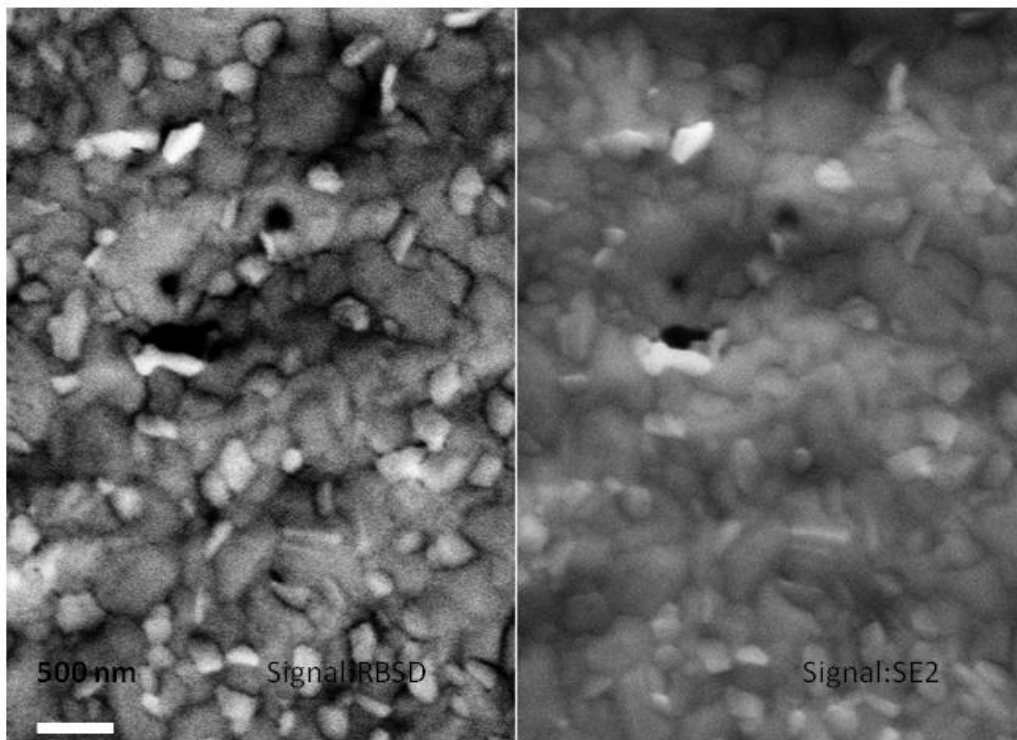


**Figure 3.12** Scanning electron microscopy (SEM) images of FAMA perovskite layer

at the same position by spilt screen technology, using different electronic signals: reflected back-scattered electrons (RBSD) in the left image, and secondary electrons (SE2) in the right image.

To deeply understand the excited charge carriers dynamics in the layer, time-correlated single-photon counting (TCSPC) experiments were conducted on the pristine FAMA and MAPbI<sub>3</sub> perovskite layers deposited on glass, a charge blocking substrate. Decay lifetime is a very important and exquisite index to quantitatively evaluate charge carriers dynamics in the perovskite materials. Especially for an absorber material of a photovoltaic device, a long decay lifetime will make sure to have enough time to extract electrons or holes and finally inject them into corresponding extraction layers. Certainly, the fluorescence decay lifetime depends on the properties of the material itself. For example, a low emission transition probability and low non-radiative transition can prolong the decay lifetime. On the other hand, some of point defects such as vacancy, interstitial particle and even foreign particle are inevitable in the crystal lattice. These defect states can trap excited charge carriers, lead to transfer from high excited energy levels to the defect state energy level which indicates making fluorescence decay lifetimes short. Therefore, the comparative study of decay lifetime change can indirectly provide a good estimation of the material crystallographic quality.

As shown in Figure 3.13, we investigated fluorescence decay dynamics of pristine FAMA perovskite and MAPbI<sub>3</sub> perovskite via the continuous deposited perovskite technology with anti-solvent dripping procedure. On the normalized curves, we obviously found a dramatic change of the decay dynamics. Compared to MAPbI<sub>3</sub> perovskite, the decay lifetime was considerably extended in the pristine FAMA perovskite. It is noticeable that the initial decay rapidly dropped in MAPbI<sub>3</sub>. This phenomenon might be explained by the fact that on MAPbI<sub>3</sub> surface it exists a lots of point defects, which induce charge carriers recombination. Actually, it is generally admitted in the literature that the initial rapid decay is assigned to charge carrier recombination on these point defects of perovskite surface.[10] Besides, the slow

decay of a behind part is assigned to the free-carrier recombination in the bulk for carriers propagating deeper in the material (crystal bulk has a better periodic lattice and with less point defects).

In Chapter 4, we adopted a biexponential function to fit the pristine FAMA decay curve, resulting in a  $\tau_{\text{fast}} = 59.04 \pm 0.5$  ns for fast decay component and  $\tau_{\text{slow}} = 1030.77 \pm 2.0$  ns for the slow decay component. On the other hand, the MAPbI<sub>3</sub> perovskite decay curve was difficult to fit by a biexponential function. But it could be fitted by a higher-order exponential function. It implies a more complex charge carrier dynamics and decay physical mechanism. The pristine FAMA perovskite sample presents an approximate linear decay curve over a large time scale, as same as some classic decay of photoluminescence materials. It indicates that the pristine FAMA perovskite attains a long decay lifetime, which supply enough time for injecting electrons and holes into the corresponding extraction layers. This excellent charge carriers separation ability paves the way to the achievement of very high efficiency FAMA perovskite solar cells.

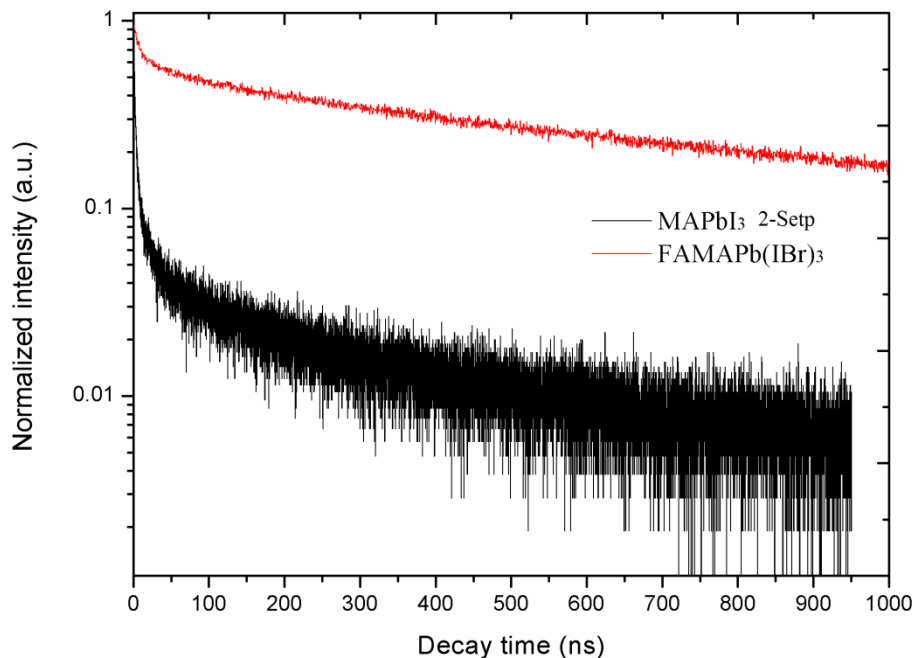


**Figure 3.13** Time-correlated single-photon counting (TCSPC) curves showing the longer lifetime of charge carriers in the pristine FAMA perovskite film compared to MAPbI<sub>3</sub> perovskite by two-step. The excitation wavelength was 470 nm.

The combination of the perovskite and the charge extraction layers is key to get highly efficient PSCs. The charges separation and extraction have been investigated by steady-state photoluminescence spectra measurements. We have investigated FAMA deposited on various extraction layers, namely (i) FAMA-compact TiO<sub>2</sub> layer, (ii) FAMA- TiO<sub>2</sub> blocking/mesoporous layer, and (iii) FAMA-Spiro TiO<sub>2</sub> layer.

The pristine FAMA deposited on glass exhibited a strong PL emission centered at 783 nm and corresponding to a PL emission energy of 1.58 eV (Figure 3.14). The PL intensity was heavily quenched when FAMA was deposited on various charge extraction layers (see Figure 3.14), which indicates that electrons or holes were efficiently extracted from the perovskite and were then injected into the corresponding extraction layers. In addition, we also found a two emission PL peaks for FAMA-Spiro sample assigned to the emission of the two layers. Actually, the hole transporting material (Spiro-OMeTAD) has its own fluorescence when excited at 470 nm.

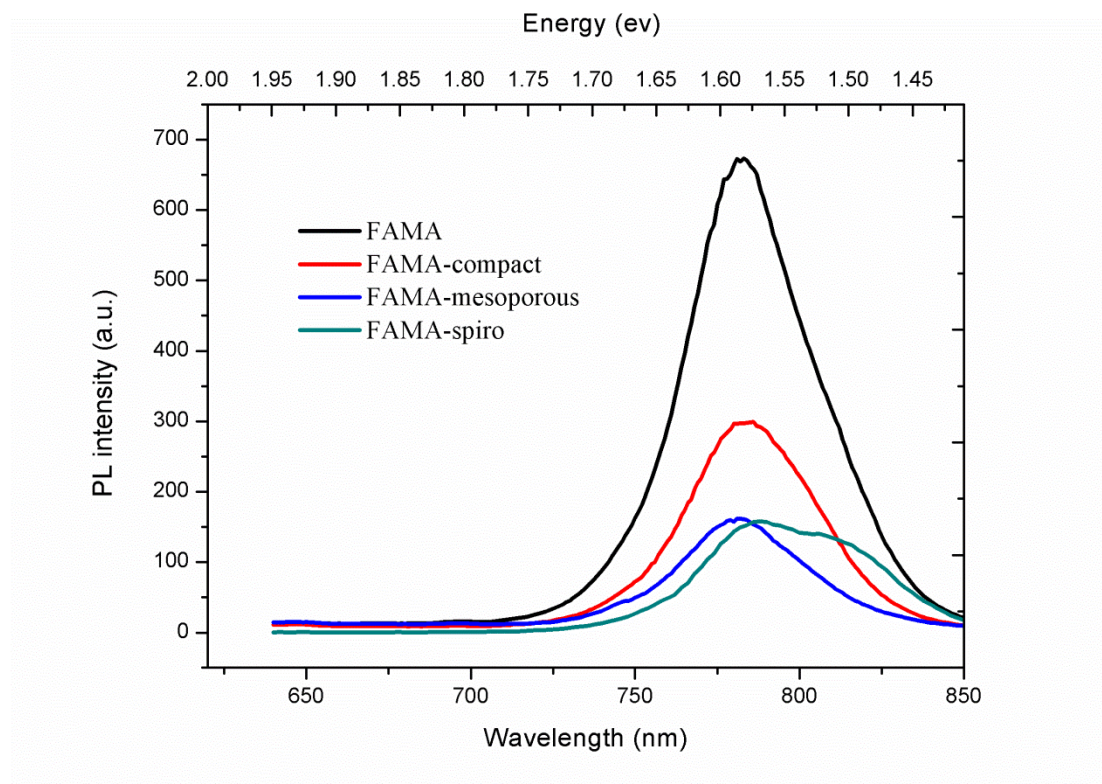


**Figure 3.14** Steady-state photoluminescence (PL) spectra of FAMA perovskite on glass and combined with various electron and hole extraction layers: TiO<sub>2</sub>/compact layer, TiO<sub>2</sub>/mesoporous layer and spiro-OMeTAD. (470 nm excitation wavelength)

The various electron and hole extraction layers combined with FAMA perovskite have also been investigated by time-correlated single-photon counting (TCSPC) measurements, namely (i) FTO/TiO<sub>2</sub>-compact electron extracted layer, (ii) FTO/TiO<sub>2</sub>-compact/TiO<sub>2</sub>-mesoporous electron extraction layer, and (iii) FTO/TiO<sub>2</sub>-compact/TiO<sub>2</sub>-mesoporous/PCBM electron extraction layer. Beside the configuration of glass/FAMA/Spiro was also investigated to get important information on holes extraction. The decay dynamics results are consistent with the steady-state PL spectra ones (Figure 3.15).

As discussed above, the pristine FAMA exhibited approximately a linear decay curve and a good convergence character at tail decay curve. On the contrary, other electron extraction layers displayed sharp a decay component. The decay curves analysis show that the FTO/TiO<sub>2</sub>-compact layer extraction time is  $\tau_{0.1} = 490$  ns, the FTO/TiO<sub>2</sub>-compact/ TiO<sub>2</sub>-mesoporous is  $\tau_{0.1} = 236$  ns, and the FTO/TiO<sub>2</sub>-compact/ TiO<sub>2</sub>-mesoporous/PCBM is  $\tau_{0.1} = 16$  ns. For the configuration of Glass/Spiro-OMeTAD, the hole extraction time is  $\tau_{0.1} = 9.26$  ns. (Here,  $\tau_{0.1}$  is the time at which the initial photoluminescence intensity decreases by a factor 10. Because the extraction layers usually demonstrate a rapid decay processe, this parameter permits a quantitative evaluation of the quenching and then of the charge transfer speed[11]). As above  $\tau_{0.1}$  results, the configurations of FTO/TiO<sub>2</sub>-compact/ TiO<sub>2</sub>-mesoporous and FTO/TiO<sub>2</sub>-compact/TiO<sub>2</sub>-mesoporous/PCBM have excellent electrons extraction properties. However, the planar configuration FTO/TiO<sub>2</sub>-compact electron extraction layer displays a different decay process. At the beginning, this decay curve shows obviously rapid decrease, indicating that it accepts electrons injection. And then it appears a slow decay process which presents a linear convergence function. It implies that planar TiO<sub>2</sub> compact layer cannot continuously supply an continuous electron extraction ability. In other words, the planar TiO<sub>2</sub> compact layer just only extracts a

few electrons at preliminary stage, and then cannot work effectively (i.e. electrons injected flux is not enough). The linear convergence of decay curve completely agrees with the above analysis. This fairly explains why TiO<sub>2</sub>/planar configuration cells usually produce poor efficiency.[3]

In comparison, the hole injection from the valence band of the perovskite into the highest occupied molecular orbital (HOMO) of Spiro-OMeTAD is more rapid than the electron injection from the conduction band of perovskite into the conduction band of TiO<sub>2</sub>. It could limit the device efficiency. Therefore, looking for a more rapid injection electrons transport layer is a key element for PSCs with higher efficiency.

Therefore, we improved the extraction ability by using the FTO/TiO<sub>2</sub>-compact/TiO<sub>2</sub>-mesoporous/PCBM configuration for the electron extraction layer. Compared to  $\tau_{0.1}=236$  ns of FTO/TiO<sub>2</sub>-compact/TiO<sub>2</sub>-mesoporous, this extraction time of  $\tau_{0.1}$  is decreased to 16 ns and demonstrates the most rapid injection ability. The specific photovoltaic metrics are discussed below in solar cell part.

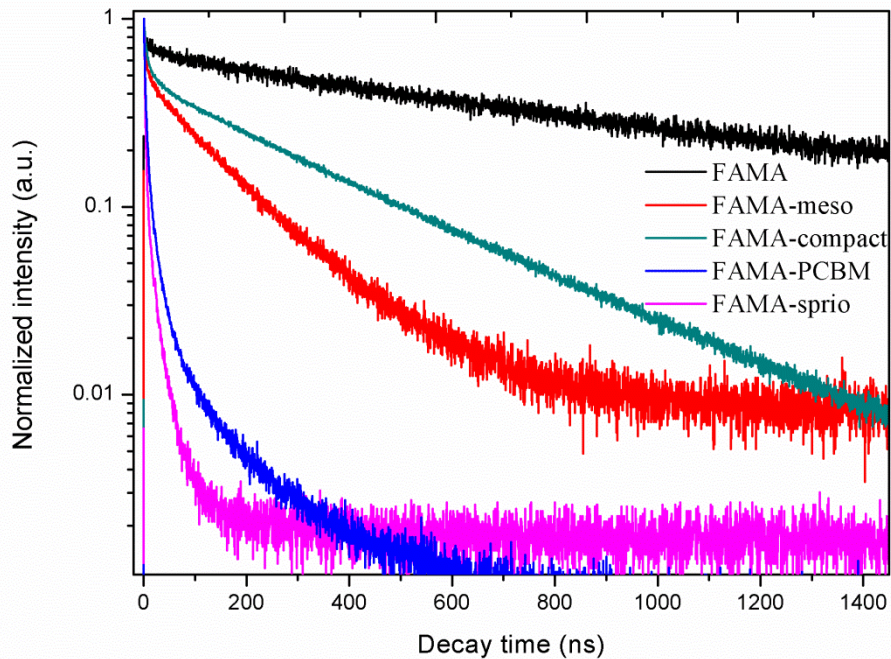


**Figure 3.15** Time-correlated single photon counting (TCSPC) curves of pristine FAMA perovskite deposited on glass and combined with various electron and hole transporting layers: TiO<sub>2</sub>-compact layer, TiO<sub>2</sub>-compact/TiO<sub>2</sub>-mesoporous layer,

TiO<sub>2</sub>-compact/ TiO<sub>2</sub>-mesoporous/PCBM layer and spiro-OMeTAD, respectively.

Perovskite solar cells have been fabricated with the various following structures:

(i) FTO/TiO<sub>2</sub>-compact/ TiO<sub>2</sub>-mesoporous/FAMA /Spiro-OMeTAD/Au

(ii) FTO/TiO<sub>2</sub>-compact/ TiO<sub>2</sub>-mesoporous/PCBM/FAMA/Spiro-OMeTAD/Au

We have investigated the photovoltaic (PV) properties of these different structures.

The photovoltaic metrics have been collected from the current-voltage  $J$ - $V$  curves of the champion FAMA devices shown in Figure 3.16. The parameters are an open circuit voltage  $V_{oc} = 1176$  mV, a short circuit current  $J_{sc} = 23.06$  mA/cm<sup>2</sup>, a fill factor  $FF = 78.2\%$ , and a power conversion efficiency (PCE) of 20.11%. The potential scan rate was 25 mV/s. To confirm the stabilized PCE outputting (and eliminating the scanning direction and speed effect), we tracked the maximum power point (MPP) under standard AM 1.5G solar illumination. Inset of figure 3.16 shows the MPP tracking for 60s, monitored at  $V_{max} = 967$  mV. The stabilized current output was 20.79 mA/cm<sup>2</sup>, yielding a stabilized efficiency of 20.11%. This result is consistent with the  $J$ - $V$  measurement, indicating that our  $J$ - $V$  measuring parameters are reliable. Generally speaking, the long-time tracking MPP results could fully present the reality of the device operating status.

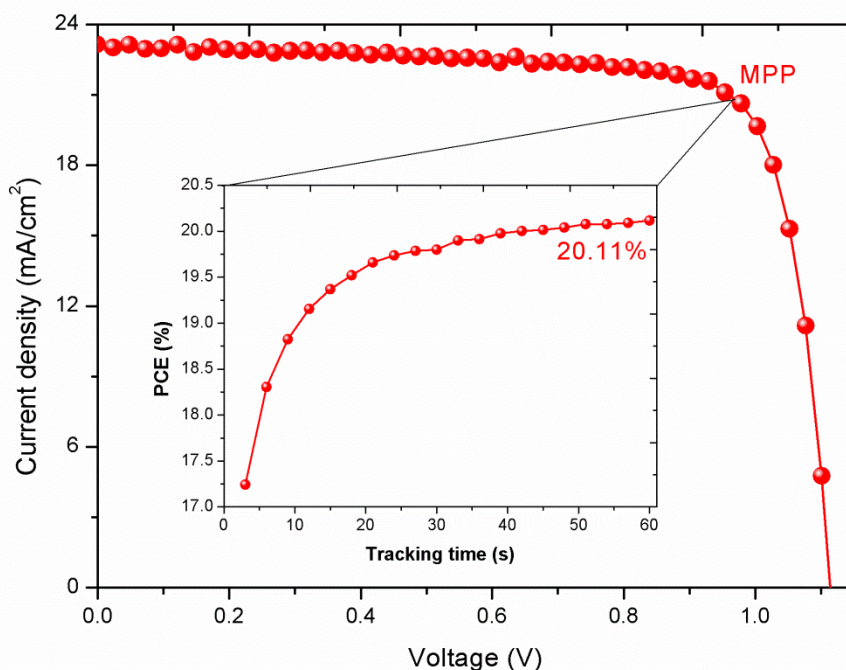


**Figure 3.16** *J-V* curve of the best FAMA solar cell performing at 20.15% ( $V_{oc} = 1176$  mV,  $J_{sc} = 23.06$  mA/cm<sup>2</sup>, and FF=78.2%), measured for a reverse scan rate of 25 mV/s. The inset shows the MPP tracking for 60s monitored at  $V_{max} = 967$  mV and which finally produced 20.79 mA/cm<sup>2</sup>, yielding stabilized efficiency of 20.11%.

We have seen above that the FTO/TiO<sub>2</sub>-compact/TiO<sub>2</sub>-mesoporous/PCBM structure can collect very rapidly the photogenerated electrons in the perovskite. We fabricated the corresponding FAMA-based PSCs, and the *J-V* curve parameters are collected under the one sun standard AM1.5G solar illumination. In Figure 3.17, with the PCBM layer, the photovoltaic device generates an open circuit voltage  $V_{oc} = 1068$  mV, a short circuit current  $J_{sc} = 25.05$  mA/cm<sup>2</sup>, and a fill factor FF = 68.6%, resulting in a power conversion efficiency PCE of 18.35%. The potential scan rate was 25mV/s. Compared to without PCBM layer, this device indeed improves short circuit current to 25.05 mA/cm<sup>2</sup>. We propose that, the more efficient electrons extraction increases the short circuit current. However, it is noticeable that this device not has a good fill factor of 68.6% that leads to an unsatisfactory device efficiency. The reason for fill factor decrease in the presence of PCBM remains to be clarified.

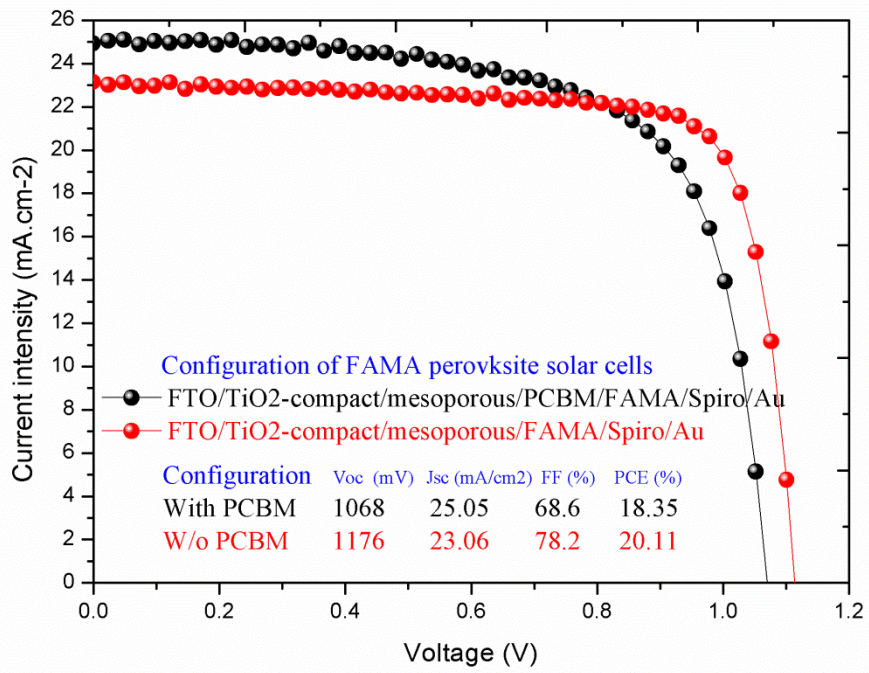


**Figure 3.17** *J-V* curve of the best FAMA perovskite solar cell with and without PCBM layer. The photovoltaic metrics details are listed at the bottom of the *J-V* curves.

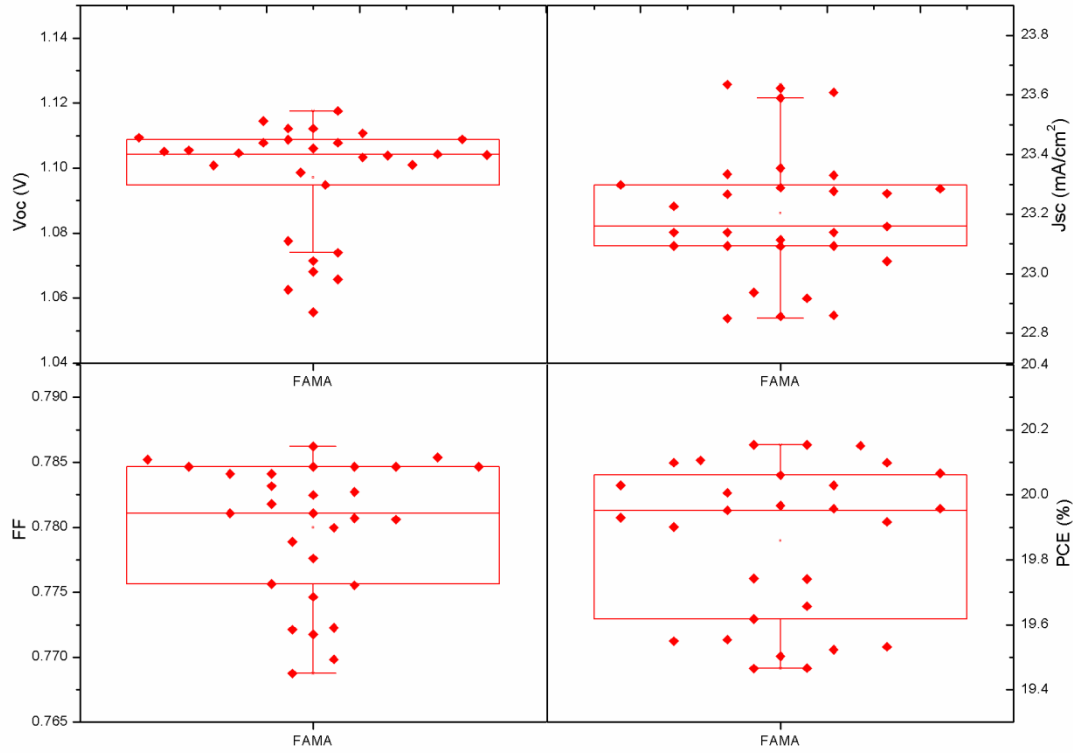


**Figure 3.18** *J-V* metrics for 30 FAMA perovskite independent devices, including  $V_{oc}$ ,  $J_{sc}$ , FF, and PCE.

To demonstrate that my FAMA perovskite solar cells could be well reproduced by anti-solvent dripping technology, the detailed inventories of photovoltaic metrics have been averaged for about 30 independent FAMA PSCs. Figure 3.18 shows the statistical distribution of these parameters. The FAMA devices showed an average value of  $V_{oc} = 1104$  mV,  $J_{sc} = 23.16$  mA/cm<sup>2</sup>, and a FF = 78%, and a PCE of 19.80%. The averaged photovoltaic metrics are close to the best performing FAMA device ( $V_{oc} = 1176$  mV, a  $J_{sc} = 23.06$  mA/cm<sup>2</sup>, FF = 78.2%, and a PCE of 20.11%). It indicates that our fabrication of FAMA perovskite solar cells is reproducible and achieves high efficiency.

### 3.4 Conclusion

In this chapter, based on thermodynamic phase transition theory  $\Delta G_c = RT \ln(C_0/C)$ , we have investigated the promotion of spontaneous crystallization and growth of FAMA

perovskite by the control of the supersaturation concentration of the precursor solution. We developed two kinds of perovskite deposition technology, the simple direct film-forming and the hot-casting methods. Firstly, the direct film-forming without dripping process realized high purity perovskite  $\alpha$ -phase. At the same time, this technique could be used for deposition at the large scale, on large surface area, of perovskite layers with considerable reproducibility by eliminating the artificial dripping problem. Secondly, the hot-casting technology realized a dense, big-grains, and high purity phase perovskite layer. This leads to further decrease grain boundaries and its detrimental effect of charge carrier recombination enhancement. However, due to morphological defects in the perovskite layer such as pinholes, voids and ridge topography, these layers did not demonstrate excellent photovoltaic properties.

Then we adopted a deposition method with the dripping by an anti-solvent step to trigger the layer crystallization. By using this technique, we finally realized high efficiency and highly reproducible perovskite photovoltaic devices. In addition, we have carried out a detailed investigation of the various charge extraction layers by TCSPC and PL spectroscopy, and obtained sound conclusions about their effect on charge carrier injection kinetics. We explained that the planar structure of TiO<sub>2</sub>-compact electron transport layer (ETL) usually not attain excellent photovoltaic properties due to slow charge injection. On the other hand, the TiO<sub>2</sub>-compact/TiO<sub>2</sub>-mesoporous/PCBM ETL achieved much more efficient electron injection. Then we conclude that the finding of a new electron transport material that could improve electron injection would breakthrough a new solar cells record.

Finally, the best performing FAMA photovoltaic devices exhibited an open circuit voltage  $V_{oc} = 1176$  mV, a short circuit current  $J_{sc} = 23.06$  mA/cm<sup>2</sup>, and a fill factor  $FF = 78.2\%$ , resulting in a power conversation efficiency (PCE) of 20.11%. The investigation of 30 independent devices demonstrated that the average photovoltaic parameters are:  $V_{oc} = 1104$  mV,  $J_{sc} = 23.16$  mA/cm<sup>2</sup>, and a  $FF = 78\%$ , and a PCE of 19.80%.

## References

1. Li Z, Yang M, Park J-S, Wei S-H, Berry JJ, Zhu K. Stabilizing perovskite structures by tuning tolerance factor: formation of formamidinium and cesium lead iodide solid-state alloys. *Chemistry of Materials*. 2015;28:284-92.
2. Hoke ET, Slotcavage DJ, Dohner ER, Bowring AR, Karunadasa HI, McGehee MD. Reversible photo-induced trap formation in mixed-halide hybrid perovskites for photovoltaics. *Chemical Science*. 2015;6:613-7.
3. Jeon NJ, Noh JH, Kim YC, Yang WS, Ryu S, Seok SI. Solvent engineering for high-performance inorganic–organic hybrid perovskite solar cells. *Nature materials*. 2014;13:897.
4. Paek S, Schouwink P, Athanasopoulou EN, Cho K, Grancini G, Lee Y, Zhang Y, Stellacci F, Nazeeruddin MK, Gao P. From Nano-to Micrometer Scale: The Role of Antisolvent Treatment on High Performance Perovskite Solar Cells. *Chemistry of Materials*. 2017;29:3490-8.
5. Yi C, Luo J, Meloni S, Boziki A, Ashari-Astani N, Grätzel C, Zakeeruddin SM, Rühlisberger U, Grätzel M. Entropic stabilization of mixed A-cation ABX<sub>3</sub> metal halide perovskites for high performance perovskite solar cells. *Energy & Environmental Science*. 2016;9:656-62.
6. Saliba M, Matsui T, Domanski K, Seo J-Y, Ummadisingu A, Zakeeruddin SM, Correa-Baena J-P, Tress WR, Abate A, Hagfeldt A. Incorporation of rubidium cations into perovskite solar cells improves photovoltaic performance. *Science*. 2016;354:206-9.
7. Saliba M, Matsui T, Seo J-Y, Domanski K, Correa-Baena J-P, Nazeeruddin MK, Zakeeruddin SM, Tress W, Abate A, Hagfeldt A. Cesium-containing triple cation perovskite solar cells: improved stability, reproducibility and high efficiency. *Energy & Environmental Science*. 2016;9:1989-97.
8. Luo D, Yang W, Wang Z, Sadhanala A, Hu Q, Su R, Shivanna R, Trindade GF, Watts JF, Xu Z. Enhanced photovoltage for inverted planar heterojunction perovskite solar cells. *Science*. 2018;360:1442-6.

9. Yang M, Li Z, Reese MO, Reid OG, Kim DH, Siol S, Klein TR, Yan Y, Berry JJ, van Hest MF. Perovskite ink with wide processing window for scalable high-efficiency solar cells. *Nature Energy*. 2017;2:17038.
10. Shi D, Adinolfi V, Comin R, Yuan M, Alarousu E, Buin A, Chen Y, Hoogland S, Rothenberger A, Katsiev K. Low trap-state density and long carrier diffusion in organolead trihalide perovskite single crystals. *Science*. 2015;347:519-22.
11. Arora N, Dar MI, Hinderhofer A, Pellet N, Schreiber F, Zakeeruddin SM, Grätzel M. Perovskite solar cells with CuSCN hole extraction layers yield stabilized efficiencies greater than 20%. *Science*. 2017:eaam5655.

# **Chapter 4 Multiple cations lead trihalide perovskite for solar cells with higher stability, reproducibility and highest efficiency.**

## **4.1 Introduction**

Although we reached high power conversion efficiency with the best PCE of 20.11%, a persistent outputting at the maxima power point (MPP) of 20.79 mA/cm<sup>2</sup>, and a relative stability in perovskite solar cells (PSCs) based on FAMA, we found that the just dual organic cation lead trihalide (such as: methylammonium (MA) CH<sub>3</sub>NH<sub>3</sub><sup>+</sup> and formamidinium (FA) CH<sub>3</sub>(NH<sub>2</sub>)<sub>2</sub><sup>+</sup>) perovskite usually exhibits impurity phase which usually includes the yellow β-phase perovskite and un-reacted PbI<sub>2</sub> phase in the photoactive black α-perovskite perovskite phase. Therefore, our work on the increase of the perovskite complexity was motivated by the improvement of perovskite ABX<sub>3</sub> structure stability, and by the obtaining of the perovskite phase with higher purity. In general, the slight changing of perovskite structure and the distorting coordination environment of perovskite structure by introducing other cations affect the phase stability [1]. Adding more inorganic elements can increase the entropy of mixing [2], leads to an excellent thermo-stability of perovskite and to the stability under PSC continuous working in real operation environment.

In addition, recently, high efficiency PSCs have been prepared using Pb-based multiple cations perovskites such as: CsMA [3], CsFA [4], CsFAMA [5], and even the quadruple RuCsFAMA [6] and KCsFAMA [7] compositions. These perovskites demonstrated surprising properties and merits. For example, CsFA/mixed halide perovskite exhibited wide bandgap adjustment ability (from 1.55 eV to 2.2 eV), delivering a complete tunability of the bandgap around 1.75 eV which is the optimum bandgap for tandem silicon/perovskite solar cells [8]. The KCsFAMA based PSCs demonstrated big-size, high quality grains and the devices achieved a 20.5% PCE

almost hysteresis-free [7]. Besides, the RuCsFAMA PSCs attained an average PCE about 20.2%, due to a high open circuit voltage at 1.24 V. This perovskite had a 1.63 eV bandgap and exhibited low non-radiative recombinations [9]. However, for Goldschmidt tolerance factor of  $ABX_3$  structure, only the inorganic  $Cs^+$  cations incorporated into perovskite can satisfy a 0.8~1 index range, to stabilize  $ABX_3$  structure [2] (except radioactive francium  $Fr^+$  monovalent cation which radius is 1.80 Å).

## 4.2 Experiments

Here, we introduce the detailed fabrication procedure of Cs5FAMA PSCs. We adopted an anti-solvent dripping method to deposit the perovskite layer [10, 11].

It is noticeable that all the perovskite layers were fabricated at dry air atmosphere (the relative humidity was kept at 8%-10%, in a "dry-box" which is a not very harsh term compared to under the low 1% relative humidity used in Ref. [12] or under the completely nitrogen atmosphere in Ref. [9]). Therefore, it implies that, even under not harshly controlled atmosphere conditions, it is possible to prepare very high efficiency PSCs. This would decrease the manufacture process requirements in the PSCs industrialized production.

### *Substrates cleaning*

The F-doped tin oxide coated glass (TEC7, Pilkington) was cut, and etched patterned using HCl 10% and Zn powder. It was then cleaned for 20 min in a concentrated 2.5 mol.L<sup>-1</sup> NaOH ethanolic solution, rinsed with water, cleaned with a detergent, rinsed with MilliQ water and dried with compressed air. The substrates were then annealed 30 min at 500 °C on a hotplate.

### *TiO<sub>2</sub> compact and mesoporous layers preparations*

A 20–30 nm dense compact layer of TiO<sub>2</sub> was deposited on FTO substrate via spraying pyrolysis technology at 450 °C which precursor solution was prepared by

mixing titanium isopropoxide and acetyl acetone in isopropoxide (volume ratio is 3:2:35 ). Then a 150–200 nm thick mesoporous TiO<sub>2</sub> layer was deposited by spin-coating. 40 μL of a solution of 30 nm TiO<sub>2</sub> particle paste (Dyesol 30 NR-D paste diluted by ethanol with a 1:8 mass ratio) was deposited on the substrate and spin-coated for 20s at 4000 rpm with an initial ramp of 2000 rpm/s. The mesoporous layer was dried at 100 °C and immediately sintered at 500 °C for 30 min on a hotplate under dry air flux.

#### *TiO<sub>2</sub>/PCBM electron transport layer*

For studying PCBM (a fullerene derivative, [6,6]-phenyl-C61-butyric acid methyl ester) to investigate the electron injection enhancement, a 15 mmol PCBM in acetonitrile (ACN) solution was prepared. 50 μL of this solution was deposited on the FTO/TiO<sub>2</sub>-compact/TiO<sub>2</sub>-mesoporous substrate and spin-coated at 4000 rpm for 20 s (the acceleration was 2000 rpm/s). After that, these PCBM coated substrates were placed on a hot-plate for 10 min at 100 °C, and cooled down before to proceed to the perovskite deposition.

Li-treatment of mesoporous TiO<sub>2</sub> was accomplished using a solution of 22 mg Li-TFSI in 1.5 mL acetonitrile. 50 μL of this solution was spin-coated at 4000 rpm for 30 s and then the sample was annealed at 500 °C for 30 min.

#### *Perovskite layers preparations*

The multiple organic monovalent cation perovskite compounds with the following formula were prepared: FA<sub>0.83</sub>MA<sub>0.17</sub>Pb(I<sub>0.83</sub>Br<sub>0.17</sub>)<sub>3</sub> and Cs-doped triple cation perovskite Cs<sub>x</sub>FA<sub>0.83</sub>MA<sub>0.17</sub>Pb(I<sub>0.83</sub>Br<sub>0.17</sub>)<sub>3</sub> (x=0.05 and 0.1). The multiple cations perovskite precursor solution was prepared by mixing FAI (1M), MABr (0.2M), PbI<sub>2</sub> (1.1M) and PbBr<sub>2</sub> (0.22M) in anhydrous DMF and DMSO (volume ratio is 4:1).

For the triple cation perovskite, CsI (1.5M) pre-dissolved solution was mixed into perovskite precursor to get the desired triple cations perovskite composition. In addition, we know that the excess lead iodide introduction is good at improving perovskite electronic properties from report.[13, 14] 45 μL of perovskite precursor solution was spin-coated on FTO/TiO<sub>2</sub>-compact/TiO<sub>2</sub>-mesoporous substrate at 1000

rpm for 10 s and 6000 rpm for 30 s. During the second step, after 20s, 100  $\mu$ L of anhydrous chlorobenzene anti-solvent was dripped on the sample. The coating perovskite layer was then annealed at 100  $^{\circ}$ C for 1 hour on a hotplate.

For the aging experiment samples, the coating perovskite layer was heated at 130  $^{\circ}$ C for 3 hours under the dry air atmosphere.

#### *Hole transporting layer and back contact preparations*

After the perovskite layer annealing, the substrates were cooled down for a few minutes. In here, Spiro-OMeTAD was used as the hole transporting materials (HTM) layer. Spiro-OMeTAD precursor solution was doped with bis(trifluoromethylsulfonyl)-imide lithium salt solution (Li-TFSI, Sigma Aldrich), tris(2-1H-pyrazol-1-yl)-4-tert-butylpyridine)-cobalt(III)-tris(bis-(trifluoromethylsulfonyl)imide) (FK209, Dynamo), and 4-tert-Butylpyridine (tBP, Sigma Aldrich). The molar ratio of additives for Spiro-OMeTAD was: 0.5, 0.03, and 3.3 for Li-TFSI, FK209 cobalt complex and tBP respectively. The detailed preparation protocol of Spiro-OMeTAD solution is the same as in chapter 3. A 35  $\mu$ L aliquot of the Spiro-OMeTAD solution was spin-coated at 4000 rpm for 20 s.

Finally, the device was completed by thermally evaporating a 70–80 nm thick gold back electrode on the Spiro-OMeTAD layer.

### **4.3 Results and discussion**

Here, we mainly discuss about the effect of Cs<sup>+</sup> cation mixing with methylammonium (MA) and formamidinium (FA) on the phase purity, thermo-stability, and high crystallinity of perovskite. We show that Cs<sup>+</sup> leads to less defects and long excited carriers lifetimes which ensure the effectively extraction of free charge carriers and injection into ETL and HTL. At the same time, we investigated the use of Cs5FAMA perovskite absorber to fabricate photovoltaic devices which achieved a high power conversion efficiency of 20.67% and a stabilized current output of 21.86 mA/cm<sup>2</sup>.

### 4.3.1 The nucleation kinetics of perovskite

Firstly, we have investigated the nucleation kinetics of Cs5FAMA and FAMA after anti-solvent dripping. Figure 4.1 shows that the two compounds exhibit dramatically different kinetic behaviors at the beginning of the nucleation process. At first, just after the injection of the anti-solvent on the prepared precursor film, a sharp rise of absorption intensity (in 40 s) was observed, which indicated that a speedily heterogeneous nucleation was occurring at solution interface [11, 15]. It was followed by a continuous increase at longer times due to a slower nucleation and growth. It implies that perovskite was rapidly nucleated after dripping and gradually continue to growth at longer time even before the annealing treatment. In comparison, the absorption intensity of Cs5FAMA is always higher than the absorption of FAMA. It indicates that  $\text{Cs}^+$  embedded into FAMA definitely improved the nucleation process before annealing.

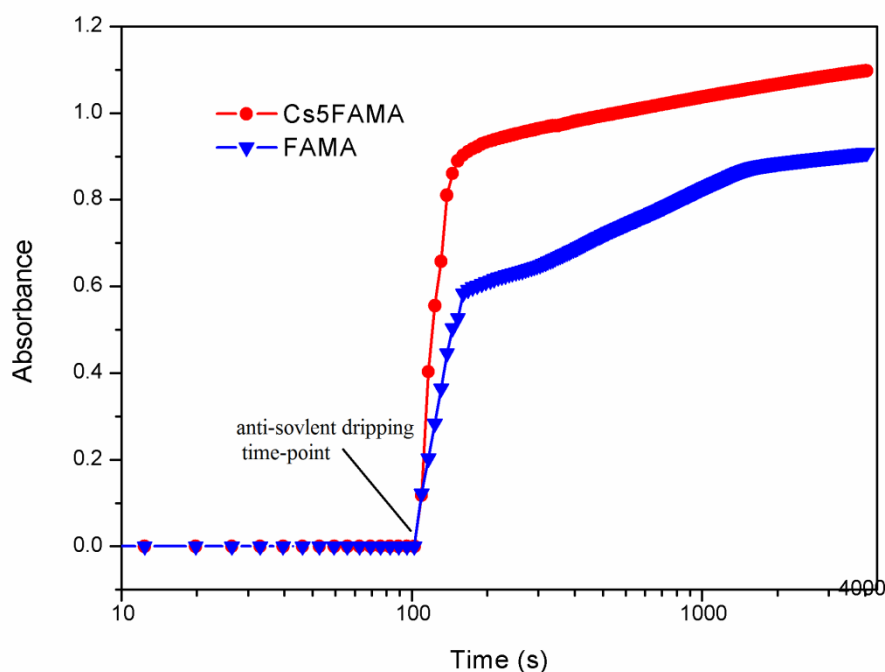


**Figure 4.1** Nucleation kinetics tracking for Cs5FAMA and FAMA, upon anti-solvent dripping. The anti-solvent was rapidly dripped after 100s on prepared precursor thin-film. The absorbance was recorded every 6 seconds and monitored at 495~500nm wavelength.

### 4.3.2 Nature of fluorescence mechanism in Cs5FAMA perovskite

Figure 4.2 shows the absorbance spectra of FAMA and Cs5FAMA layers deposited on glass and on TiO<sub>2</sub> underlayers and after their annealing at 100 °C. The perovskite materials absorb light over a large wavelength range in the visible and in the near-infrared region. They present a high absorbance, especially below 500 nm. The high absorbance shows that the crystal nuclei rapidly further grew by annealing to form condensed and mature perovskite grains.

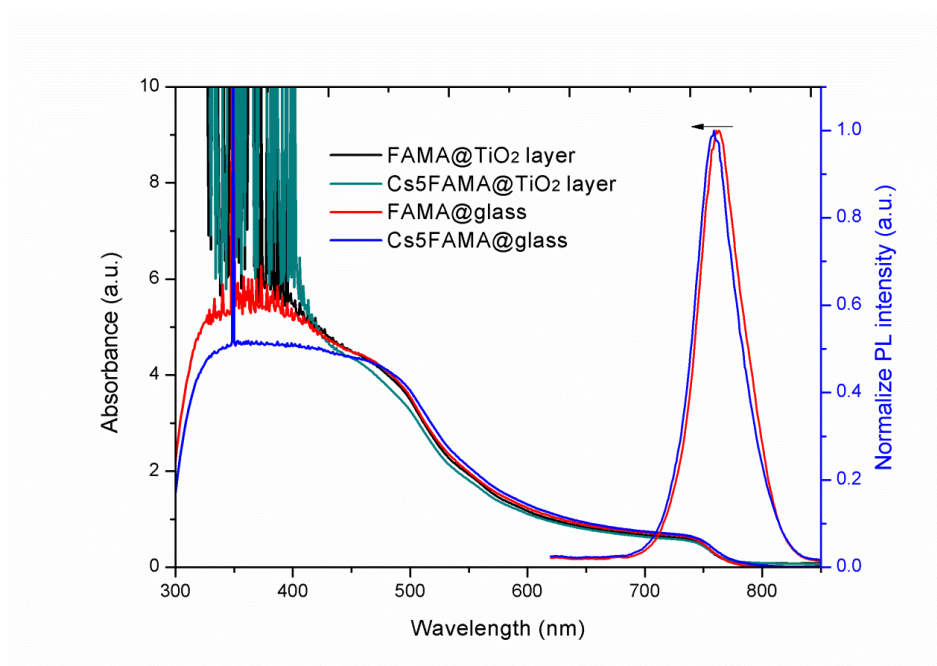


**Figure 4.2** Ultraviolet-visible (UV-vis) absorption spectra of FAMA and Cs5FAMA on the TiO<sub>2</sub> and glass substrates. The normalized photoluminescence (PL) spectra of FAMA and Cs5FAMA on glass substrate are presented on the same figure.

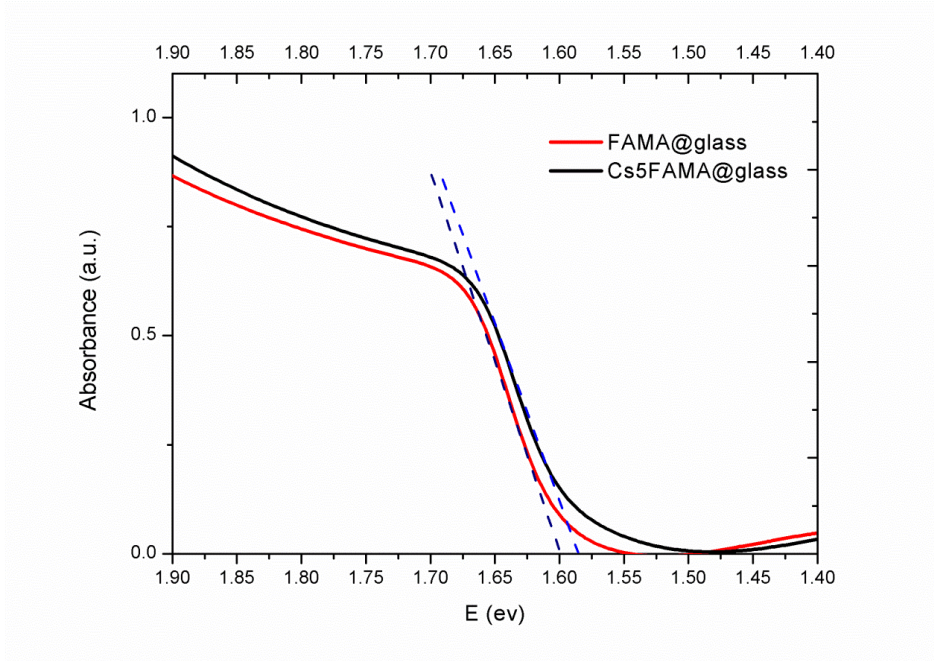


**Figure 4.3** Tauc plots at the near optical bandgap edges of both absorption spectra, which show that Cs5FAMA bandgap is 1.58 eV and FAMA bandgap is 1.60 eV.

The Photoluminescence (PL) spectra are presented in the same Figure 4.2. The emission peak of Cs5FAMA is slightly blue-shifted (5 nm) compared to FAMA. The absorbance spectra have been plotted as a Tauc plot in Figure 4.3. We found that the Cs5FAMA optical bandgap edge was red-shifted to 1.58 eV compared to FAMA measured at 1.60 eV. This implies that Cs5FAMA absorber could obtain a wider scope of wavelength to be excited, consequently giving rise to a slightly improved Cs5FAMA PSCs short circuit current ( $J_{sc}$ ) (we will show below that the  $J_{sc}$  increased from 23.31 mA/cm<sup>2</sup> to 24.1 mA/cm<sup>2</sup>, when Cs5FAMA absorber was used instead of FAMA in the PSCs).

The calculated emission energy of PL at ~1.59 eV (Figure 4.4) is basically equal to the Cs5FAMA forbidden band gap of 1.58 eV. It indicates that the Cs5FAMA perovskite is a direct semiconductor like typical MAPbI<sub>3</sub> perovskite [16]. In direct semiconductors, the conduction band (CB) bottom and the valence band maximum (VB) have the same position in Brillouin zone. Electrons are directly excited without phonon momentum and the electron-hole pair recombination produces a highly

efficient photoluminescent emission [9, 13].

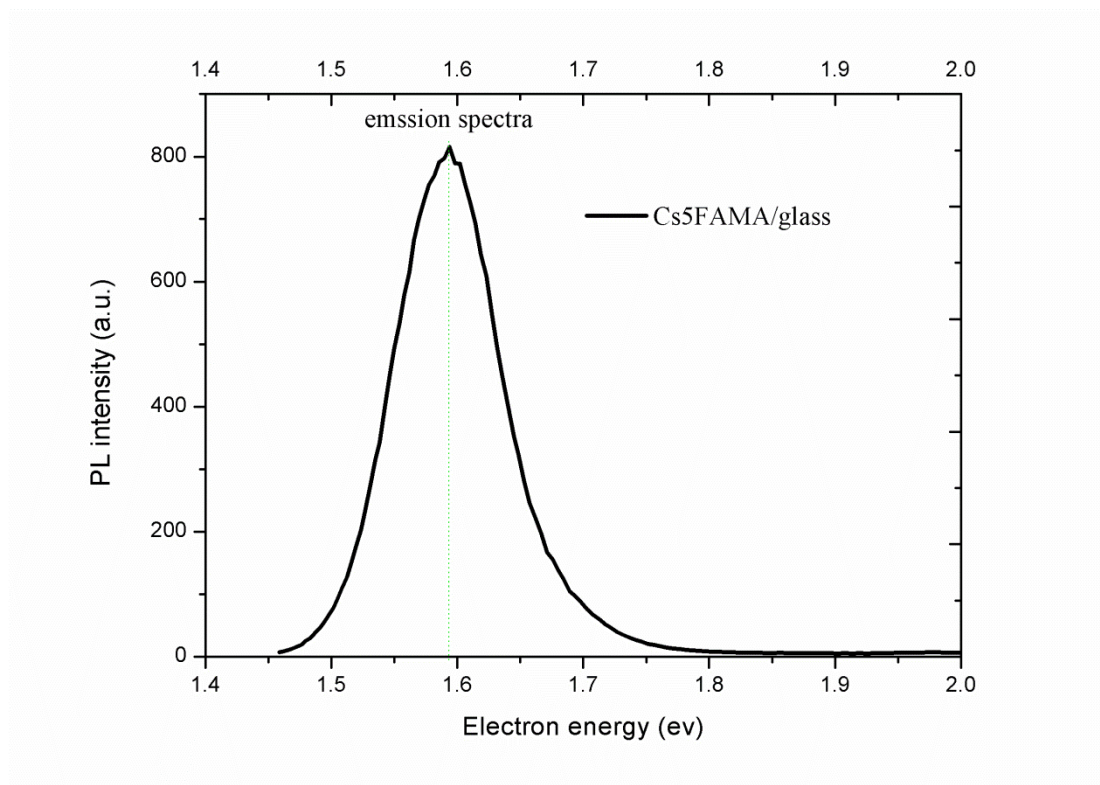


**Figure 4.4** Steady state photoluminescence spectrum of Cs5FAMA perovskite on the glass substrate. It shows that the PL emission energy is about 1.59 eV.

The PL emission mechanism diagram is proposed in Figure 4.5. For PL mechanism proposal, it will help us to deeply understand excitons dissociation and decay. (a) In Cs5FAMA, Electrons are photo-excited and transferred to the conduction band. When high energy light irradiates perovskite, electron can be transferred to higher excited-states. Internal conversion to the relative lower excited-state in conduction band takes place, and then direct recombination with holes occurs and realizes a 1.58 eV emission. When excited at the band gap energy, i.e. 1.58 ev, electron realized band gap transition to the lowest energy level in the conduction band. In the recombination process, electrons are directly transferred to the ground state in valence band and produce a 1.58 eV emission.

However, in the case of FAMA, the PL energy is 1.58 eV (see Figure 3.14 in chapter 3) that is less than the FAMA forbidden bandgap of 1.6 eV. It means that it exists a

non-radiative transition processes from low energy level excited state to some defect centers (the defects and impurity phase will be discussed below in perovskite phase analysis section), and they are located under the conduction band (CB) bottom. When electrons return to the ground-state, they firstly undergo a nonradiative transition to defect energy levels, and then they recombine with holes to produce a 1.58 eV photoluminescence emission (Figure 4.5b).

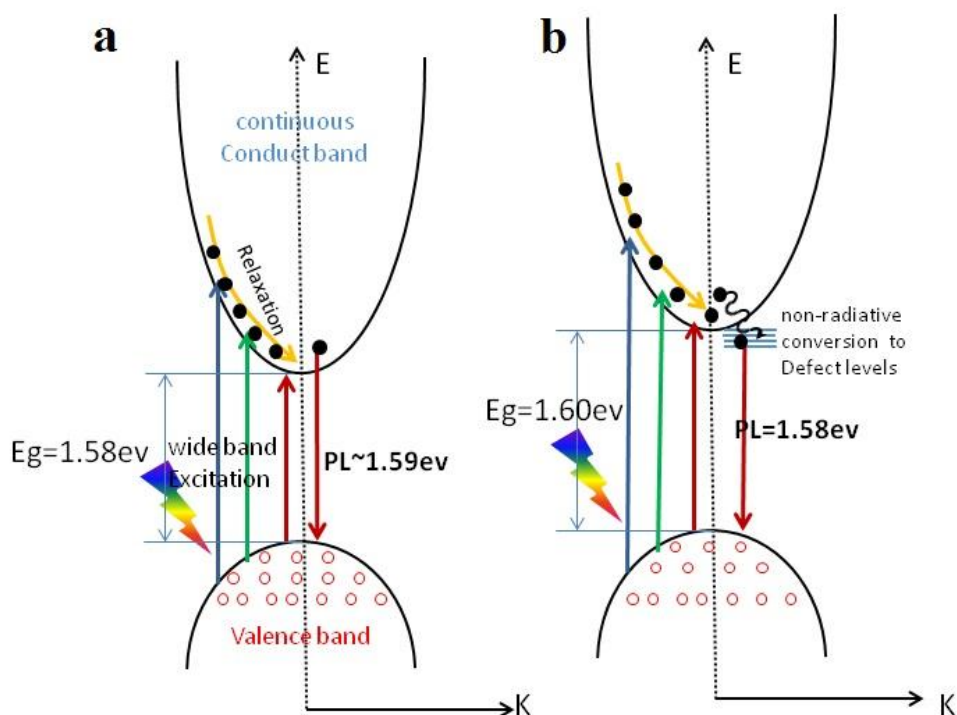


**Figure 4.5** Photoluminescence mechanism of Cs5FAMA and FAMA. (a) Proposed excitation and photoluminescence mechanism in Cs5FAMA perovskite. (b) Proposed excitation and photoluminescence mechanism in FAMA perovskite.

### 4.3.3 Discussion on the phase changes in perovskite

We have just discussed about the PL mechanism and found a non-radiative transition in the emission process of the FAMA perovskite. In general, the perovskite phase also contains other phases such as the un-reacted  $\text{PbI}_2$  phase and yellow  $\delta$ -phase perovskite, which induce some defect centers and vacancies. FAMA perovskite is prepared during

a long time and high temperature heating annealing process, which produced a series of defects especially due to organic cations decomposition and evaporation under the relative high annealing temperature [17]. Besides, Hoke et al. reported that, in the case of  $\text{MAPb}(\text{I}_x\text{Br}_{1-x})_3$  soaking with light, induces a halide segregation within the perovskite [18]. Hence, these various vacancies and defects will enable defect energy levels in the material bandgap. While excited electrons are sent into the conduction band and leave holes in the valence band, due to the electrostatic Coulomb force, the excited electrons and a holes are attracted each other to form bound state of exciton. If this exciton is bounded to the defect energy levels (i.e. defect centers), it is generally deemed that these excitons are combined with these defect centers which will produce some independent energy levels in the forbidden band of semiconductor. When electrons from these defect energy levels return to the ground state, they emit a certain irradiation energy of photoluminescence. In our FAMA case, we indeed discovered the energy loss from PL spectra energy calculation compared to the optical band edge absorption. Hence, we think that the defects exist in FAMA bulk perovskite, and the non-radiative transition happened between conduction band and independent defect energy levels. This transition process is not beneficial for either electroluminescence or photovoltaic devices. In photovoltaic devices, these bound state excitons are trapped into defect energy levels, lead to the fact that the electrons cannot be fully extracted by the electron transport layer (ETL) and cause a reduction of the efficiency of solar cells. We need to further study perovskite phase purity, phase stability and defects.

Therefore, we investigated perovskite phase change and crystallization properties for the two perovskite compositions (i.e. Cs5FAMA and FAMA) upon annealing at  $100^\circ\text{C}$ . Figure 4.6 shows the corresponding x-ray diffraction (XRD) data. The presence of Cs cations in the lattice improves the photoactive black  $\alpha$ -phase purity. We did not found the yellow  $\delta$ -phase at  $11.58^\circ$  and  $\text{PbI}_2$  phase at  $12.7^\circ$ ,  $38.8^\circ$  in Cs5FAMA perovskite XRD pattern (Figure 4.6). On the other hand, FAMA perovskite exhibits impurity

phase, such as  $\text{PbI}_2$  phase at  $12.7^\circ$  and  $38.8^\circ$ , and also non-photoactive  $\delta$ -yellow phase at  $11.58^\circ$ . This indicates that a slight energetic disorder in the perovskite matrix definitely promotes the phase purity. In addition, increasing the perovskite complexity is motivated by the need to improve the materials stability by adding more inorganic elements and increasing the entropy of mixing, which can stabilize ordinarily unstable materials (such as the “yellow,” non-photoactive phase of  $\text{FAPbI}_3$  that can be avoided adopting small amounts of the otherwise unstable  $\text{CsPbI}_3$ .[9]

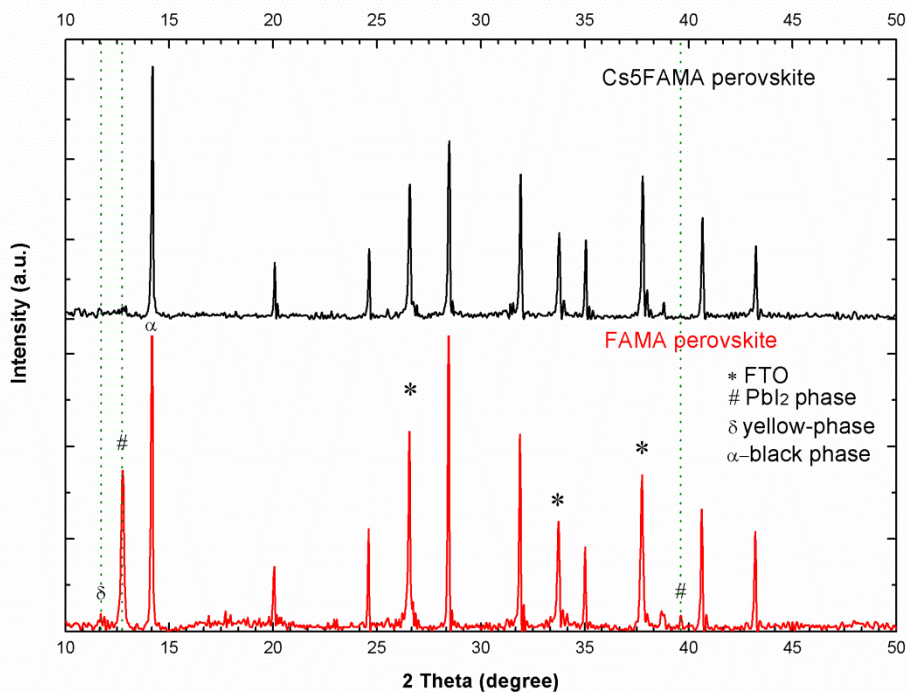


**Figure 4.6** X-ray diffraction (XRD) patterns of Cs5FAMA and FAMA perovskite layer. Here, the symbol \* is F-doped tin dioxide, the # is the un-reacted  $\text{PbI}_2$  phase,  $\delta$  marks the non-photoactive yellow phase and  $\alpha$  is the photoactive black phase.

In Figure 4.7, the scanning electron microscope (SEM) morphology image of FAMA reveals that some brighter grains are grown up from perovskite grains (grey color) boundary. However, Obviously Cs5FAMA image just displays legible and homogeneous grains. Although many scholars found separating phases and impurity phases in FAMA, we firstly rely on reflected back-scattering electron (RBSE) signal

to identify bright grains as the  $\text{PbI}_2$  phase by the split screen technology (just as we discussed and analyzed about  $\text{PbI}_2$  phase was mixed in the FAMA perovskite, detailed content in Figure 3.12). This finding is in good agreement with the XRD patterns of FAMA which exhibited clearly sharp  $\text{PbI}_2$  diffraction peaks at  $12.7^\circ$  and  $38.8^\circ$  (Figure 4.6).

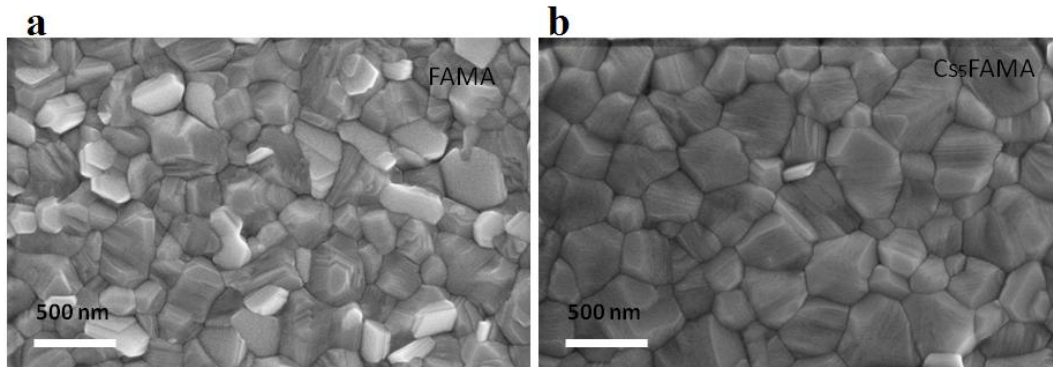


**Figure 4.7** Top view of scanning electron microscope (SEM) images of (a) FAMA and (b) Cs5FAMA perovskite layers.

#### 4.3.4 Discussion on the perovskite thermo-stability

We think that the unstable yellow phase and the  $\text{PbI}_2$  phase may induce the decomposition of the black phase of perovskite at rather high temperature operating conditions. (Above  $85^\circ\text{C}$  which, according to the international regulations, must be withstood by commercial PV products [8]) .

Therefore, we studied the perovskite aging processes and thermo-stability upon heating at  $130^\circ\text{C}$  for 3 hours. Here, it is noted that a  $130^\circ\text{C}$  heating treatment is an extremely severe challenge for hybrid perovskites and aims at realizing rapid aging experiments. Figure 4.8 clearly shows that a lot of  $\text{PbI}_2$  grains grew on FAMA surface after heating. On the other hand, the formation of  $\text{PbI}_2$  phase grains was effectively reduced in case of Cs5FAMA perovskite and the  $\text{PbI}_2$  grains presented schistose morphology on the perovskite.

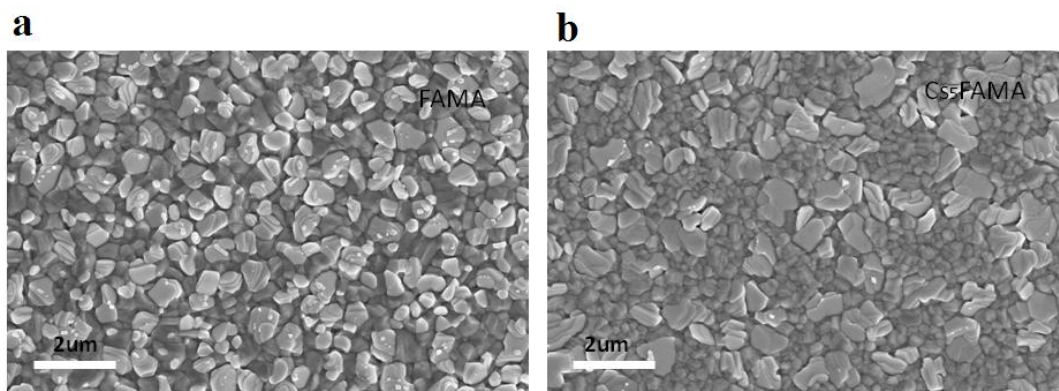


**Figure 4.8** SEM images of (a) FAMA and (b) Cs5FAMA layers after a heating treatment at 130 °C for 3 hours.

These results are consistent with both composition perovskite XRD data after aging experiment. We found that the  $\text{PbI}_2$  diffraction peaks completely dominated in the XRD patterns of FAMA perovskite in Figure 4.9. The  $\text{PbI}_2$  diffraction peak intensity strongly increases at  $12.7^\circ$  and  $38.8^\circ$  respectively (the black solid line), compared to the FAMA pattern before aging. At the same time, the photoactive black  $\alpha$ -phase was seriously reduced at  $14.7^\circ$  (the red dashed line). It indicates that the black  $\alpha$ -phase is gradually converted into  $\text{PbI}_2$  phase, which also implies that this composition is not thermo-stable.

On the other hand, the Cs-doped perovskite still obviously preserved the black  $\alpha$ -phase perovskite at  $14.7^\circ$  and its intensity was still higher than the  $\text{PbI}_2$  one which appeared with the heating treatment (Figure 4.10). These results show that Cs-doping of FAMA does not only promote the  $\alpha$ -phase purity, but also boosts the perovskite thermo-stability that could be a key advantage for persistent operation under full-sun illumination.

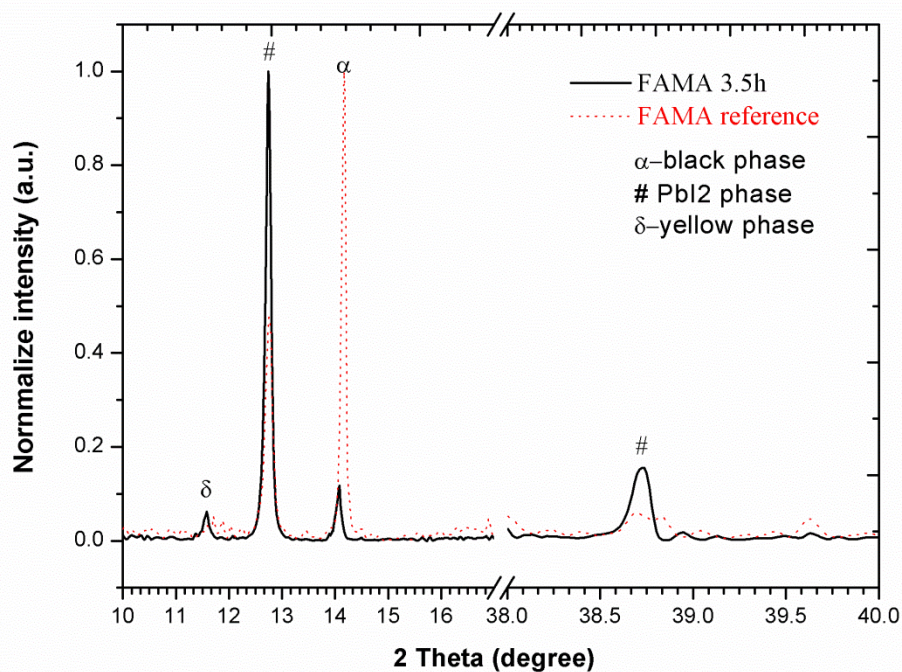


**Figure 4.9** XRD patterns of FAMA before (red dashed line), and after (black solid line) an heating treatment at 130 °C for 3h.

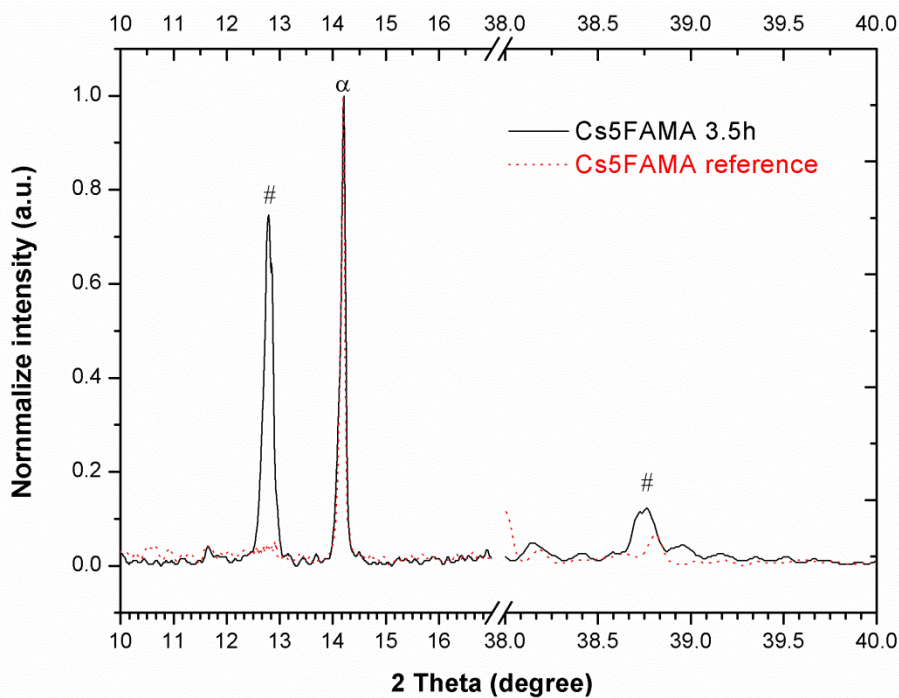


**Figure 4.10** XRD patterns of Cs5FAMA before (red dashed line), and after (black solid line) an heating treatment at 130 °C for 3h.

### 4.3.5 The charge carriers lifetimes

To further survey the charge carrier injection situation, the charge carrier dynamics were quantitatively investigated in the pristine perovskite via time-correlated single-photon counting (TCSPC) measurements. We have estimated the charge carriers lifetimes of the pristine Cs5FAMA and FAMA through two approaches: by calculating the average lifetime (Equation 4.1) and by adopting a general biexponential function to fit the decay curves (Equation 4.2). In Figure 4.11, Cs5FAMA presented an extremely long decay-time with a mean calculated value  $\tau_{\text{mean}} = 1.573 \mu\text{s}$ . Fit with the biexponential function results in  $\tau_{\text{fast}} = 115.5 \pm 1.5 \text{ ns}$  for the fast decay component and  $\tau_{\text{slow}} = 1340.8 \pm 2.3 \text{ ns}$  for the slow decay component. Both methods are in good agreement. On the other hand, FAMA exhibited a lower decay lifetime with  $\tau_{\text{mean}} = 1.089 \mu\text{s}$ , while the fitting results are  $\tau_{\text{fast}} = 59.04 \pm 0.5 \text{ ns}$  for fast decay component and  $\tau_{\text{slow}} = 1030.77 \pm 2.0 \text{ ns}$  for slow decay component. In previous reports, the fluorescence decay dynamics reflected by the slow-decay component  $\tau_{\text{slow}}$  was assigned to the free carrier recombination in the grain bulk and the fast-decay component,  $\tau_{\text{fast}}$ , to free carrier recombination at the grain surface [19]. Due to the promoted phase purity and defects decreasing in the Cs5FAMA phase, we found that the decay lifetime was prolonged in Cs5FAMA compared to FAMA. It implies that the charge carrier recombinations were suppressed in a large extent either at the surface and in the bulk of perovskite. In addition, the longer charge carrier lifetime can be related to weaker exciton effects in bandgap and high purity  $\alpha$ -phase effectively reduce recombination at defect centers, which paves the way to the achievement of very high efficiency PSCs.

The mean lifetime of decay curves formulae is:

$$\tau_{\text{average lifetime}} = \frac{\int_0^{\infty} t I(t) dt}{\int_0^{\infty} I(t) dt} \quad \text{Equation 4.1}$$

The bi-exponential decay formulae is:

$$y = A_1 * \exp(-t/\tau_1) + A_2 * \exp(-t/\tau_2) + y_0 \quad \text{Equation 4.2}$$

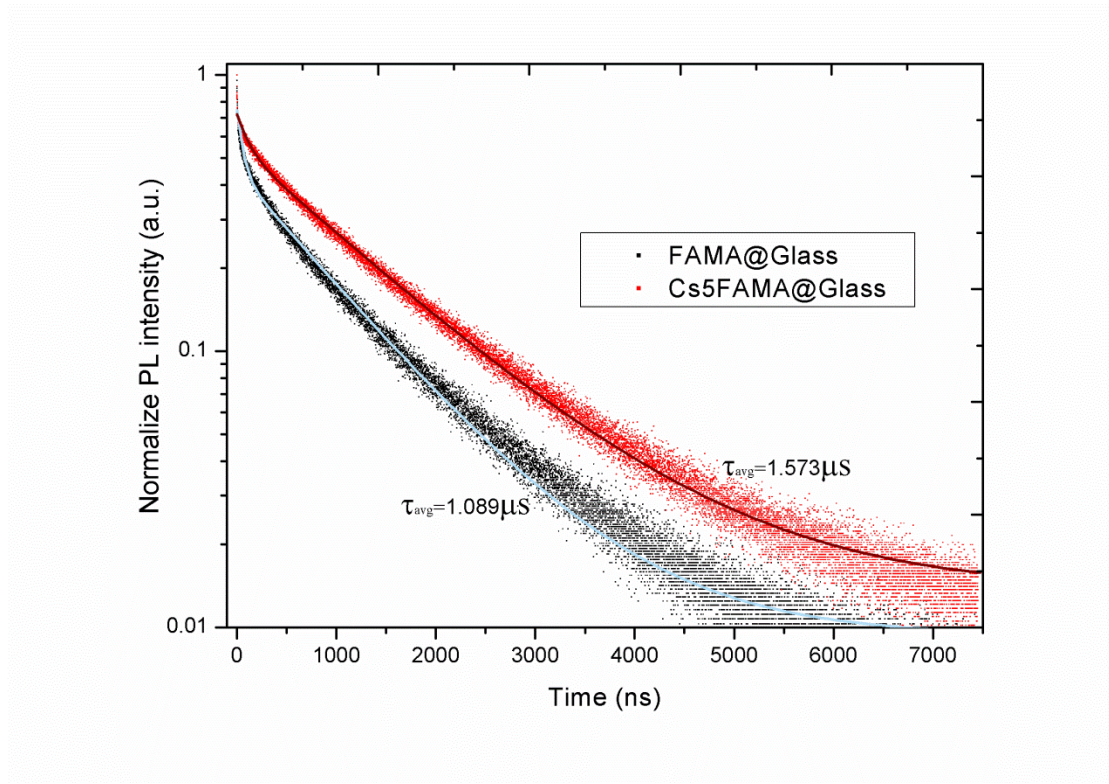


**Figure 4.11** Time-correlated single-photon counting (TCSPC) curves showing the longer lifetime of charge carriers in the pristine Cs5FAMA perovskite film, compared to FAMA.

#### 4.3.6 Design and discussion of the charge extraction layers

The combination of the perovskite and the charge extraction layers is key to get highly efficient PSCs. The charges extraction and separation have been investigated by steady-state photoluminescence spectra measurements and by time-resolved photoluminescence. We have investigated Cs5FAMA deposited on various extraction layers, namely (i) FTO/TiO<sub>2</sub>-compact layer, (ii) FTO/TiO<sub>2</sub>-compact/TiO<sub>2</sub>-mesoporous layer, and (iii) FTO/TiO<sub>2</sub>-compact/ TiO<sub>2</sub>-mesoporous/PCBM layer. The hole extraction layer was investigated on configuration of Glass/Spiro-OMeTAD.

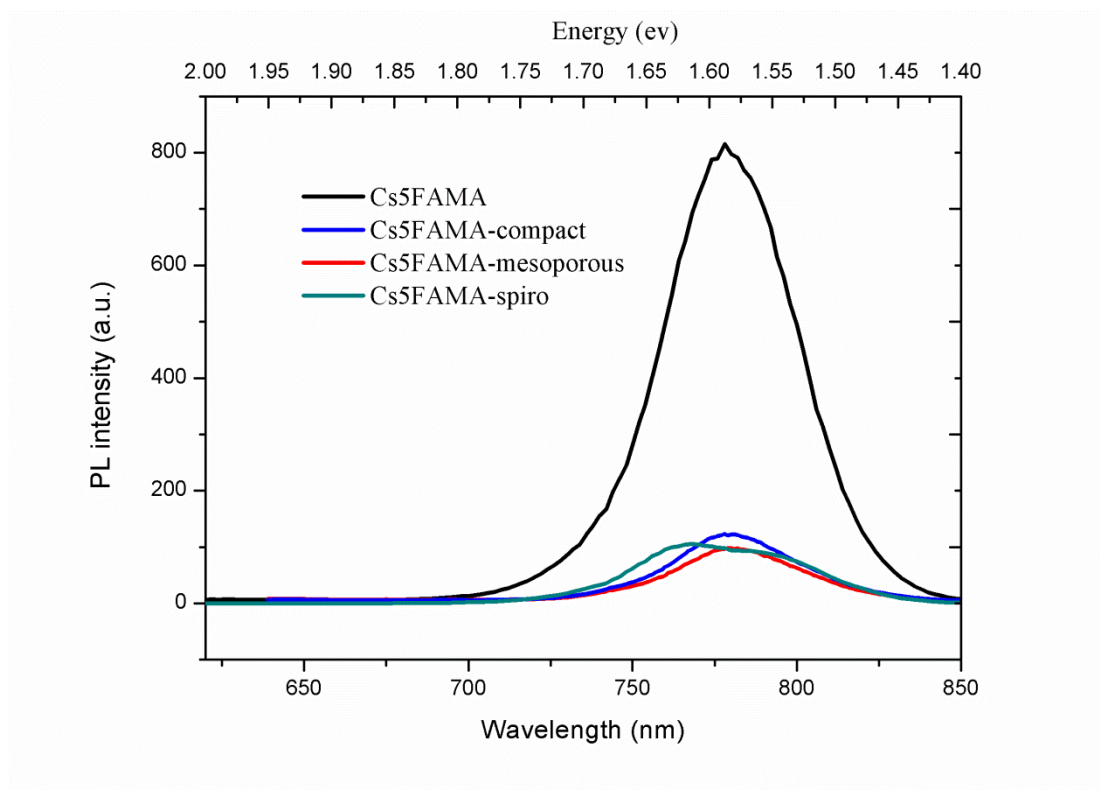


**Figure 4.12** Steady state PL spectrum of Cs5FAMA showing the emission intensity quenching on the electrons transport layer (ETL). The investigated substrates are glass, TiO<sub>2</sub> compact layer, TiO<sub>2</sub> mesoporous layer and Spiro-OMeTAD (on top of Cs5FAMA).

Firstly, the pristine Cs5FAMA deposited on glass exhibited strong PL intensity at 778 nm with a 50 nm FWHM (Figure 4.12). However, PL intensity was heavily quenched when deposited Cs5FAMA was deposited on an extraction layer, which indicated that electrons or holes were efficiently extracted from perovskite and were then injected into the corresponding extraction layers. We can also note that in the case of FAMA perovskite, the various extraction layers PL spectra followed the same quenching trend (see Figure 3.14 in Chapter 3). These observations indicate that steady state PL measurements are very precise.

The various layer combinations for Cs5FAMA have also been investigated by time-correlated single-photon counting (TCSPC). The results are consistent with the steady-state PL spectra ones (Figure 4.13). Here, the pristine Cs5FAMA exhibited a completely linear decay and good convergence character at tail decay curve.

(Generally speaking, linear slow decay indicates that the probability of excited charge carriers transfer from a certain excited state energy level to another level is very low and the good convergence character of decay curves imply that the detector detects excited charge carriers having high probability at that time range. On the contrary, other electron extraction layers displayed sharp decay component. The curve analysis shows that the FTO/TiO<sub>2</sub>-compact layer lifetime is  $\tau_{0.1} = 327$  ns, the FTO/TiO<sub>2</sub>-compact/ TiO<sub>2</sub>-mesoporous is  $\tau_{0.1} = 108$  ns and the FTO/TiO<sub>2</sub>-compact/ TiO<sub>2</sub>-mesoporous/PCBM is  $\tau_{0.1} = 80$  ns. (Here,  $\tau_{0.1}$  which is the time at which the initial photoluminescence intensity decreases by a factor 10). We can note that although FTO/TiO<sub>2</sub>-compact layer can rapidly extract electrons at the beginning, there is a changeover to a linear decay and has a convergence state in the tail of decay curve (which represents excited charge carriers has a high probability to exist in certain excited energy levels. On the contrary, the divergence state represents low rate happening). It indicates that electrons are difficult to completely and continuously inject into FTO/TiO<sub>2</sub>-compact (injected flux not enough). This fairly explains why TiO<sub>2</sub>/planar configuration cells usually produce poor efficiency.[20] On the contrast, the FTO/ TiO<sub>2</sub>-compact/TiO<sub>2</sub>-mesoporous and the FTO/TiO<sub>2</sub>-compact/TiO<sub>2</sub>-mesoporous/PCBM samples present a different shape (Figure 4.13). In this case, electron extraction layer display a rapid decay process and divergent character at the end of decay curves. It shows that these structures can efficiently extract the electrons from Cs5FAMA perovskite. We think that the 3 dimensionality mesoporous layer realizes a more specific interface which improves the contact area with perovskite. It increases the electron injection flux compared to the planar structure.

In the case of Spiro-OMeTAD contact, the charge (hole) injection is even much faster. The configuration of Glass/Spiro-OMeTAD realized an extraction time as low as  $\tau_{0.1} = 7.6$  ns. Therefore, the injection speed for holes is more than two orders of magnitude higher that for electrons. The configuration of FTO/TiO<sub>2</sub>-compact/ TiO<sub>2</sub>-mesoporous/PCBM produces the best electron injection ability. It is explained based on the energy diagram presented in Figure 4.14. The PCBM layer introduces an

energy level located in-between that of the conduction band of perovskite and of  $\text{TiO}_2$ . Moreover, PCBM molecules could passivate  $\text{TiO}_2$  surface defects. Therefore, the presence of this layer facilitates the electron injection and its transfer towards the  $\text{TiO}_2$  layer. The corresponding photovoltaic device's parameters will be discussed later.

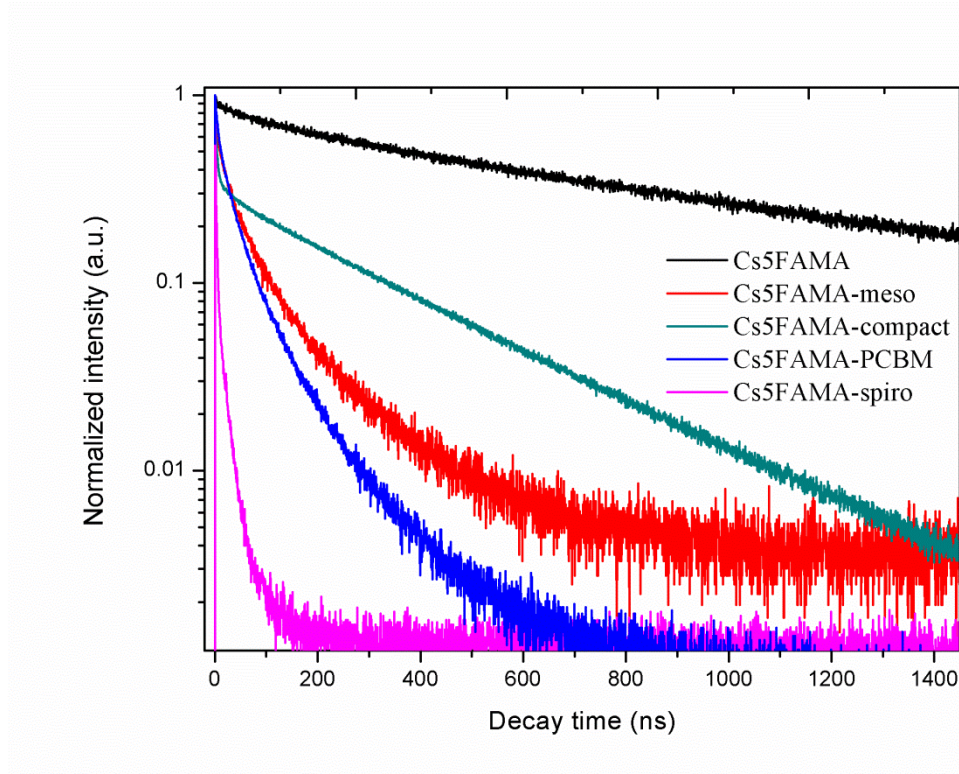


**Figure 4.13** Time-correlated single-photon counting (TCSPC) curves of pristine Cs5FAMA perovskite deposited on glass and combined with various electron and hole transport layers: FTO/ $\text{TiO}_2$ -compact layer, FTO/ $\text{TiO}_2$ -compact/ $\text{TiO}_2$ -mesoporous layer, FTO/ $\text{TiO}_2$ -compact/ $\text{TiO}_2$ -mesoporous/PCBM layer and Spiro-OMeTAD.

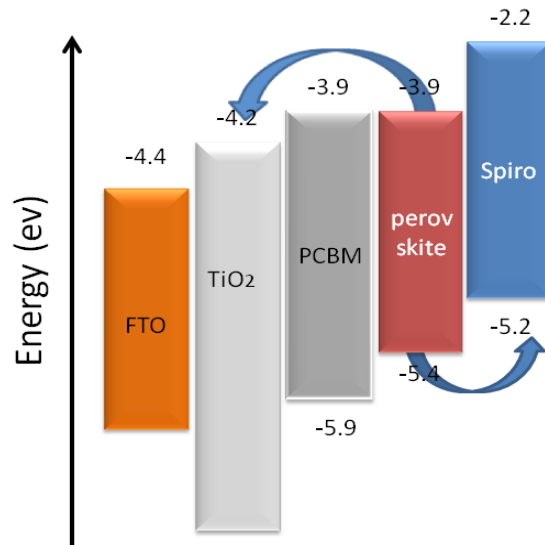


**Figure 4.14** Energy level diagram of various layers in perovskite solar cell.

### 4.3.7 The properties of Cs5FAMA perovskite solar cells

Perovskite solar cells have been fabricated with the various following structures:

- ( i ) FTO/TiO<sub>2</sub>-compact/TiO<sub>2</sub>-mesoporous/FAMAPEROVSKITE/Spiro-OMeTAD/Au (for reference),
- ( ii ) FTO/TiO<sub>2</sub>-compact/mesoporous/Cs5FAMAPEROVSKITE/Spiro-OMeTAD/Au,
- ( iii ) FTO/TiO<sub>2</sub>-compact/mesoporous/PCBM/Cs5FAMA/Spiro-OMeTAD/Au.

We have investigated the photovoltaic (PV) properties of these devices. The photovoltaic (PV) metrics are collected from current-voltage *J-V* curves of the champion Cs5FAMA devices in Figure 4.15, in which are an open circuit voltage  $V_{oc} = 1104$  mV, a short circuit current  $J_{sc} = 24.19$  mA/cm<sup>2</sup>, and a fill factor FF = 77.4%, resulting in a power conversion efficiency PCE of 20.67%. The potential scan rate was 25 mV/s. To confirm the stabilized PCE outputting (and eliminate the scanning direction and speed effects), we tracked the maxima power point (MPP) under standard AM 1.5G solar illumination. Inset of Figure 4.15 shows the MPP tracking for 60s monitored at  $V_{max} = 944$  mV. The stabilized current output was 21.86 mA/cm<sup>2</sup>,

yielding a stabilized PCE of 20.64%. This result is consistent with the  $J$ - $V$  measurement, indicating that our  $J$ - $V$  measuring parameters are reliable. Generally speaking, the long-time tracking MPP results could completely present the reality device operating status.

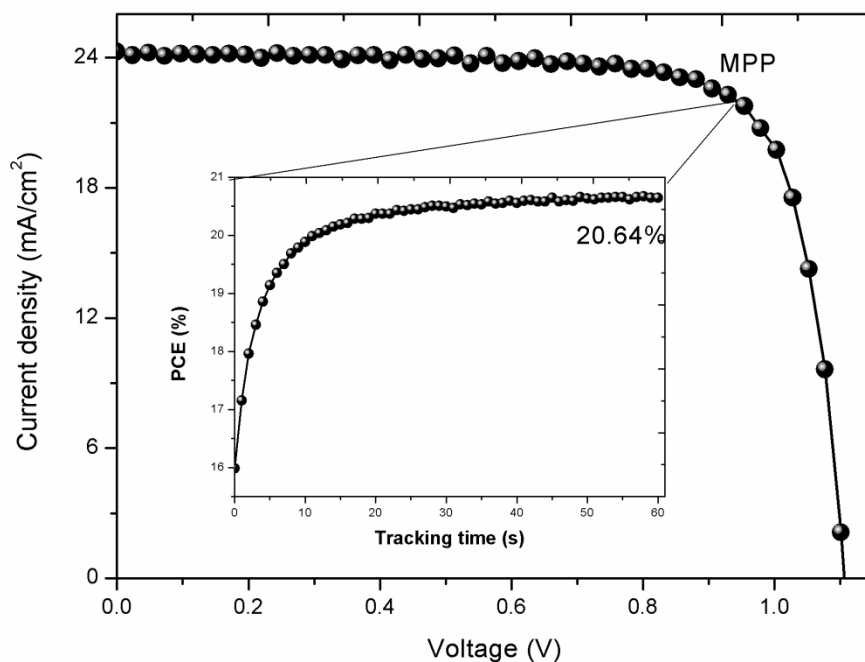


**Figure 4.15** Current density/voltage ( $J$ - $V$ ) curve of the best Cs5FAMA solar cell performing at 20.67% ( $V_{oc} = 1104$  mV,  $J_{sc} = 24.19$  mA/cm<sup>2</sup>, and fill factor 77.4%), measured at scan rate of 25 mV/s. The inset shows the maximum power point (MPP) tracking for 60s monitored at  $V_{max} = 944$  mV and finally producing 21.86 mA/cm<sup>2</sup>, yielding a stabilized efficiency of 20.64%.

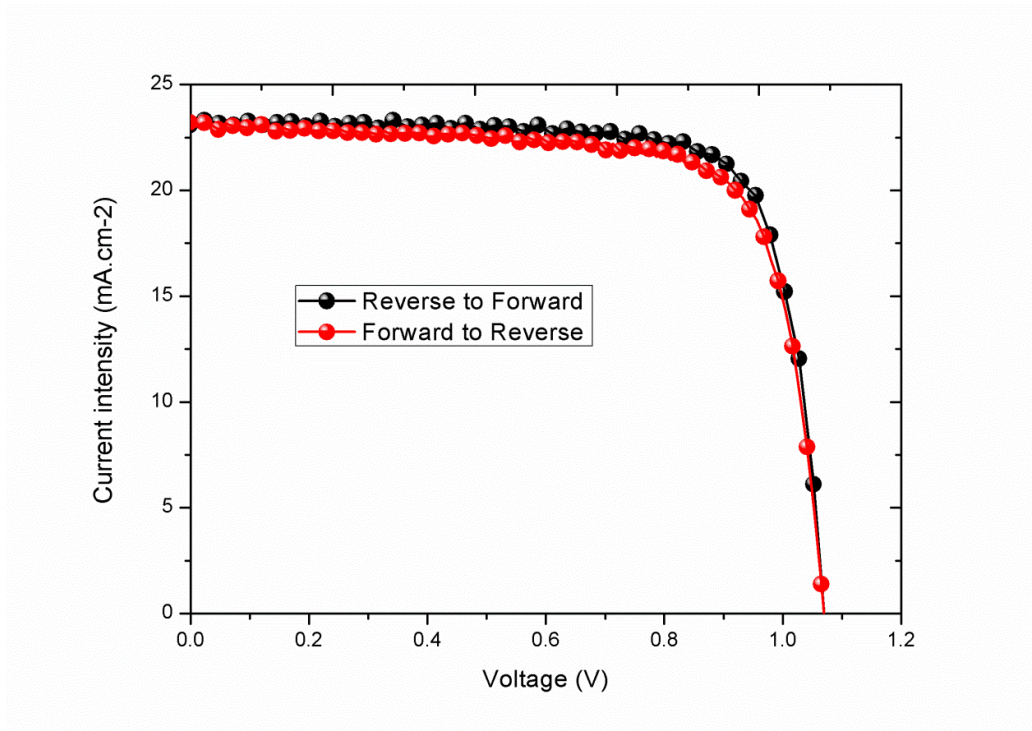


**Figure 4.16** A typical  $J$ - $V$  curves of Cs5FAMA device measured in the forward and reverse potential scan directions (potential scan rate at 25 mV/s).

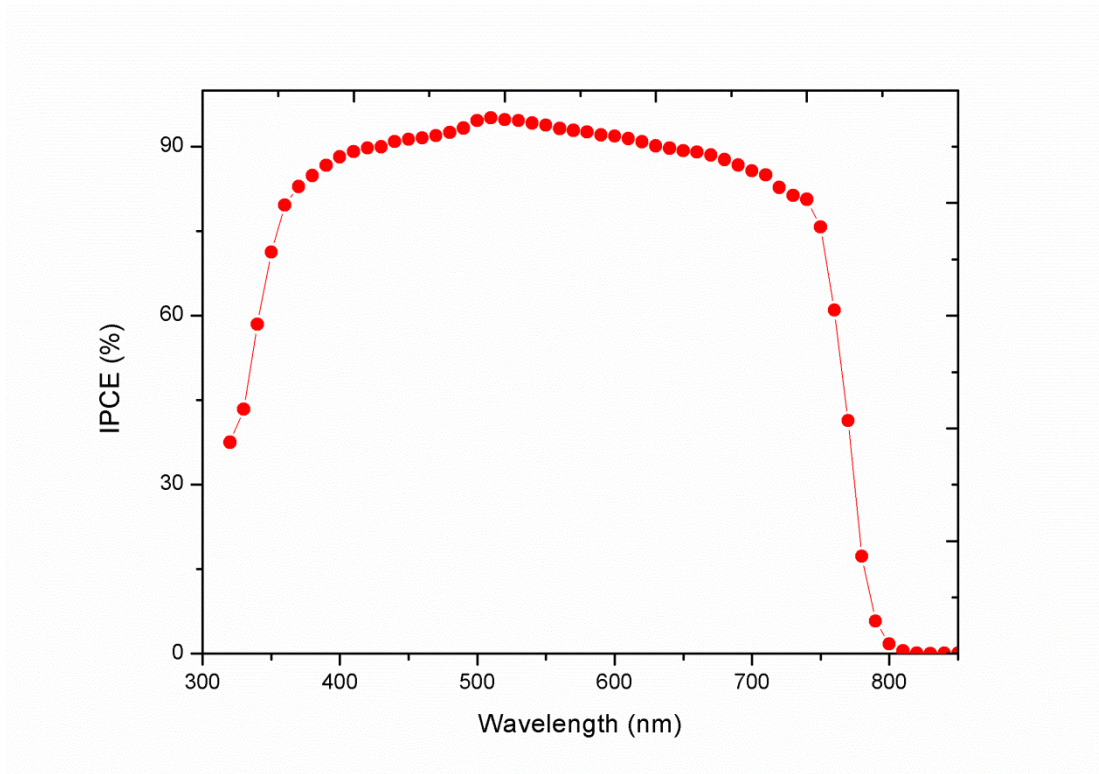


**Figure 4.17** External quantum efficiency of the best performing Cs5FAMA solar cell, the integrated short circuit current density is  $23.6 \text{ mA/cm}^2$ .

Perovskite solar cells are reported to present a hysteresis between the forward and the reverse scans of the  $J$ - $V$  curves. The amplitude of this hysteresis depends on the system, on the selective contacts and on the quality of the interfaces. It is generally admitted that hysteresis is related to the accumulation of mobile ions (and ion vacancies) at the interfaces near the contacts due to ion migration under an electric field. It alters the band structure at the interface and modulates the barrier heights for electron/hole collection. Some authors have suggested that defects and vacancies seriously affect the transport of free charges, especially under the short circuit condition, the free charges will be removed from defects states and lead to more or less current changes [21, 22]. Besides, the ionic polarization in devices might be attributed to methylammonium cation migration under the light excitation, and ferroelectric effects [23]. Because of various perovskite compositions, configuration of device, and different experiment technologies, it is difficult to get a harmonized view of the phenomenon. However, we believe that a good thermo-stability, a high crystallization, and less defect states in the perovskite absorber are important to get an efficient, stable, and reproducible photovoltaic device.

In our case, we investigated hysteresis effect in Cs5FAMA device by measuring the cells both under reverse and forward voltage scan directions. In Figure 4.16, the  $J$ - $V$  curves of Cs5FAMA device are almost hysteresis-free. Generally speaking, the persistent power outputting is traced at the maxima power point that can completely overcome to estimate uncorrected value of efficiency which is affected by hysteresis effect. In addition, the integrated photocurrent densities obtained from the external quantum efficiency (EQE) spectra of the Cs5FAMA device closely agrees with the  $J_{sc}$  determined from the  $J$ - $V$  curves of the solar device.

To demonstrate that Cs5FAMA device properties are better than the FAMA ones, we remind here the best performing FAMA-based device metrics: a  $V_{oc} = 1176$  mV, a  $J_{sc} = 23.06$  mA/cm<sup>2</sup>, and a FF = 78.2%, resulting in a PCE of 20.11% taken a scan rate at 25mV/s (in Chapter 3).

Moreover, for demonstrating that Cs5FAMA PCEs are more efficient and reproducible than FAMA devices, the detailed inventory of photovoltaic metrics have

been averaged for about the 30 FAMA and 40 Cs5FAMA independent devices. Figure 4.18 shows the statistical distribution of photovoltaic metrics. Cs5FAMA devices showed an average value of  $V_{oc} = 1106$  mV, a  $J_{sc} = 23.84$  mA/cm<sup>2</sup>, a FF = 76%, and having a PCE of 20.2 %. FAMA devices demonstrate an average value of  $V_{oc} = 1104$  mV,  $J_{sc} = 23.16$  mA/cm<sup>2</sup>, and a FF = 78%, and having a PCE of 19.8% in FAMA devices. In comparison, the Cs5FAMA PCEs were more reproducible and provided a higher efficiency than in FAMA devices. This is in good agreement with the analysis of perovskite detailed above which showed a high phase purity, less defects, and reduced non-radiation loss for Cs5FAMA.

Besides, FAMA bandgap is 1.60 eV, while it is 1.58 eV for Cs5FAMA. It is noticeable that the bandgap slight red shift may have some impact on short circuit current  $J_{sc}$  because a wider light wavelength range can be harvested by the absorber. Therefore, the Cs5FAMA device exhibited higher  $J_{sc}$  values than FAMA (the average  $J_{sc}$  value is 23.84 mA/cm<sup>2</sup> compared to 23.16 mA/cm<sup>2</sup>). Moreover, it is interesting that the open circuit voltage  $V_{oc}$  values are not seriously affected by the bandgap red shift (although the champion of FAMA device is slightly higher than that of the Cs5FAMA device), because of increasing non-radiative recombination loss in defects centers in FAMA perovskite that lead to  $V_{oc}$  cannot reach the conventional true value of open circuit voltage.

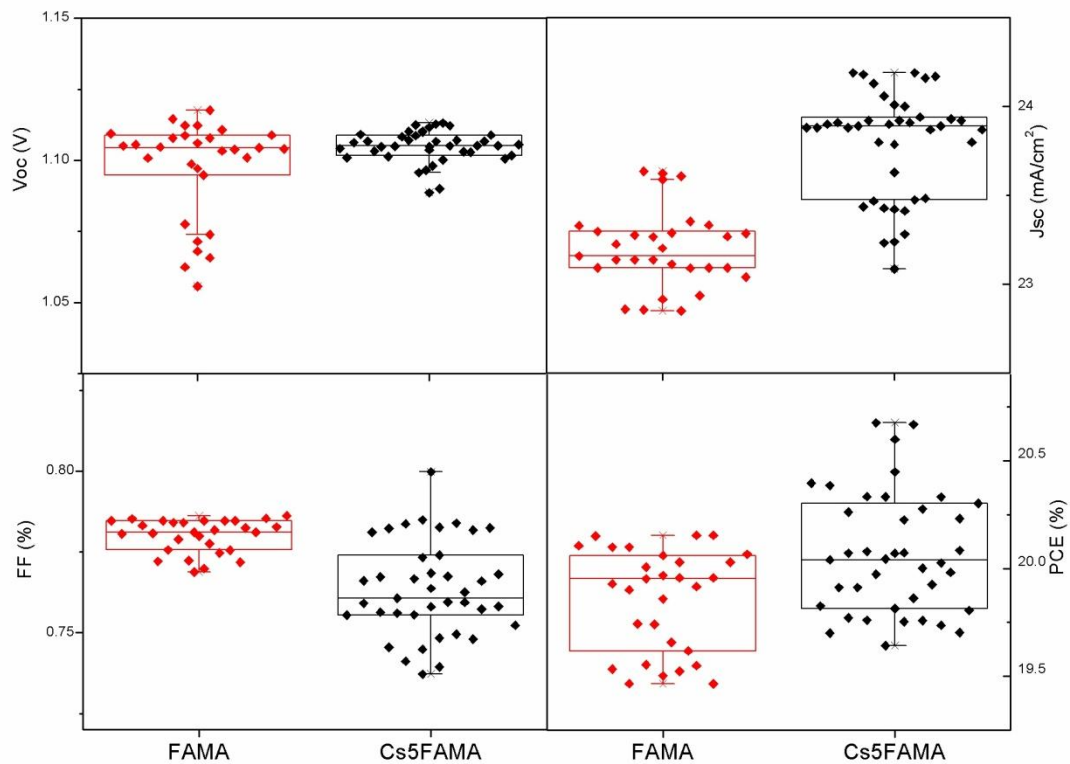


**Figure 4.18**  $J$ - $V$  metrics for 30 devices of FAMA and 40 devices of Cs5FAMA, including  $V_{oc}$ , open circuit voltage;  $J_{sc}$ , short circuit current; FF, fill factor; PCE, power conversion efficiency.

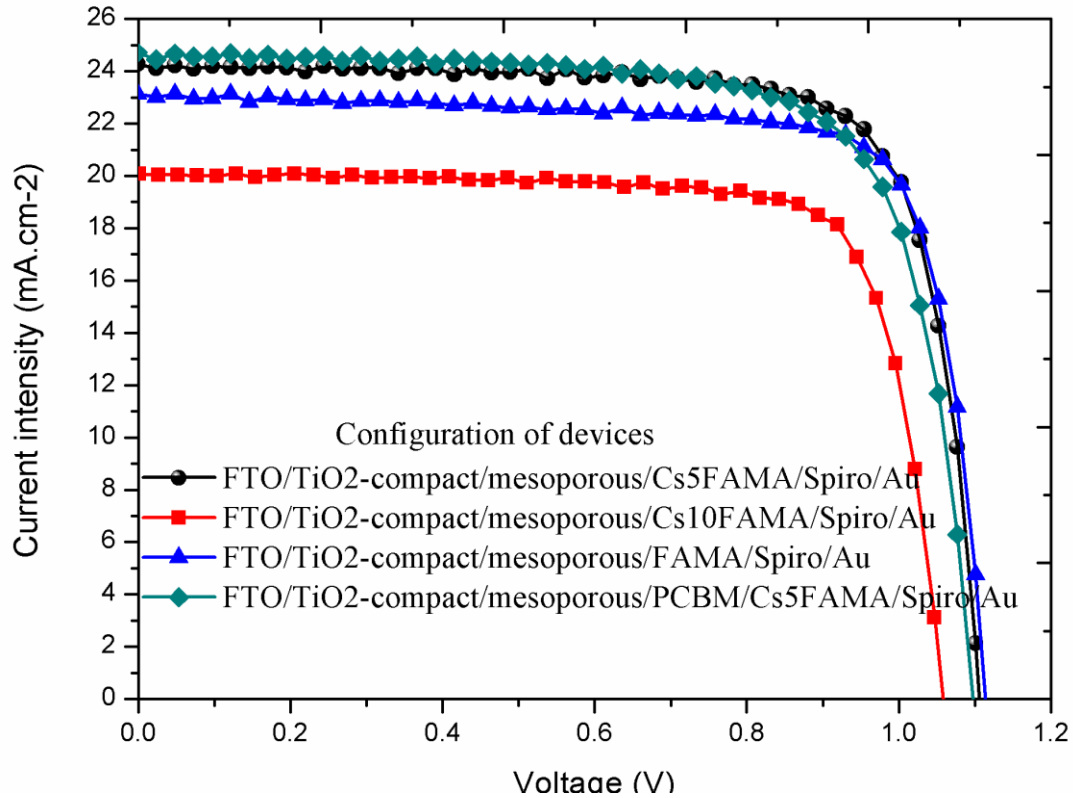


**Figure 4.19** *J-V* curves for devices with various perovskites in the different configuration of perovskite solar cells measured with a reverse scan rate at 25mV/s.

**Table 4. 1** *J-V* curve parameters of the best solar cells presented in Figure 4.18.

Configuration/Perovskite	$V_{oc}$ (mV)	$J_{sc}$ (mA/cm <sup>2</sup> )	Fill factor (%)	PCE (%)
Cs5FAMA	1104	24.19	77.4	20.67
Cs10FAMA	1056	21.55	78.4	17.87
FAMA	1176	23.06	78.2	20.11
PCBM/Cs5FAMA	1096	24.61	73.9	19.96

We have shown above that adopting the FTO/TiO<sub>2</sub>-compact/TiO<sub>2</sub>-mesoporous/PCBM layer for electrons extraction layer can increase the extraction speed. A consequence was a TCSPC curve with a rapidly decay trend  $\tau_{0.1} = 80$  ns, while using the normal electron extraction layer (i.e. TiO<sub>2</sub>-compact/ TiO<sub>2</sub>-mesoporous configuration), it was  $\tau_{0.1} = 108$  ns.

According to *J-V* measurements, the photovoltaic *J-V* curves were recorded in Figure

4.19 and photovoltaic (PV) metrics in the table 4.1, where a  $V_{oc} = 1096$  mV,  $J_{sc} = 24.61$  mA/cm<sup>2</sup>, and a FF = 73.9%, resulting in a PCE of 19.96%. We noted that here the  $J_{sc}$  value is higher than TiO<sub>2</sub>-compact/ TiO<sub>2</sub>-mesoporous configuration. It indicates the TiO<sub>2</sub>-compact/TiO<sub>2</sub>-mesoporous/PCBM electrons extraction layer indeed could effectively extract electrons and that the electrons were efficiently injected. This leads to improve  $J_{sc}$  of the device.

In addition, we also investigated the high concentration Cs10 doped FAMA perovskite. As was shown in Figure 4.19, the photovoltaic metrics are decreased compared to Cs5FAMA device, with a  $V_{oc} = 1056$  mV, a  $J_{sc} = 21.55$  mA/cm<sup>2</sup>, and a FF = 78.4%, resulting in a PCE of 17.87%. SEM images of Cs10FAMA perovskite displayed small crystal grains compared with Cs5FAMA under the same amplification (Figure 4.20). The relative low performance might be due to high charge carriers recombinations at grains boundaries, because the small size grains are accompanied by more grains boundaries.

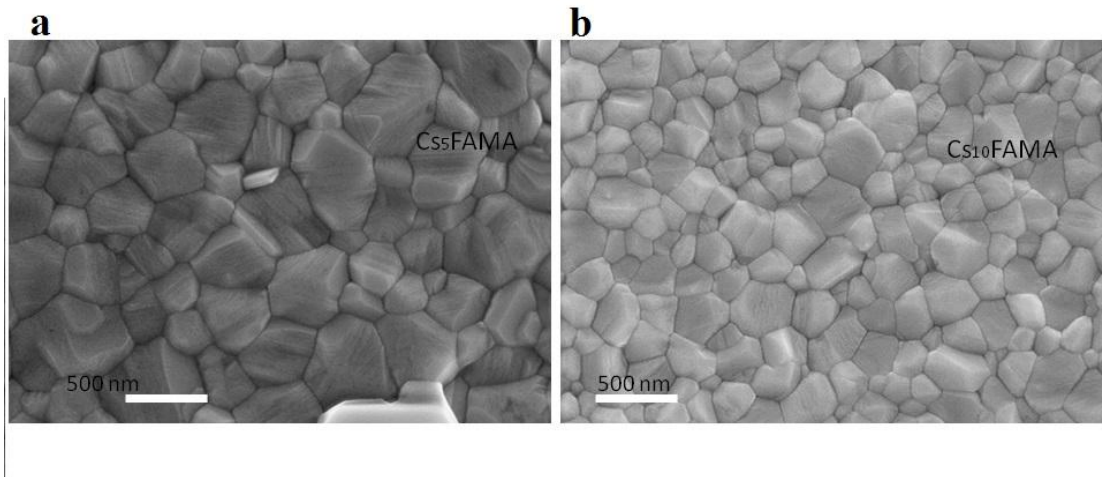


**Figure 4.20** Top views of scanning electron microscopy (SEM) images of (a) Cs5FAMA and (b) Cs10FAMA perovskite layers. The scale bar is 500 nm.

A preliminary study of the Cs5FAMA cell stability was carried out. Figure 4.21 shows that the unencapsulated Cs5FAMA photovoltaic device output persistent current was 21.83 mA/cm<sup>2</sup>. It produced a steady-state PCE of 20.6% during 5 minutes under room ambient conditions without any inert atmosphere protection. The stable outputting

state indicates that the Cs5FAMA device is stable and that high efficiency is reached under closely real working conditions via tracking MMP experiment for 5 min.

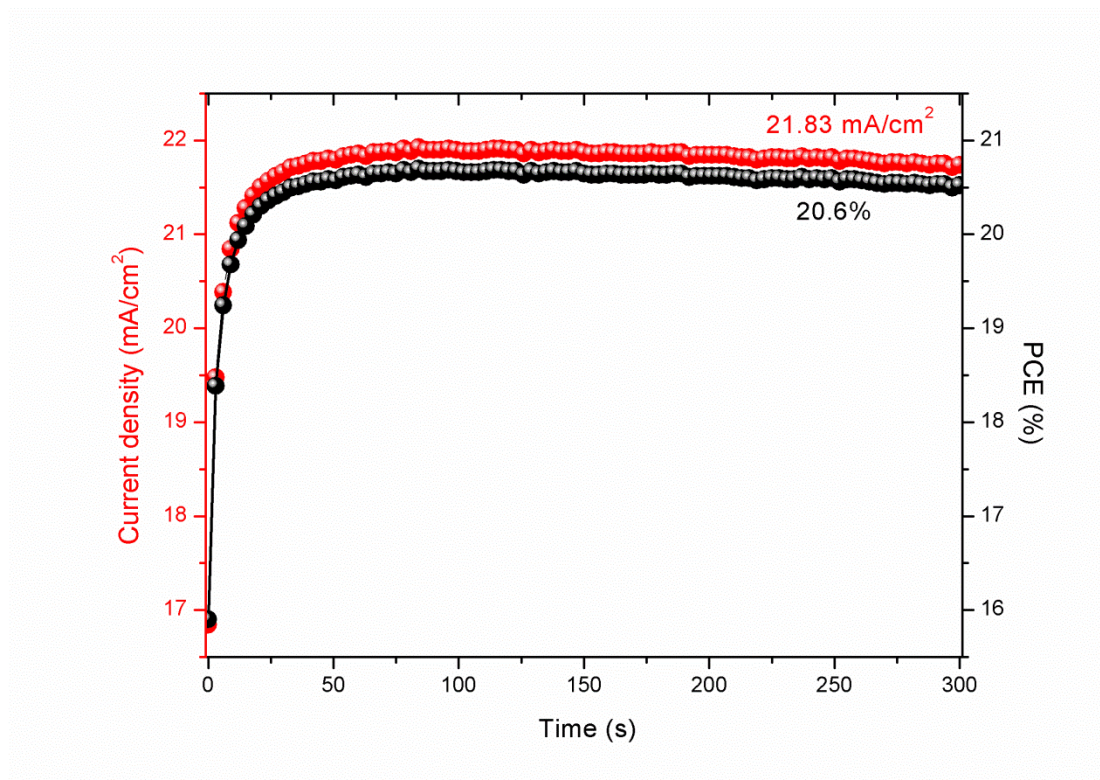


**Figure 4.21** MPP tracking for 5 minutes of unencapsulated Cs5FAMA device placed under ambient conditions, yielding a stabilized current density of 21.83 mA/cm<sup>2</sup> and a stabilized efficiency of 20.6 %.

## 4.4 Conclusion

In this chapter, we have thoroughly investigated the effect of adding 5% of Cs cation into dual cations FAMA perovskite. Our analysis of the early period nucleation kinetics before heating treatment has shown that the addition of Cs favors heterogeneous nucleation compared to FAMA. This dramatically distinct kinetics changing has indicated that the system Gibbs free energy was decreased and that the spontaneous nucleation reaction was promoted in Cs5FAMA precursor solution. The XRD patterns comparison between Cs5FAMA and FAMA perovskite showed that Cs cations introduction into the perovskite matrix reduces the possibility of phase

segregation and promotes the photoactive black  $\alpha$ -phase purity. At the same time, this higher phase purity further protects the perovskite from phase decomposition under high temperature operating conditions. It is a key element to make sure that solar cells can be operated in a stable manner under the international standard at 85 °Celsius. As we know, the first step of the photoluminescence mechanism is light absorption which produces the excited charge carriers. There have been few studies on the photoluminescence mechanism in hybrid perovskites. According to our analysis of the absorption and fluorescence spectrum of Cs5FAMA, and their comparison with the FAMA ones, we propose a different photoluminescence mechanism for the two perovskites. Due to the presence of defect states and the relatively large binding energy at the defect centers in FAMA perovskite, some excitons were bounded at defect centers (like some point defect and vacancies) which is introduced by impurity phases in FAMA. It is in good agreement with the decay lifetime which was different for the two different compositions. The higher crystal quality of Cs5FAMA gave rise to a longer decay lifetime. In addition, we designed the electron extraction layer of TiO<sub>2</sub>-compact/TiO<sub>2</sub>-mesoporous/PCBM that possesses the most rapid electron injection speed and then exhibited the highest  $J_{sc}$  (24.61 mA/cm<sup>2</sup>) attained in the configuration of FTO/TiO<sub>2</sub>-compact/TiO<sub>2</sub>-mesoporous/PCBM/Cs5FAMA/Spiro/Au PSCs. The comparison of the charge extraction speed between ETL and HTL, shows that the electron transport material and configuration limit the photovoltaic device performance and that it was important to optimize this extraction layer.

Finally, we achieved high efficiency, reproducibility, and stability with Cs5FAMA perovskite solar cells. These photovoltaic devices exhibited at best an open circuit voltage  $V_{oc} = 1104$  mV, a short circuit current  $J_{sc} = 24.19$  mA/cm<sup>2</sup>, and a fill factor  $FF = 77.4\%$ , resulting in a power conversion efficiency PCE of 20.67%. The average photovoltaic metrics were a  $V_{oc} = 1106$  mV, a  $J_{sc} = 23.84$  mA/cm<sup>2</sup>, a  $FF = 76\%$ , and having a PCE of 20.2 % for 40 pieces of independent devices.

## References

1. Yi C, Luo J, Meloni S, Boziki A, Ashari-Astani N, Grätzel C, Zakeeruddin SM, Rühlisberger U, Grätzel M. Entropic stabilization of mixed A-cation ABX<sub>3</sub> metal halide perovskites for high performance perovskite solar cells. *Energy & Environmental Science*. 2016;9:656-62.
2. Li Z, Yang M, Park J-S, Wei S-H, Berry JJ, Zhu K. Stabilizing perovskite structures by tuning tolerance factor: formation of formamidinium and cesium lead iodide solid-state alloys. *Chemistry of Materials*. 2015;28:284-92.
3. Choi H, Jeong J, Kim H-B, Kim S, Walker B, Kim G-H, Kim JY. Cesium-doped methylammonium lead iodide perovskite light absorber for hybrid solar cells. *Nano Energy*. 2014;7:80-5.
4. Lee JW, Kim DH, Kim HS, Seo SW, Cho SM, Park NG. Formamidinium and cesium hybridization for photo-and moisture-stable perovskite solar cell. *Advanced Energy Materials*. 2015;5.
5. Saliba M, Matsui T, Seo J-Y, Domanski K, Correa-Baena J-P, Nazeeruddin MK, Zakeeruddin SM, Tress W, Abate A, Hagfeldt A. Cesium-containing triple cation perovskite solar cells: improved stability, reproducibility and high efficiency. *Energy & Environmental Science*. 2016;9:1989-97.
6. Raga SR, Ono LK, Qi Y. Rapid perovskite formation by CH<sub>3</sub>NH<sub>2</sub> gas-induced intercalation and reaction of PbI<sub>2</sub>. *Journal of Materials Chemistry A*. 2016;4:2494-500.
7. Bu T, Liu X, Zhou Y, Yi J, Huang X, Luo L, Xiao J, Ku Z, Peng Y, Huang F. A novel quadruple-cation absorber for universal hysteresis elimination for high efficiency and stable perovskite solar cells. *Energy & Environmental Science*. 2017;10:2509-15.
8. McMeekin DP, Sadoughi G, Rehman W, Eperon GE, Saliba M, Hörantner MT, Haghighirad A, Sakai N, Korte L, Rech B. A mixed-cation lead mixed-halide perovskite absorber for tandem solar cells. *Science*. 2016;351:151-5.
9. Saliba M, Matsui T, Domanski K, Seo J-Y, Ummadisingu A, Zakeeruddin SM,

Correa-Baena J-P, Tress WR, Abate A, Hagfeldt A. Incorporation of rubidium cations into perovskite solar cells improves photovoltaic performance. *Science*. 2016;354:206-9.

10. Jeon NJ, Noh JH, Yang WS, Kim YC, Ryu S, Seo J, Seok SI. Compositional engineering of perovskite materials for high-performance solar cells. *Nature*. 2015;517:476.

11. Paek S, Schouwink P, Athanasopoulou EN, Cho K, Grancini G, Lee Y, Zhang Y, Stellacci F, Nazeeruddin MK, Gao P. From Nano-to Micrometer Scale: The Role of Antisolvent Treatment on High Performance Perovskite Solar Cells. *Chemistry of Materials*. 2017;29:3490-8.

12. Arora N, Dar MI, Hinderhofer A, Pellet N, Schreiber F, Zakeeruddin SM, Grätzel M. Perovskite solar cells with CuSCN hole extraction layers yield stabilized efficiencies greater than 20%. *Science*. 2017:eaam5655.

13. Bi D, Tress W, Dar MI, Gao P, Luo J, Renevier C, Schenk K, Abate A, Giordano F, Baena J-PC. Efficient luminescent solar cells based on tailored mixed-cation perovskites. *Science advances*. 2016;2:e1501170.

14. Bi D, Luo J, Zhang F, Magrez A, Athanasopoulou EN, Hagfeldt A, Grätzel M. Morphology Engineering: A Route to Highly Reproducible and High Efficiency Perovskite Solar Cells. *ChemSusChem*. 2017;10:1624-30.

15. Yang M, Li Z, Reese MO, Reid OG, Kim DH, Siol S, Klein TR, Yan Y, Berry JJ, van Hest MF. Perovskite ink with wide processing window for scalable high-efficiency solar cells. *Nature Energy*. 2017;2:17038.

16. Kong L, Liu G, Gong J, Hu Q, Schaller RD, Dera P, Zhang D, Liu Z, Yang W, Zhu K. Simultaneous band-gap narrowing and carrier-lifetime prolongation of organic–inorganic trihalide perovskites. *Proceedings of the National Academy of Sciences*. 2016;113:8910-5.

17. Zhou Z, Wang Z, Zhou Y, Pang S, Wang D, Xu H, Liu Z, Padture NP, Cui G. Methylamine-Gas-Induced Defect-Healing Behavior of CH<sub>3</sub>NH<sub>3</sub>PbI<sub>3</sub> Thin Films for Perovskite Solar Cells. *Angewandte Chemie International Edition*. 2015;54:9705-9.

18. Hoke ET, Slotcavage DJ, Dohner ER, Bowring AR, Karunadasa HI, McGehee

MD. Reversible photo-induced trap formation in mixed-halide hybrid perovskites for photovoltaics. *Chemical Science*. 2015;6:613-7.

19. Shi D, Adinolfi V, Comin R, Yuan M, Alarousu E, Buin A, Chen Y, Hoogland S, Rothenberger A, Katsiev K. Low trap-state density and long carrier diffusion in organolead trihalide perovskite single crystals. *Science*. 2015;347:519-22.

20. Jeon NJ, Noh JH, Kim YC, Yang WS, Ryu S, Seok SI. Solvent engineering for high-performance inorganic–organic hybrid perovskite solar cells. *Nature materials*. 2014;13:897.

21. Street R, Ready S, Van Schuylenbergh K, Ho J, Boyce J, Nylén P, Shah K, Melekhov L, Hermon H. Comparison of PbI<sub>2</sub> and HgI<sub>2</sub> for direct detection active matrix x-ray image sensors. *Journal of Applied Physics*. 2002;91:3345-55.

22. Snaith HJ, Abate A, Ball JM, Eperon GE, Leijtens T, Noel NK, Stranks SD, Wang JT-W, Wojciechowski K, Zhang W. Anomalous hysteresis in perovskite solar cells. *The journal of physical chemistry letters*. 2014;5:1511-5.

23. Frost JM, Butler KT, Walsh A. Molecular ferroelectric contributions to anomalous hysteresis in hybrid perovskite solar cells. *Apl Materials*. 2014;2:081506.

## General conclusion and perspectives

Perovskite solar cells are attracting more and more attention in the photovoltaic device field due to a continuous increase of power conversion efficiency within a few years. These rapid progresses are the results of the intensive studying and research activities in the perovskite scientific ‘hot point’ field. They are all the more remarkable that the single-junction silicon solar cells have spent almost 40 years for achieving high efficiencies above 20%. The development of researches on the perovskite material itself, on extraction layer matching and on the device structure are important footstones for realizing highly efficient, stable, reproducible perovskite solar cells.

In this thesis work, we aimed at achieving high efficiency perovskite solar cells and at having a good understanding of the perovskite photovoltaic devices, with a special attention on the role of the hole blocking layer, the extraction ability of electrons transporting layer, the design of highly effective electron extraction layers, the excellent crystallinity of multiple cation perovskite and so on. Firstly, we focused on traditional TiO<sub>2</sub> electron transporting layer preparation by different techniques. We investigated how the thickness, phase, and morphology of TiO<sub>2</sub> hole blocking layers affect the cells functioning. Adopting the optimal TiO<sub>2</sub> hole blocking layer, we attained a relatively high efficiency of 17.49% in the CH<sub>3</sub>NH<sub>3</sub>PbI<sub>3</sub> solar cells. Subsequently, we focused our research on the multiple cations perovskites (i.e. Cs5FAMA and FAMA), obtained the pure photoactive black  $\alpha$ -phase, less defect, and high crystallinity. Finally, we realized a series of highly efficient, stable and reproducible perovskite solar cells.

In the chapter 1 we have presented the context of the research on the solar cells. We detailed the functioning mechanism of the silicon and dye-sensitized solar cells. We explained the different characters of structure, electrons separation processes and mechanisms in the corresponding cells. In addition, we further introduced perovskite

solar cells development and revolution in the past few years, including the various functional layers, cells structure, and some hot-point studying.

In Chapter 2 we have investigated the key parameters that render the TiO<sub>2</sub> blocking layer (BL) efficient in PSCs. Several BLs have been prepared using the aerosol spray pyrolysis and the spin-coating techniques. The sprayed BLs presented thin, highly compact, full-covering characters in their morphology. They exhibited the pure anatase phase characters to boost electrons transport. Besides, we developed the use of the impedance spectroscopy technique to investigate the various processes taking place in the cells under illumination and how they are influenced by the BL.

In Chapter 3 we developed two kinds of perovskite deposition techniques, the simple direct film-forming and the hot-casting methods. The direct film-forming without dripping process realized high purity perovskite  $\alpha$ -phase and could be used for deposition at the large scale. The hot-casting technology realized a dense, big-grain, and pure phase perovskite layer, in order to further decrease grain boundaries and eliminate its detrimental effect on the charge carriers recombination. In first sections, we investigated the promotion of spontaneous crystallization and growth of FAMA (FA<sub>0.83</sub>MA<sub>0.17</sub>Pb(I<sub>0.83</sub>Br<sub>0.17</sub>)<sub>3</sub> with FA the formamidinium cation and MA the methylammonium one) perovskite by the control the supersaturation concentration of the precursor solution. Then we adopted an anti-solvent dripping step to trigger crystallization and finally realized high efficiency and highly reproducible perovskite photovoltaic devices. The investigation of 30 FAMA photovoltaic devices exhibited the following average photovoltaic parameters;  $V_{oc} = 1104$  mV,  $J_{sc} = 23.16$  mA/cm<sup>2</sup>, and FF = 78%, from which it resulted an average power conversion efficiency (PCE) of 19.8%.

In Chapter 4 we thoroughly investigated the effect of adding 5% of Cs cation into the dual cations FAMA perovskite. Our analysis of the early period nucleation kinetic before heating treatment showed that the addition of Cs promotes the heterogeneous nucleation and suppresses phase segregation compared to FAMA. Based on energy band theory, we proposed a photoluminescence mechanism for Cs5FAMA and

predicted that Cs5FAMA belongs to direct semiconductors. We also discussed the impact of point defects of perovskite on these cells. In addition, we investigated the effects of the various electron extraction layers on perovskite solar cells performances. We designed a new electron extraction layer of TiO<sub>2</sub>-compact/TiO<sub>2</sub>-mesoporous/PCBM, this configuration cells achieved a very high  $J_{sc}$  of 24.61 mA/cm<sup>2</sup>. Finally, we achieved high efficiency, reproducible, and stable devices with Cs5FAMA perovskite. These photovoltaic devices exhibited at best an open circuit voltage  $V_{oc} = 1104$  mV, a short circuit current  $J_{sc} = 24.19$  mA/cm<sup>2</sup>, and a fill factor  $FF = 77.4\%$ , resulting in a PCE of 20.67%.

The investigations presented in this thesis show that the electron transporting layer and perovskite components are very important in the perovskite solar cells. New matching energy level materials have been used for extraction layer to promote operating efficiency and stability. Besides, it also certainly depends on the electron transporting speed and injection ability. For perovskite itself, important points are how making perovskite with reduced point defects and improved phase purity, high crystallinity, which play a key role for decreasing charges recombination inside of perovskite and realize the best performance in the cells. Through investigated various electrons extraction layers, we think that the traditional TiO<sub>2</sub> layer maybe not the best choice, because of the electrons extraction ability of these layers are weaker by two orders of magnitude than that of hole extraction ability on the Spiro-OMeTAD. It is noteworthy that recently adopted polymer electron transporting layers achieved a great progress in the inverted structure of perovskite solar cells. It resulted in reduced hysteresis phenomena. In addition, recent research shows that the Spiro-OMeTAD maybe not the best candidate for hole transporting material.

Therefore, we believe that perovskite solar cell is the most promising photovoltaic device for the future, the efficiency records of which will continuously refresh and that further understanding of their operating mechanism will be achieved.

# List of figures

## Chapter 1

<b>Figure 1.1</b> Renewable power capacity and cumulative capacity, from the report Renewable Energy Capacity Statistics 2015 by International Renewable Energy Agency (IRENA). .....	4
<b>Figure 1.2</b> Reference solar irradiation spectra according to the standards by the American Society of Testing and Materials. ....	5
<b>Figure 1. 3</b> Silicon solar cells operating mechanism. (a) Silicon materials doping to form p-type and n-type semiconductor. (b) p-n junction formation. (c) Formation of the built-in electric field. (d) A pair of electron-hole formation after sunlight irradiation. (e) Realized charge carriers separation and current generation. ....	8
<b>Figure 1. 4</b> Device architecture of a typical liquid dye-sensitized solar cell.[21] .....	9
<b>Figure 1. 5</b> Dye-sensitized solar cell device working mechanism.[22].....	11
<b>Figure 1.6</b> Chart of perovskite solar cell efficiency records by the National Renewable Energy Laboratory (NREL).[25] .....	12
<b>Figure 1.7</b> Performance evolution chart of the best certified research cell efficiencies as published by NREL.[25] .....	13
<b>Figure 1. 8</b> Ball and stick model of generic ABX <sub>3</sub> perovskite structure.[34].....	14
<b>Figure 1.9</b> Standard structure of perovskite solar cells and functional layer assemblies (the left schematic). Cross section SEM image of a standard perovskite solar cells (right image). The insets are pictures of FAMA and Cs5FAMA –based perovskite solar cells. ....	16
<b>Figure 1. 10</b> Molecular structure of 2,2',7,7'-tetrakis-N,N-di(4-methoxyphenyl)amine-9,9'-spirobifluorene (Spiro-MeOTAD), utilized as HTM in PSCs.....	19

## Chapter 2

<b>Figure 2.1</b> Field emission scanning electron microscopy (SEM) views of blocking layers. (a-c) BL-S prepared by spray-pyrolysis technology; (d-k) prepared by spin coating. (d,e) BL-A; (f-h) BL-H and (i-k) BL-P. ....	36
<b>Figure 2.2</b> Ultraviolet-Visible (UV-Vis) absorption spectra of various TiO <sub>2</sub> blocking layers,	

displayed as Tauc plots.....	37
<b>Figure 2.3</b> Raman spectra of the various prepared TiO <sub>2</sub> blocking layers on FTO/Glass by the different precursor solution and deposited technologies.....	38
<b>Figure 2.4</b> Raman spectra zoom view at the first E <sub>g</sub> mode for the various prepared TiO <sub>2</sub> blocking layers.....	39
<b>Figure 2.5</b> Cyclic voltammograms of FTO electrode (dashed line) and BL electrodes (full lines) in an aqueous solution containing the Fe(CN) <sub>6</sub> <sup>3-/4-</sup> redox system. Scan rate 50 mV.s <sup>-1</sup> . The inset is the ΔE <sub>p</sub> curve parameter for FTO and the spin-coated TiO <sub>2</sub> layers.....	40
<b>Figure 2.6</b> SEM views of the mesoporous TiO <sub>2</sub> layer, deposited on the BL-S/FTO substrate. The left image is a top view, and the right image is a cross-sectional view. ....	42
<b>Figure 2.7</b> Top view SEM images. (a) The initial deposited PbI <sub>2</sub> layer. (b) The same layer after its reaction with MAI and its transformation into MAPbI <sub>3</sub> layer.....	42
<b>Figure 2.8</b> (a) XRD pattern of two-step MAPbI <sub>3</sub> perovskite layer. (d) Absorbance and photoluminescence spectra of two-step MAPbI <sub>3</sub> on glass (red curves) and on BL-S (dark blue curves).....	43
<b>Figure 2.9</b> Typical <i>J-V</i> curves of MAPbI <sub>3</sub> perovskite solar cells prepared on various BLs. The solid lines are the photocurrent measured under AM1.5 filtered one sun illumination; the dashed lines are the dark current.....	44
<b>Figure 2.10</b> Dark current of two-step MAPbI <sub>3</sub> perovskite solar cells prepared on various BLs. The dark current is plotted in a logarithmic scale. ....	46
<b>Figure 2.11</b> Perovskite solar cells impedance spectra in a Nyquist plot. (a) Spectra at short circuit (0.0V) for various BLs. (b) The same with an applied voltage of 0.6V. (c) Zoom for BL-S at 0.6 V. The dots are the experimental points and full lines are the fits. Blue curve, BL-S; Red, BL-A; Green, BL-H; and Black, BL-P. (d) Effect of applied potential on the impedance response of the BL-A cell.....	48
<b>Figure 2.12</b> Simplified (a') and general (a) equivalent electrical circuit used to fit the impedance spectra (HF, high frequency; IF, intermediate frequency; and LF, low frequency). Fitting results of the electrical parameters plotted as the function of the applied potential: (b) R <sub>1</sub> , (c) C <sub>1</sub> , (d) C <sub>3</sub> , (e) R <sub>3</sub> , (f) τ <sub>3</sub> and (g) L <sub>2</sub> . ....	51
<b>Figure 2.13</b> Variation of the C <sub>2</sub> parameter with the applied potential. ....	52

## Chapter 3

- Figure 3.1** X-ray diffraction (XRD) patterns of FAMA perovskite layer prepared by simple direct film-forming method (the first four patterns) and anti-solvent method (the bottom pattern). Effect of low and high precursor solution concentration and annealing for FAMA prepared by direct film-forming method. The symbol \* is F-doped tin dioxide, # is un-reacted  $\text{PbI}_2$  phase,  $\delta$  is non-photoactive yellow phase and  $\alpha$  is phase photoactive black phase. ....67
- Figure 3.2** XRD patterns of FAMA perovskite layer by direct film-forming method, under the different annealing times, 5second, 10 min, 20 min, 30 min, 40 min and 1 hour, respectively. ....68
- Figure 3.3** Ultraviolet-visible (UV-vis) absorption spectrum of FAMA perovskite layer by direct film-forming method prepared from the high and low concentrations of precursor solution. The inset is a zoom of the bandgap edge.....69
- Figure 3.4** UV-vis absorption spectra of FAMA perovskite layers without annealing and for annealing times of 30 min and 1h. ....69
- Figure 3.5** Top views of scanning electron microscopy (SEM) images of perovskite films prepared from low concentration (a,b) and high concentration (c,d) precursor solutions. The layers before heating treatment are in the left and those after heating treatment in the right. The scale bar is 200 nm. ....71
- Figure 3.6** Current density / voltage ( $J$ - $V$ ) curves of the FAMA perovskite solar cell prepared by the direct film-forming method. (Solar cell N 39 in Table 3.1).....71
- Figure 3.7** X-ray diffraction (XRD) patterns of fresh and 10-days aged FAMA perovskite layers prepared by host-casting method. ....73
- Figure 3.8** Ultraviolet-visible (UV-vis) absorption spectra of FAMA perovskite layers prepared by different deposition techniques (anti-solvent dripping method, host-casting, and direct film-forming technique). ....74
- Figure 3.9** SEM top views of hot-casted FAMA layers on mesoporous  $\text{TiO}_2$  underlayer. (a) and (b) show big-sized FAMA perovskite grains under different magnifications. (c) and (d) are SEM views of Spiro-OMeTAD (hole transporting material) deposited on top of the FAMA perovskite layer prepared by hot-casting. (e) Cross-sectional scheme of the Spiro-OMeTAD (in grey) deposited on the perovskite (in brown). ....75
- Figure 3.10** SEM images focusing on ridge structures of perovskite (brighter lines) at various

magnifications.....	76
<b>Figure 3.11</b> SEM top views at various magnifications of the FAMA perovskite layer prepared via the general anti-solvent dripping method.....	77
<b>Figure 3.12</b> Scanning electron microscopy (SEM) images of FAMA perovskite layer at the same position by spilt screen technology, using different electronic signals: reflected back-scattered electrons (RBSD) in the left image, and secondary electrons (SE2) in the right image. ....	78
<b>Figure 3.13</b> Time-correlated single-photon counting (TCSPC) curves showing the longer lifetime of charge carriers in the pristine FAMA perovskite film compared to MAPbI <sub>3</sub> perovskite. The excitation wavelength was 470 nm. ....	81
<b>Figure 3.14</b> Steady-state photoluminescence (PL) spectra of FAMA perovskite on glass and combined with various electron and hole extraction layers: TiO <sub>2</sub> /compact layer, TiO <sub>2</sub> /mesoporous layer and spiro-OMeTAD. (470 nm excitation wavelength).....	82
<b>Figure 3.15</b> Time-correlated single photon counting (TCSPC) curves of pristine FAMA perovskite deposited on glass and combined with various electron and hole transporting layers: TiO <sub>2</sub> -compact layer, TiO <sub>2</sub> -compact/TiO <sub>2</sub> -mesoporous layer, TiO <sub>2</sub> -compact/ TiO <sub>2</sub> -mesoporous/PCBM layer and spiro-OMeTAD, respectively. ....	83
<b>Figure 3.16</b> <i>J-V</i> curve of the best FAMA solar cell performing at 20.15% ( $V_{oc} = 1176$ mV, $J_{sc} = 23.06$ mA/cm <sup>2</sup> , and FF=78.2%), measured for a reverse scan rate of 25 mV/s. The inset shows the MMP tracking for 60s monitored at $V_{max} = 967$ mV and which finally produced 20.79 mA/cm <sup>2</sup> , yielding stabilized efficiency of 20.11%. ....	85
<b>Figure 3.17</b> <i>J-V</i> curve of the best FAMA perovskite solar cell with and without PCBM layer. The photovoltaic metrics details are listed at the bottom of the <i>J-V</i> curves. ....	86
<b>Figure 3.18</b> <i>J-V</i> metrics for 30 FAMA perovskite independent devices, including $V_{oc}$ , $J_{sc}$ , FF, and PCE. ....	87
Chapter 4	
<b>Figure 4.1</b> Nucleation kinetics tracking for Cs5FAMA and FAMA, upon anti-solvent dripping. The anti-solvent was rapidly dripped after 100s on prepared precursor thin-film. The absorbance was recorded every 6 seconds and monitored at 495~500nm wavelength. ....	95
<b>Figure 4.2</b> Ultraviolet-visible (UV-vis) absorption spectra of FAMA and Cs5FAMA on the TiO <sub>2</sub> and glass substrates. The normalized photoluminescence (PL) spectra of FAMA and Cs5FAMA on	

glass substrate are presented on the same figure.....	96
<b>Figure 4.3</b> Tauc plots at the near optical bandgap edges of both absorption spectra, which show that Cs5FAMA bandgap is 1.58 eV and FAMA bandgap is 1.60 eV.....	97
<b>Figure 4.4</b> Steady state photoluminescence spectrum of Cs5FAMA perovskite on the glass substrate. It shows that the PL emission energy is about 1.59 eV. ....	98
<b>Figure 4.5</b> Photoluminescence mechanism of Cs5FAMA and FAMA. (a) Proposed excitation and photoluminescence mechanism in Cs5FAMA perovskite. (b) Proposed excitation and photoluminescence mechanism in FAMA perovskite. ....	99
<b>Figure 4.6</b> X-ray diffraction (XRD) patterns of Cs5FAMA and FAMA perovskite layer. Here, the symbol * is F-doped tin dioxide, the # is the un-reacted PbI <sub>2</sub> phase, δ marks the non-photoactive yellow phase and α is the photoactive black phase. ....	101
<b>Figure 4.7</b> Top view of scanning electron microscope (SEM) images of (a) FAMA and (b) Cs5FAMA perovskite layers. ....	102
<b>Figure 4.8</b> SEM images of (a) FAMA and (b) Cs5FAMA layers after a heating treatment at 130 °C for 3 hours. ....	103
<b>Figure 4.9</b> XRD patterns of FAMA before (red dashed line), and after (black solid line) an heating treatment at 130 °C for 3h. ....	104
<b>Figure 4.10</b> XRD patterns of Cs5FAMA before (red dashed line), and after (black solid line) an heating treatment at 130 °C for 3h. ....	104
<b>Figure 4.11</b> Time-correlated single-photon counting (TCSPC) curves showing the longer lifetime of charge carriers in the pristine Cs5FAMA perovskite film, compared to FAMA. ....	106
<b>Figure 4.12</b> Steady state PL spectrum of Cs5FAMA showing the emission intensity quenching on the electrons transport layer (ETL). The investigated substrates are glass, TiO <sub>2</sub> compact layer, TiO <sub>2</sub> mesoporous layer and Spiro-OMeTAD (on top of Cs5FAMA). ....	107
<b>Figure 4.13</b> Time-correlated single-photon counting (TCSPC) curves of pristine Cs5FAMA perovskite deposited on glass and combined with various electron and hole transport layers: FTO/TiO <sub>2</sub> -compact layer, FTO/TiO <sub>2</sub> -compact/TiO <sub>2</sub> -mesoporous layer, FTO/TiO <sub>2</sub> -compact/TiO <sub>2</sub> -mesoporous/PCBM layer and Spiro-OMeTAD.....	109
<b>Figure 4.14</b> Energy level diagram of various layers in perovskite solar cell.....	110
<b>Figure 4.15</b> Current density/voltage ( <i>J-V</i> ) curve of the best Cs5FAMA solar cell performing at	

20.67% ( $V_{oc} = 1104$  mV,  $J_{sc} = 24.19$  mA/cm<sup>2</sup>, and fill factor 77.4%), measured at scan rate of 25 mV/s. The inset shows the maximum power point (MPP) tracking for 60s monitored at  $V_{max} = 944$  mV and finally producing 21.86 mA/cm<sup>2</sup>, yielding a stabilized efficiency of 20.64%..... 111

**Figure 4.16** A typical *J-V* curves of Cs5FAMA device measured in the forward and reverse potential scan directions (potential scan rate at 25 mV/s)..... 112

**Figure 4.17** External quantum efficiency of the best performing Cs5FAMA solar cell, the integrated short circuit current density is 23.6 mA/cm<sup>2</sup>..... 112

**Figure 4.18** *J-V* metrics for 30 devices of FAMA and 40 devices of Cs5FAMA, including  $V_{oc}$ , open circuit voltage;  $J_{sc}$ , short circuit current; FF, fill factor; PCE, power conversion efficiency. .... 115

**Figure 4.19** *J-V* curves for devices with various perovskites in the different configuration of perovskite solar cells measured with a reverse scan rate at 25mV/s..... 116

**Figure 4.20** Top views of scanning electron microscopy (SEM) images of (a) Cs5FAMA and (b) Cs10FAMA perovskite layers. The scale bar is 500 nm. .... 117

**Figure 4.21** MPP tracking for 5 minutes of unencapsulated Cs5FAMA device placed under ambient conditions, yielding a stabilized current density of 21.83 mA/cm<sup>2</sup> and a stabilized efficiency of 20.6 %..... 118

## List of tables

<b>Table 2.1</b> Analysis of the CV curves redox peaks in figure 2.5. $E_p$ is the potential difference between the anodic and cathodic peak maxima. Intensity ratio between the cathodic peak of FTO and of BLs.....	41
<b>Table 2.2</b> Photovoltaic parameters of $J-V$ curves of two-step MAPbI <sub>3</sub> PSCs for various BL (AM1.5G filtered 100 mW.cm <sup>-2</sup> illumination). .....	45
<b>Table 3.1</b> $J-V$ curve parameters for the forward and backward potential scans of FAMA perovskite solar cells prepared by the direct film-forming technology. Under AM1.5G 100 mW.cm <sup>-2</sup> illumination. The potential scan rate was 25mV/s. ....	72
<b>Table 4. 1</b> $J-V$ curve parameters of <b>the</b> best solar cells presented in Figure 4.18.....	116

## List of the abbreviations and symbols

DSSC	Dye-sensitized solar cell
ssDSSC	Solid state dye sensitized solar cell
PSCs	Perovskite solar cells
HPs	Hybird perovskites
TiO <sub>2</sub> BLs	TiO <sub>2</sub> Blocking layers
HTL	Hole transport layer
HTM	Hole transport materials
ETL	Electron transport layer
ETM	Electron transport materials
TCO	Transparent conductive oxide
LUMO	Lowest unoccupied molecular orbital
HOMO	Highest occupied molecular orbital
$V_{oc}$	Open-circuit potential
$J_{sc}$	Short-circuit photocurrent
FF	Fill factor
PCE	Power conversion efficiency
IPCE	Incident photon-to-current conversion efficiency
APCE	Absorbed photon-to-current conversion efficiency
$P_{max}$	Maximum output electrical power
MPP	Maxima power point
$e$	Elementary charge
$k$	Boltzman constant
$T$	Temperature
$R_s$	Series resistance
$R_p$	Shunt resistance
CB	Conduction band

VB	Valence band
$\lambda$	Wavelength
$\nu$	Light frequency
$\eta$	Cell efficiency = PCE
PT	Phase transition
eV	Electron volt
IS	Impedance spectroscopy
LF	Low frequencies
IF	Intermediate frequency
HF	High frequencies
EEC	Equivalent electrical circuit
FTO	Fluorine-doped tin oxide
ITO	Indium tin oxide
TBP	4-tert-butylpyridine
LiTFSI	Bis(trifluoromethane)sulfonimide lithium salt
TTIP	Titanium isopropoxide
PCBM	[6,6]-phenyl-C61-butyric acid methyl ester
ACN	Acetonitrile
MAPI	$\text{CH}_3\text{NH}_3\text{PbI}_3$
FAMA	$\text{FA}_{0.83}\text{MA}_{0.17}\text{Pb}(\text{I}_{0.83}\text{Br}_{0.17})_3$
DMF	Dimethyl formamide
DMSO	Dimethylsulfoxide
FE-SEM	Field emission scan electron microscopy
XRD	X-ray diffraction
PL	Photoluminescence
EQE	External quantum efficiency
TCSPC	Time-resolved single-photon counting
ALD	Atomic layer deposition
UV-vis	Ultraviolet-visible

Rrms	Root mean square of roughness
Q	Electrical charge density
R	Gas constant
P	Supersaturated vapor pressure
$\Delta G$	Balanced state Gibbs energy
HI	Hysteresis index
CE	Counter electrode

## Résumé

Dans cette thèse, nous nous sommes appliqués à optimiser la couche bloquante des trous (BL) de  $\text{TiO}_2$  et à développer des pérovskites à cations monovalents multiples (A dans  $\text{ABX}_3$ ) pour l'application. Nous avons finalement obtenu des PSC très stables, reproductibles et de très haut rendement de photoconversion. Le Chapitre 1 est une revue bibliographique de différentes technologies de cellules solaires, des composants des cellules de type PSC ainsi que des principales techniques de caractérisation des cellules photovoltaïques. Dans le Chapitre 2, nous avons étudié les paramètres qui rendent les couches bloquantes de  $\text{TiO}_2$  efficaces. Plusieurs BLs ont été préparées par la technique de pyrolyse-spray et par spin-coating. Nous avons aussi utilisé la spectroscopie d'impédance pour étudier les différents phénomènes de transfert et d'accumulation de charges se déroulant dans le dispositif sous éclairage et comment ils sont influencés par la BL. Dans le chapitre 3, nous avons étudié le phénomène de cristallisation spontanée de la pérovskite FAMA par le contrôle de la concentration de supersaturation de la solution de précurseur. Nous avons développé deux types de dépôts de la pérovskite, le dépôt direct et la technique de dépôt à chaud (hot-casting). Dans le chapitre 4, nous avons étudié l'ajout de cation césium ( $\text{Cs}^+$ ) dans la structure pérovskite FAMA. nous avons obtenu des dispositifs de rendement très élevé reproductible et stable avec la pérovskite  $\text{Cs5FAMA}$ . Pour les cellules record, nous avons mesuré:  $V_{oc} = 1104$  mV,  $J_{sc} = 24.19$  mA/cm<sup>2</sup>, et  $FF = 77.4\%$ , soit un PCE de 20.67 %. Le suivi de la puissance maximale délivrée a donné un rendement stable de 20.6%.

## Mots Clés

Pérovskites  
Dioxyde de titane  
Cellules solaires  
Photovoltaïque

## Abstract

In this thesis, we have optimized the  $\text{TiO}_2$  hole blocking layer (BL) and we have investigated multiple monovalent cation (A in  $\text{ABX}_3$ ) perovskite compounds for PSC application. Finally we realized a series of stable, reproducible and highly efficient PSCs. Chapter 1 is a bibliographic review of solar cells and PSC components as well as a description of the main techniques employed for the device characterizations. In chapter 2, we have investigated the key parameters that render the  $\text{TiO}_2$  BL efficient in PSCs. Several BLs have been prepared using the aerosol spray pyrolysis and the spin-coating techniques. we developed the impedance spectroscopy technique to investigate the various processes taking place in the cells under illumination and how they are influenced by the BL. In the chapter 3, we have investigated the promotion of spontaneous crystallization and growth of FAMA perovskite by the control the supersaturation concentration of the precursor solution. We developed two kinds of perovskite deposited techniques, the simply direct film-forming and the hot-casting method. In the chapter 4, we have thoroughly investigated the effect of adding cesium cation ( $\text{Cs}^+$ ) into the dual cation FAMA perovskite. We achieved high efficiency, reproducible, and stable devices with  $\text{Cs5FAMA}$  perovskite. These photovoltaic devices exhibited at best an open circuit voltage  $V_{oc} = 1104$  mV, a short circuit current  $J_{sc} = 24.19$  mA/cm<sup>2</sup>, and a fill factor  $FF = 77.4\%$ , resulting in a PCE of 20.67 %. The maximum power point tracking of the cells produced a steady-state PCE of 20.6%.

## Keywords

Perovskite  
Titanium dioxide  
Solar cells  
Photovoltaic